Energy Storage Materials

Networks of Electrochemical Oxidation of Common Lithium-Ion Battery Solvents Revealed by NMR Spectroscopy

--Manuscript Draft--

Manuscript Number:	ENSM-D-26-00220R1
Article Type:	Research Paper
Section/Category:	Electrochemical energy storage
Keywords:	Lithium-ion battery; Electrolytes; NMR; oxidation reactions; high voltages
Corresponding Author:	Leah Rynearson Argonne National Laboratory Lemont, Illinois UNITED STATES OF AMERICA
First Author:	Leah Rynearson
Order of Authors:	Leah Rynearson
	Haoyu Liu, Ph.D.
	Stefan Ilic, Ph.D.
	Milena Martins, Ph.D.
	Pedro Farinazzo Bergamo Dias Martins, Ph.D.
	Jens Niklas, Ph.D.
	Justin G. Connell, Ph.D.
	Dusan Strmcnik, Ph.D.
	Jordi Cabana, Ph.D.
	Baris Key, Ph.D.
Manuscript Region of Origin:	North America
Abstract:	Raising the upper cutoff voltage of lithium-ion batteries (LIBs) to increase energy density often exceeds the electrolyte's anodic stability limit, accelerating degradation and creating a major durability tradeoff. Designing electrolytes that can sustain long-term high-voltage cycling requires a clearer understanding of the fundamental mechanisms occurring when commercial carbonate solvents oxidize. To this end, simplified single-salt, single-solvent formulations of LiClO4 and LiPF6 in dimethyl carbonate (DMC), ethylene carbonate (EC), or ethyl methyl carbonate (EMC) were anodically electrolyzed on inert electrodes and monitored for extended periods of time using 1H, 13C, 19F, and 35Cl nuclear magnetic resonance (NMR) spectroscopy. The controlled environment of the experiments, coupled to the unique sensitivity of NMR, unveiled novel metastable intermediates and the formation of branching networks of products with temporal evolution. Oxidation of the pristine solvent primarily proceeds through a radical pathway that also produces highly reactive protons but faces competition from a second pathway involving a radical carbocation intermediate. In all cases, the intermediates follow a variety of downstream pathways that can intersect with each other. The concomitant network of reactions represents a significant increase in complexity compared to common descriptions in the literature, yet, critically, it helps explain the wide range of products typically identified in electrolyte oxidation in complete cells. The results highlight the need for refocusing fundamental research on anodic stability to analysis of the hierarchy of reaction networks to better inform efforts to mitigate the detrimental effects on battery performance, including prevention and harvesting of proton and radical products.
Opposed Reviewers:	
Response to Reviewers:	

Cover Letter

Baris Key, Ph.D.
Chemist

Electrochemical Energy Storage Department
Chemical Sciences and Engineering Division
Argonne National Laboratory
9700 South Cass Avenue, Bldg. 200
Lemont, IL 60439

1-630-252-7351
bkey@anl.gov

March 6th, 2026

Prof. Jie Xiao
Editor-in-Chief, Energy Storage Materials
Department of Mechanical Engineering
University of Washington
3900 E Stevens Way NE, Box 352600
Seattle, WA 98195

Dear Prof. Xiao,

This letter accompanies the resubmission of our manuscript entitled "Networks of Electrochemical Oxidation of Common Lithium-Ion Battery Solvents Revealed by NMR Spectroscopy" (Manuscript Number: ENSM-D-26-00220) to Energy Storage Materials.

We thank the editor and reviewers for their time in reviewing our work and their constructive feedback. We've included a response letter addressing all their comments, questions and suggestions and the corresponding changes made in the manuscript and the supporting information files.

Based on the suggestion from Reviewer #1, we have included EPR data into the supporting information with further explanation for the lack of signal observed. We have also included MAS solid-state NMR of the oxidized EMC precipitate to help elucidate more of the polymeric product structure for Reviewer #2.

Both Reviewers #1 & 2 suggested the analysis of complex, multi-solvent commercial electrolytes may further benefit the field in developing high-performance electrolytes. We completely agree with the reviewers that this will be an interesting experiment and path forward; however, due to the length and detail already involved in this fundamental study, we plan to do those experiments throughout the next few years as a follow up to these works. The knowledge gained from this highly extensive single-solvent work will prove instrumental in interpreting complex mixtures in the future in this field.

We believe that through these additional experiments and constructive feedback from the reviewers, we have sufficiently addressed all comments and questions and thus, merit publication in Energy Storage Materials.

We look forward to hearing from you.

Yours Sincerely,

Baris Key, Ph.D.
Argonne National Laboratory

Reviewer #1: This paper employs nuclear magnetic resonance (NMR) spectroscopy to investigate the electrochemical oxidation of common solvents in lithium-ion batteries (LIBs).
While the research topic is of some interest, its scientific significance and impact are relatively limited. Several critical questions and suggestions are raised as follows:

We appreciate the input and viewpoint. We hope the reviewer will understand that our contribution in this work lays the foundational understanding of the simplest electrolyte systems with controls to develop an understanding of more complex systems which we have already started working on and plan to continue focusing on for the next few years. In fact, we were surprised by how complex the mechanistic picture is even for the simplest solvent system (as shown in Figure 3 and 4), which hopefully justifies the statement to this reviewer.

(1) In Figures c, d, and e, the reported chemical shifts appear to be incorrect or inconsistent with typical values for the targeted species.
All reported chemical shifts were done in reference to a flame-sealed external D_2O capillary with a peak at 4.67 ppm. The following sentence has been added to the experimental section to provide this additional context:

"All NMR samples were prepared in an argon-filled glovebox with flame sealed glass capillary inserts containing deuterated water (D_2O) as an external reference at 4.67 ppm."

Furthermore, peak position in NMR spectra can vary very slightly depending on the position of the sample in the magnet, orientation of the capillary inside the NMR tube (which must be used to preserve the reactive intermediates from side reactions with lock solvents unlike other studies in the literature where they're typically mixed in with the samples), and the coordination chemistry of the solution especially with our specific lock-solvent configuration to preserve sample purity and to not alter degradation mechanisms. Given the electrolyte composition in this study is continuously evolving, slight variances in chemical shift of the same species are likely. Therefore, in all cases, peak position of the main solvent was used as a secondary reference point to ensure the data was aligned properly.

(2) The TOCSY-HSQC pulse sequence is recommended to improve the resolution and reliability of the NMR spectral analysis.
Use of the TOCSY-HSQC method would certainly improve the resolution and combine the results of the COSY and HSQC run in this experiment. However, TOCSY, arguably, is best suited for complex molecules with chains of coupled spins and likely required a longer measurement time which was a limited resource to study metastable species in

this study (https://nmr.chem.columbia.edu/content/tocsy). Based on the splitting and shifts of our peaks, it seems almost all of the proposed products only have direct coupling, which COSY can and did measure perfectly well. We were also concerned about capturing any small changes in the proton spectra of the electrolyte and wanted to keep our measurements as short as possible while still maintaining the necessary resolution to identify species. We thank the reviewer for the suggestion and will likely utilize the method in our future studies into complex electrolytes where there will undoubtedly be more overlapping peaks.

(3) No electron paramagnetic resonance (EPR) experimental results were presented or discussed in the manuscript. Therefore, the entire EPR experimental section should be removed.

We have now included the EPR data for EMC and EC systems showing oxidized sample vs. baseline in Figure S5.

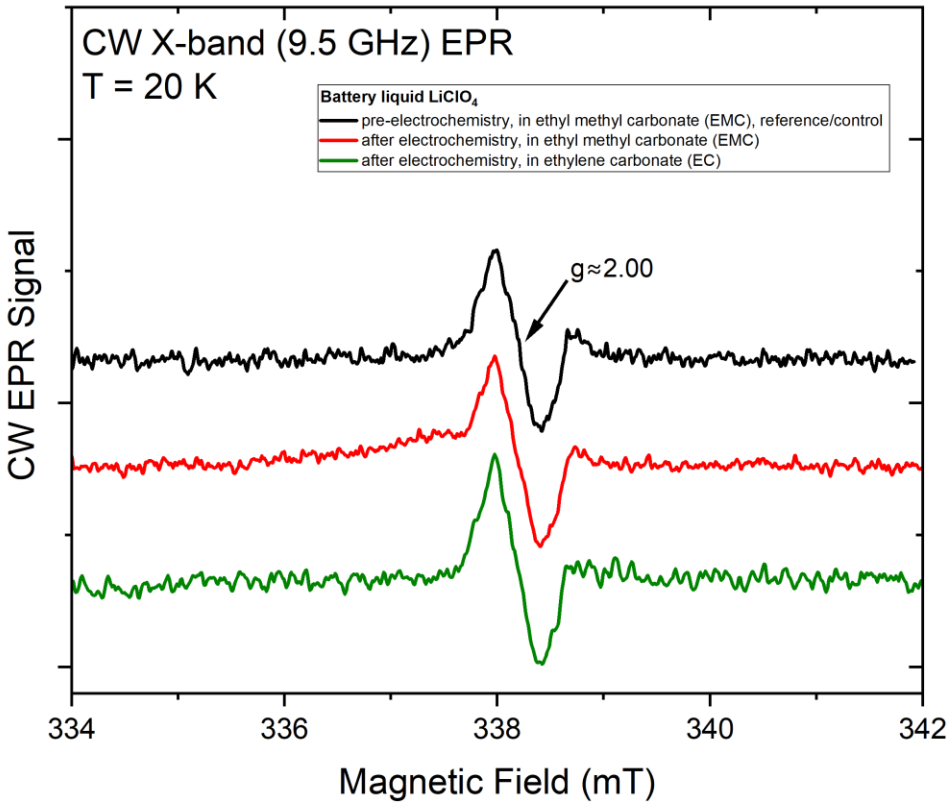

Figure S5: EPR data of oxidized $LiClO_4$/EMC and $LiClO_4$/EC

These results indicate no significant stable EPR-active radicals present which is consistent with our reasoning that either the concentrations of radicals were too low in proportion to the bulk solvent to be measured, or, more likely, as proposed in the mechanisms, that the free radical species are driven towards radical-free metastable intermediates and stable products.

(4) The research would be significantly more compelling and relevant if solvent mixtures (e.g., ethylene carbonate/dimethyl carbonate, EC/DMC), which are widely used in practical LIB electrolytes, were employed instead of single solvents.

This work is intended to be a fundamental study that can then be built upon with more complex multi-solvent electrolytes in the future; in fact, we purposefully designed it so. Given the large number of complicated products that are formed from DMC (the simplest system) and EC alone (which we started working on first but decided to switch to the simplest system), combining them from the start would have more likely resulted in a series of overlapping and complicated peaks that would be hard to distinguish and exceedingly challenging to attribute to any specific mechanism conclusively. To demonstrate this, we have plotted both $LiClO_4$/DMC and $LiClO_4$/EC together below. With the two together, there is no way to definitively assign one product to one solvent over the other, especially when considering the possibility of products coming from the two pathways intersecting. Needless to say, as suggested by the reviewer and now stated in conclusions, a follow-up study is going to be conducted on multi-component electrolyte systems with increasing complexity (solvents *and* additives) with the knowledge gained from this work of potential intersections between the different reaction mechanisms.

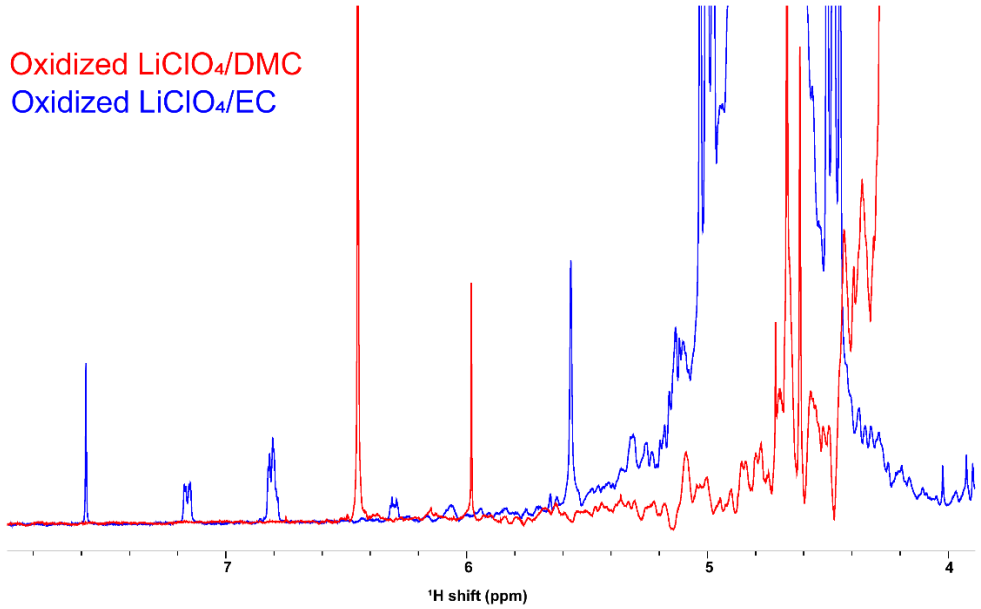

Linear combination of oxidized $LiClO_4$/DMC and $LiClO_4$/EC ^1H NMR spectra

(5) Although the use of Pt electrodes in the experiments is methodologically interesting, the results lack practical relevance. This is because the electrochemical oxidation mechanism on Pt electrodes differs substantially from that on practical LIB electrodes, such as LiCoO□ (LCO) cathodes or graphite anodes, which are more representative of real-world battery systems.

Again, this work is intended to be a fundamental study that can then be built upon with more complex systems in the future and what has been suggested by the reviewer has already been attempted (Ref. 7) with limited to no insights into the mechanisms we've proposed here. While our immediate plan is to increase electrolyte solvent and additive complexity, real-world battery system electrodes are within future plans. That being said, VC is formed at potential from EC with Pt electrodes and transition metal oxides alike (Ref. 34), directly demonstrating the commonality of reaction mechanisms in real world batteries and what is shown in this work. Ultimately, this work seeks to answer the fundamental chemical mechanisms occurring in solvent oxidation during and after the initial electrochemical reaction. The removal of one proton and two electrons would occur no matter what electrode surface the reaction occurs on (Ref. 34). Additionally, if these reactions were performed in a "real-world" battery setup, the highly reactive intermediates and products would be consumed or masked by any number of other side-reactions occurring in the cell which is why they've never been observed prior to this work that explains electrochemical VC formation. By isolating this reaction as much as possible in an idealized electrochemical system, we are able to trace mechanisms back to their initial solvent reactions directly with no confounding factors. Building complexity in future over this foundation is built-in in our experimental design.

Reviewer #2: This work presents a systematic and insightful investigation into the intrinsic electrochemical oxidation mechanisms of common carbonate solvents, providing a crucial theoretical foundation for subsequent high-performance electrolyte design. However, there are a few potential areas for improvement that require further clarification before publication:

We thank the reviewer for their kind comments and helpful suggestions.

1. The oxidation products of EMC are complex, and some peaks remain unassigned, with unclear molecular structures. The integration of other characterization techniques (such as MS) would provide complementary evidence for proposed structures.

We wish we could have provided more insight into the oxidation products of EMC, but due to the relatively asymmetric nature of the molecule itself, our current solution NMR techniques are unable to clarify the matter further. Many proposed molecules were run

through our DFT models, but none met our threshold for acceptable matches. Gel-like precipitate was extracted from the EMC NMR tubes; however, solid-state NMR was also inconclusive to its identity (see below). Still, we have added the figure below to the SI and the following statement to the manuscript:

"This precipitate was measured with ^{1}H solid-state NMR (Figure S42); however, results were inconclusive beyond that it is likely a polymeric species."

It would likely be difficult to dissolve this species into a solvent able to run on an HPLC-MS without changing some fundamental structural properties, and we have been unable to do this. By providing the splitting, shifts, and what they likely mean for the structure, we hope that we provide the basis of an assignment for other researchers and/or to our future study to potentially identify and add further context to these unknown molecules.

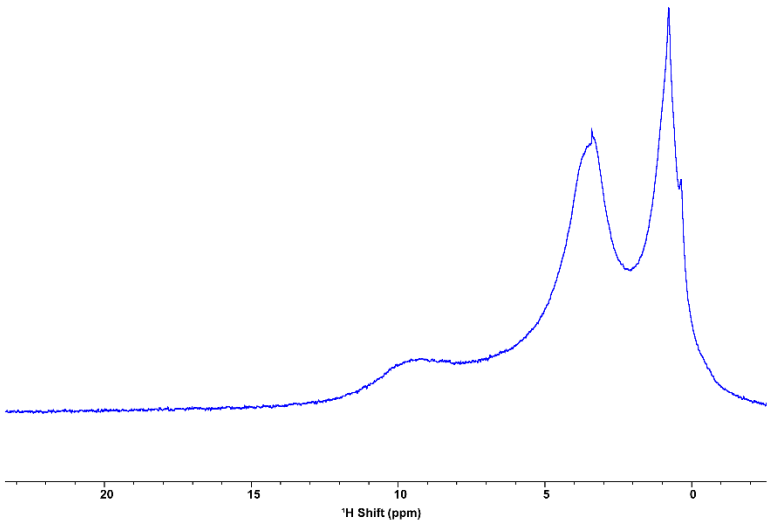

Figure S42: ^{1}H solid-state MAS NMR of $LiPF_6$/EMC precipitate

2. The experiments utilized Pt electrodes, however, in practical cathode materials (e.g., NMC) are known to catalyze electrolyte oxidation, release lattice oxygen, and participate in surface reactions. It would be valuable to discuss or conduct validation experiments on actual cathodes.

Electrolyte oxidation on typical battery cathode materials has been relatively well-studied whether it is the influence of lattice oxygen release (Ref. 19) or reactions with the electrode surface (Ref. 10). In fact, previous research (Figure 2 in Ref. 34) comparing an NMC622 cathode with C65 and a pure C65 electrode showed that the

majority of electrochemical solvent decomposition occurs at the carbon material due to the larger amount of surface area present, implying there is no specific catalytic influence from the cathode active material. However, the presence of these additional factors can actually mask the underlying chemical degradation mechanism of the electrolyte as reactive species may be formed in small amounts and be consumed through side reactions. By starting with pure Pt(111) electrodes, we are able to remove any additional consumption mechanisms and thus, capture the majority of the reaction process from oxidation to final products such as VC from EC. VC is formed at potential from EC with Pt electrodes and transition metal oxides alike (Ref. 7 and 34), directly demonstrating the commonality of reaction mechanisms in real world batteries and what is shown in this work. With this fundamental knowledge in mind, we plan to first introduce multi-solvent and additive systems and subsequently different electrode materials (LMO, LNMO, NMC) to examine the influence of each additional variable on the reaction products observed in a systematic fashion.

3. While analyzing single-solvent is methodologically sound for mechanistic clarity, commercial electrolytes typically consist of complex solvents. The study would gain more practical significance if the authors could compare the oxidation behavior of mixed solvents and determine whether synergistic or competitive effects alter degradation pathways.

We agree moving on to commercial electrolytes would be an interesting comparison, and we have already started making plans to do a follow-up on multi-component electrolyte systems with increasing complexity (solvents *and* additives) with the knowledge gained from this work of potential intersections between the different reaction mechanisms.
We think that the intermediates and fundamental mechanisms in this work provide necessary contexts for all of the potential reactive molecules in solution and will be instrumental in identifying any new products that may result from combinations of the different solvents. A statement is added to the conclusion section highlighting this.

"By systematically isolating each component of the electrolyte and mapping the whole network, this knowledge will guide fresh approaches to mitigation of degradation that more precisely target specific intermediate stages and arrest the worst outcomes, especially when moving towards more complex, multi-solvent systems with battery electrode materials."

4. It is recommended to improve the resolution of the figures and provide enlarged, annotated views of key spectral regions.
All figures were exported at 300 ppi resolution in .tif format making online pixel counts compressed. For high resolution versions, click on the link in the top corner of each

figure to see the original submitted version. All identified peaks were labelled with the abbreviation of the compound with the major peak in each oxidized sample enlarged to the side.

Graphical Abstract

Click here to access/download;Graphical Abstract;TOC graphic energy storage materials sized.tif

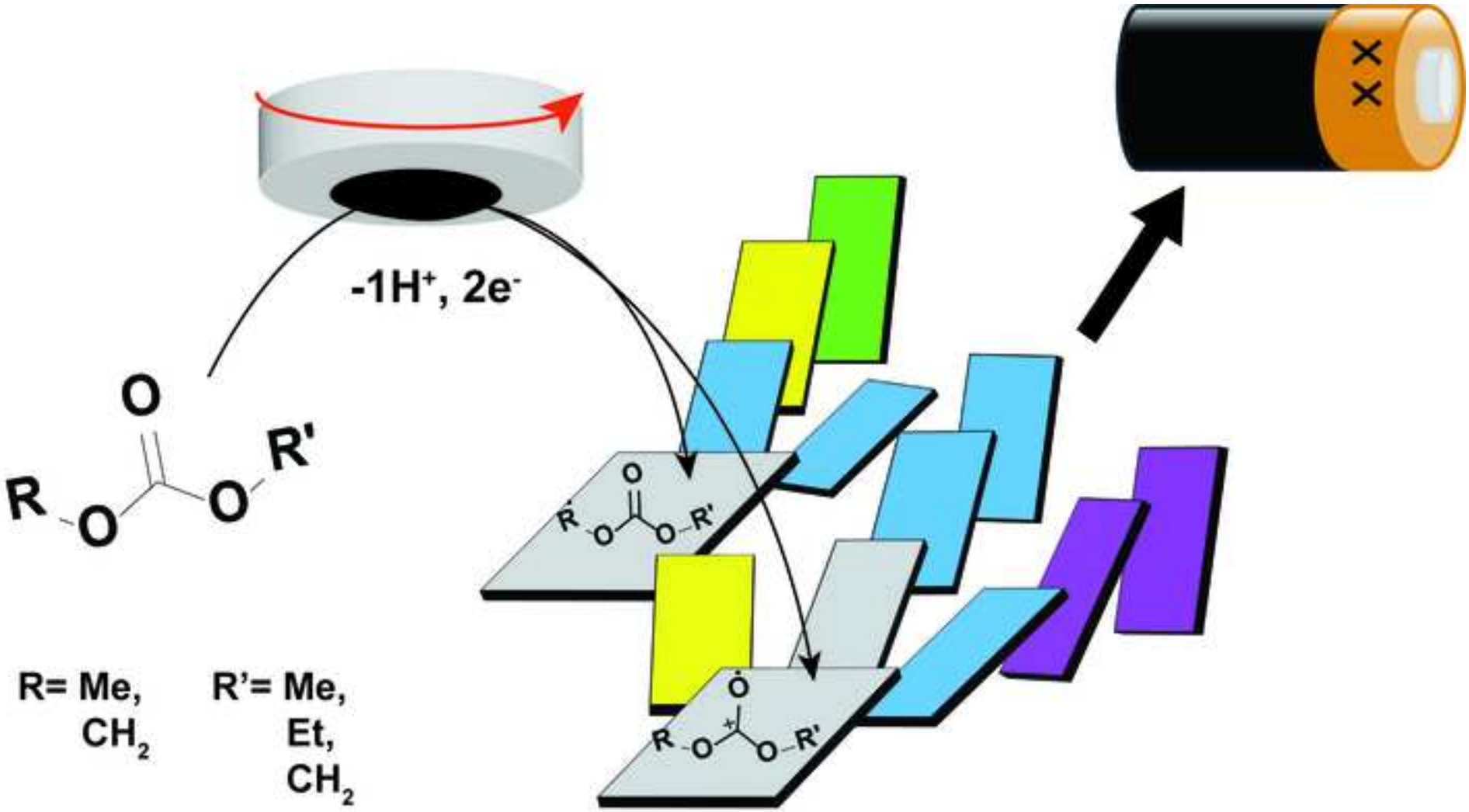

Networks of Electrochemical Oxidation of Common Lithium-Ion Battery Solvents Revealed by NMR Spectroscopy

Leah Rynearson,[a]* Haoyu Liu,[a] Stefan Ilic,[b] Milena Martins,[b, c, d] Pedro Farinazzo Bergamo Dias Martins,[b, c] Jens Niklas,[a] Justin G. Connell,[b] Dusan Strmcnik,[b, c] Jordi Cabana,[b, e] Baris Key[a]*

[a] *Chemical Sciences and Engineering, Argonne National Laboratory, Lemont, IL, USA*
[b] *Materials Science Division, Argonne National Laboratory, Lemont, IL, USA*
[c] *National Institute of Chemistry, Ljubljana, Slovenia*
[d] *Faculty of Chemistry and Chemical Engineering, University of Maribor, 2000 Maribor, Slovenia*
[e] *Department of Chemistry, University of Illinois Chicago, Chicago, IL, USA*
** Co-corresponding authors*

Corresponding Authors Address:

9700 S. Cass Avenue

Lemont, IL 60439

lrynearson@anl.gov; bkey@anl.gov

Acknowledgments

This work was primarily supported by the Assistant Secretary for Energy Efficiency and Renewable Energy, Office of Vehicle Technologies of the U.S. Department of Energy (DOE) through the Cathode-Electrolyte Interphase (CEI) consortium. The EPR measurements were supported by the U.S. Department of Energy, Office of Science, Office of Basic Energy Sciences, Division of Chemical Sciences, Geosciences, and Biosciences, through Argonne National Laboratory under Contract No. DE-AC02-06CH11357.

CRediT authorship contribution statement

Leah Rynearson: Writing – original draft, Investigation, Methodology, Visualization. **Haoyu Liu**: Investigation, Methodology, Visualization, Writing- review & editing. **Stefan Ilic**: Investigation, Methodology, Writing- review & editing. **Milena Martins:** Investigation, Visualization. **Pedro Farinazzo Bergamo Dias Martins:** Investigation, Visualization. **Jens Niklas**: Investigation, Writing- review & editing. **Justin G. Connell**: Supervision, Writing- review & editing. **Dusan Strmcnik:** Conceptualization, Methodology, Supervision, Writing- review & editing. **Jordi Cabana**: Conceptualization, Funding acquisition, Supervision, Writing- review & editing. **Baris Key**: Conceptualization, Methodology, Supervision, Writing- review & editing

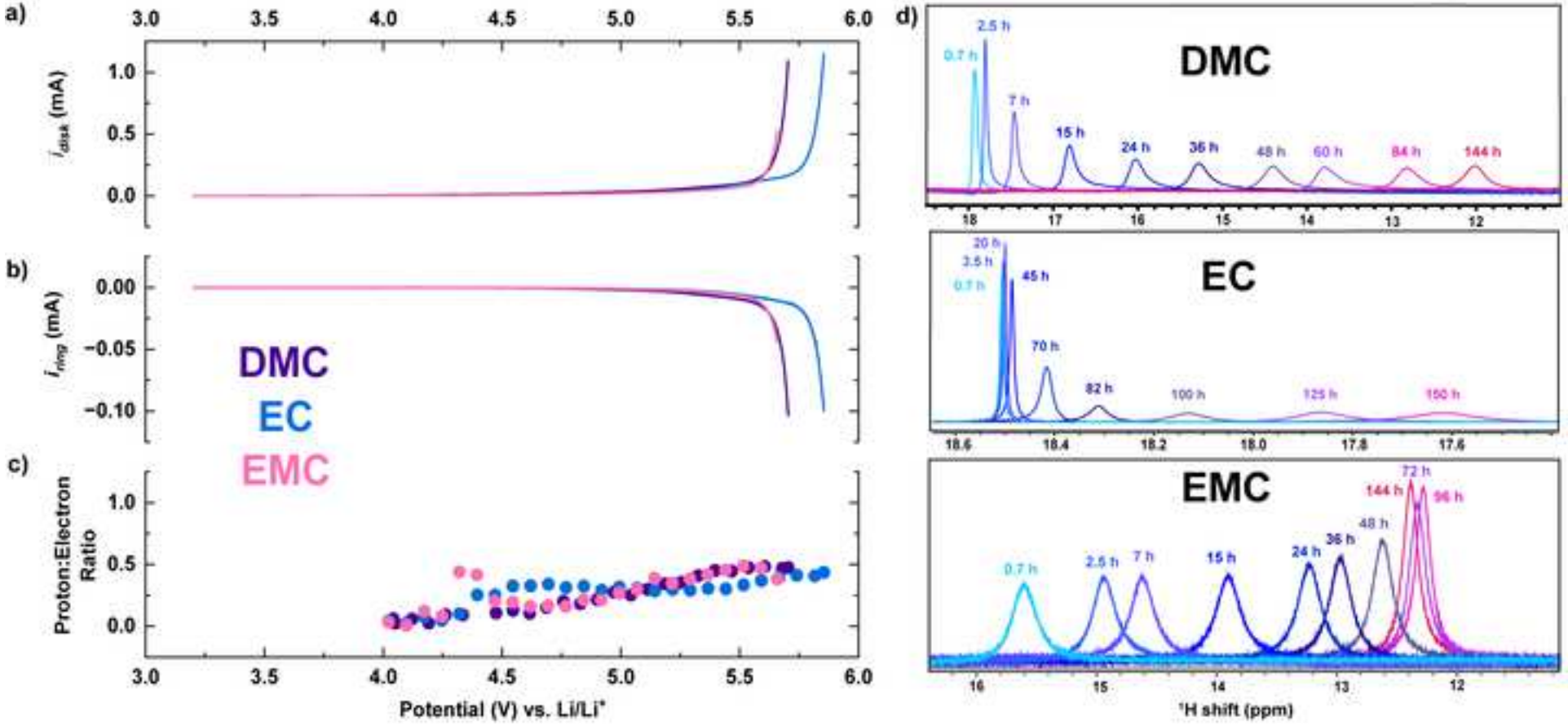

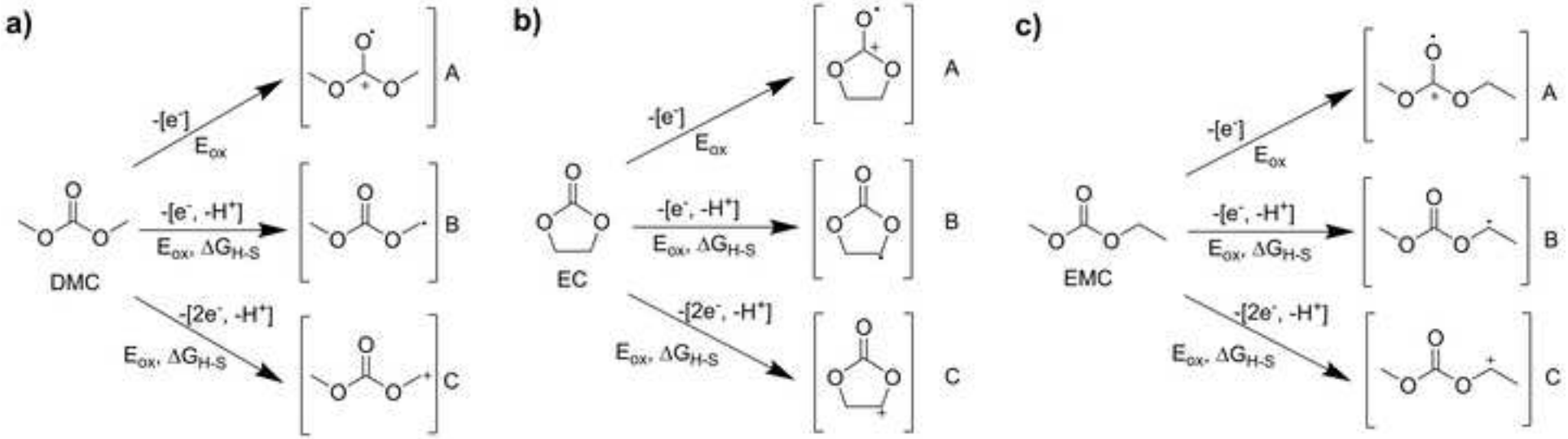

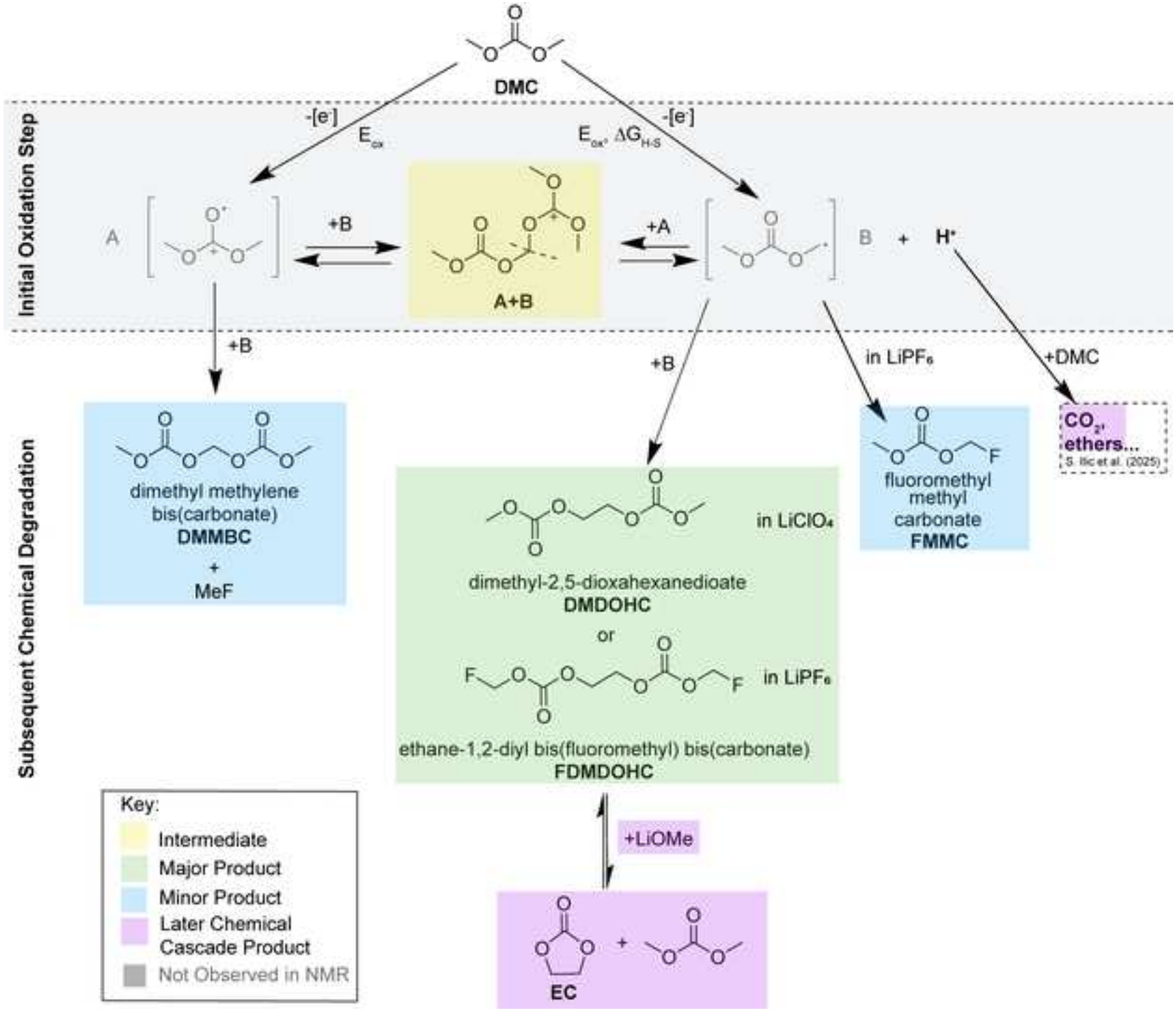

Fig4.tif

Click here to access/download;Figure;Fig4.tif

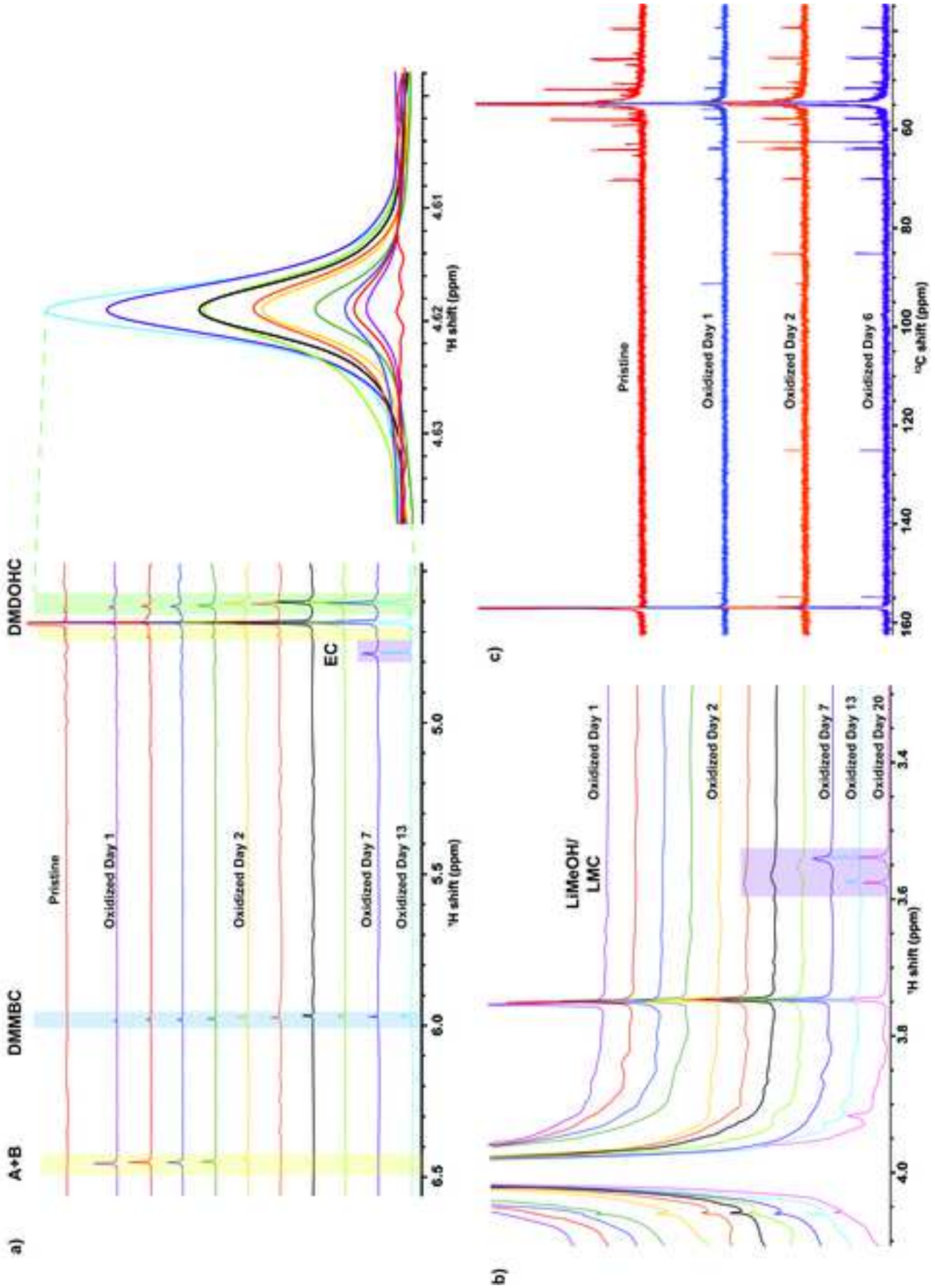

Fig5.tif

Click here to access/download;Figure;Fig5.tif

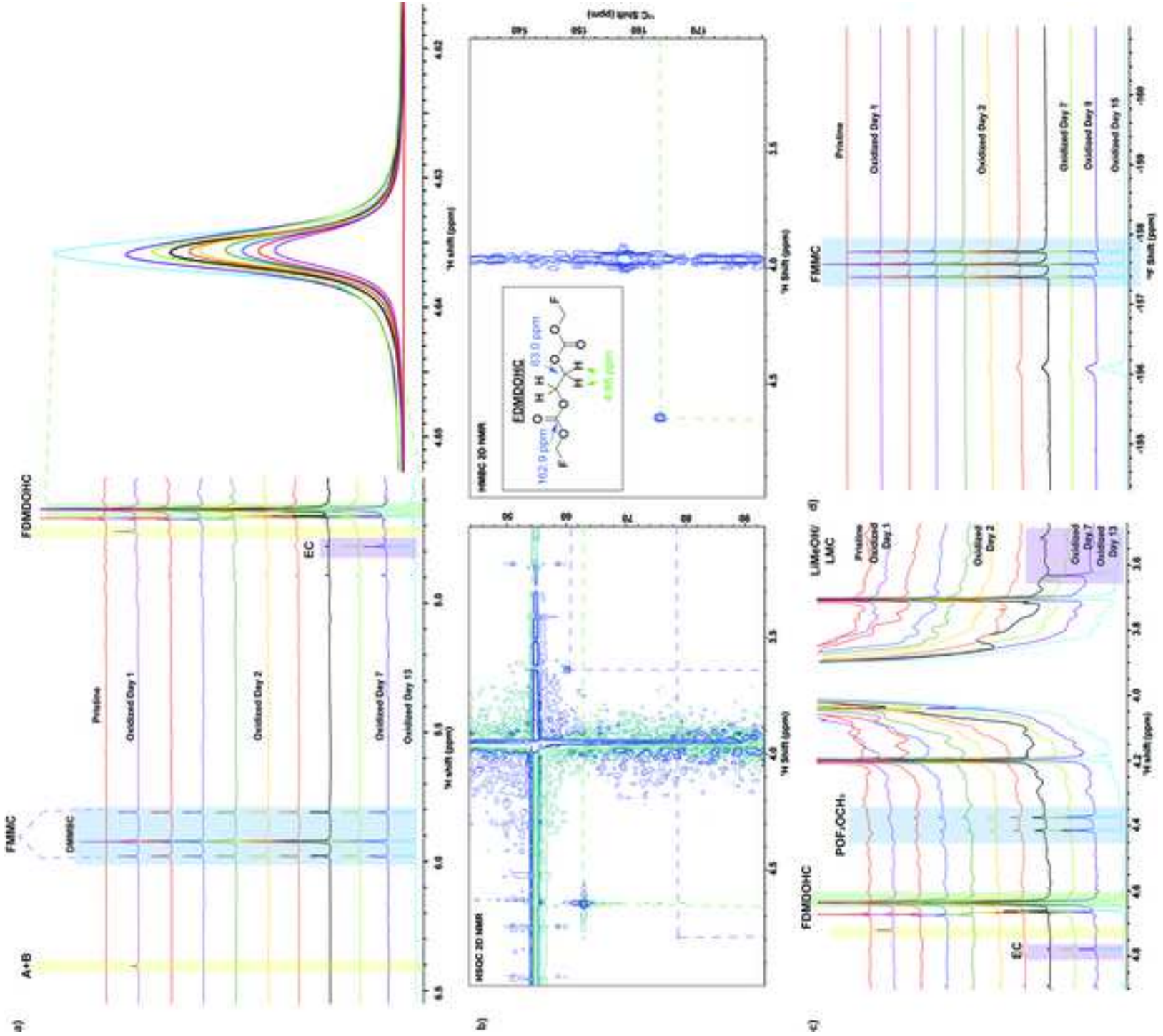

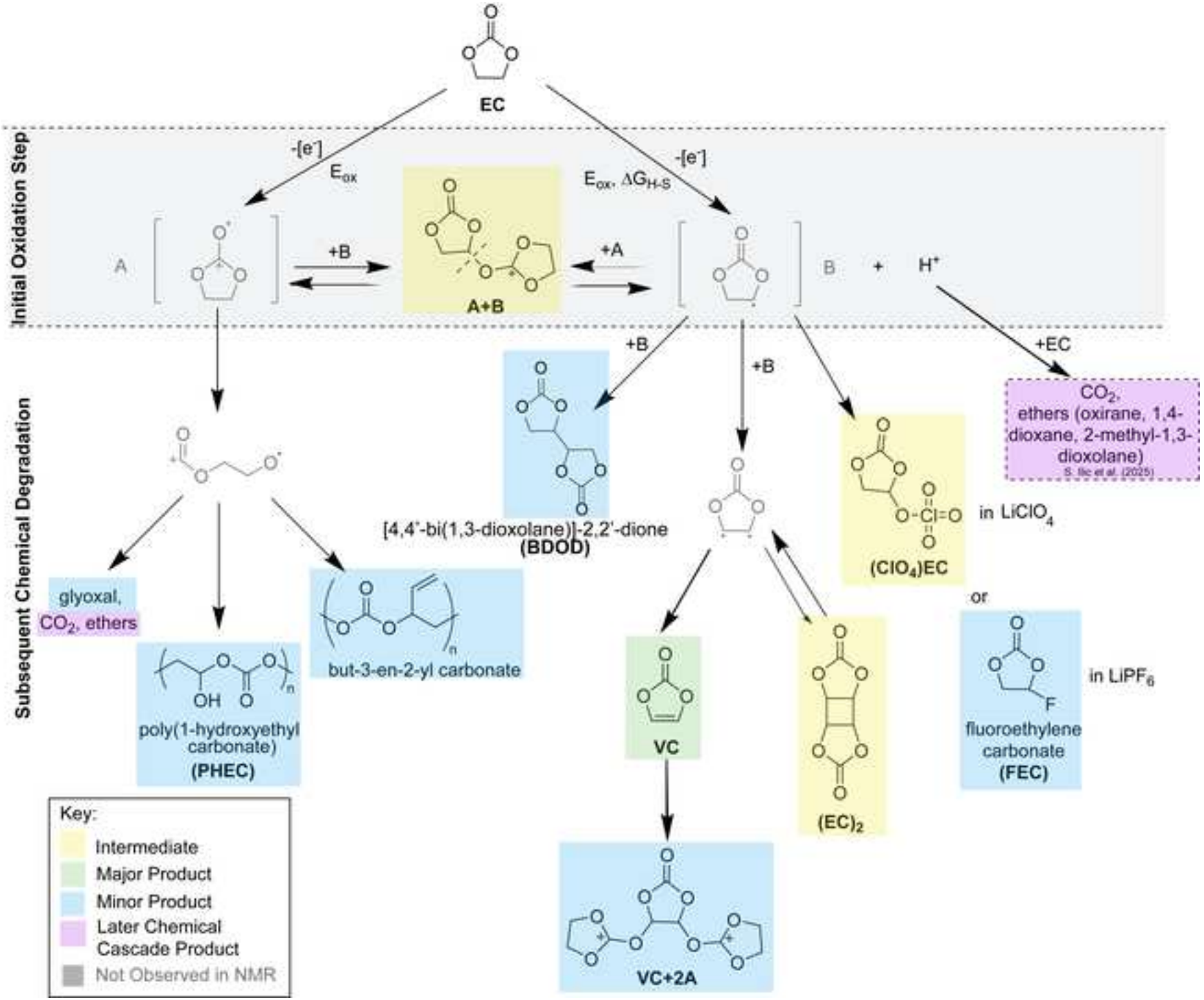

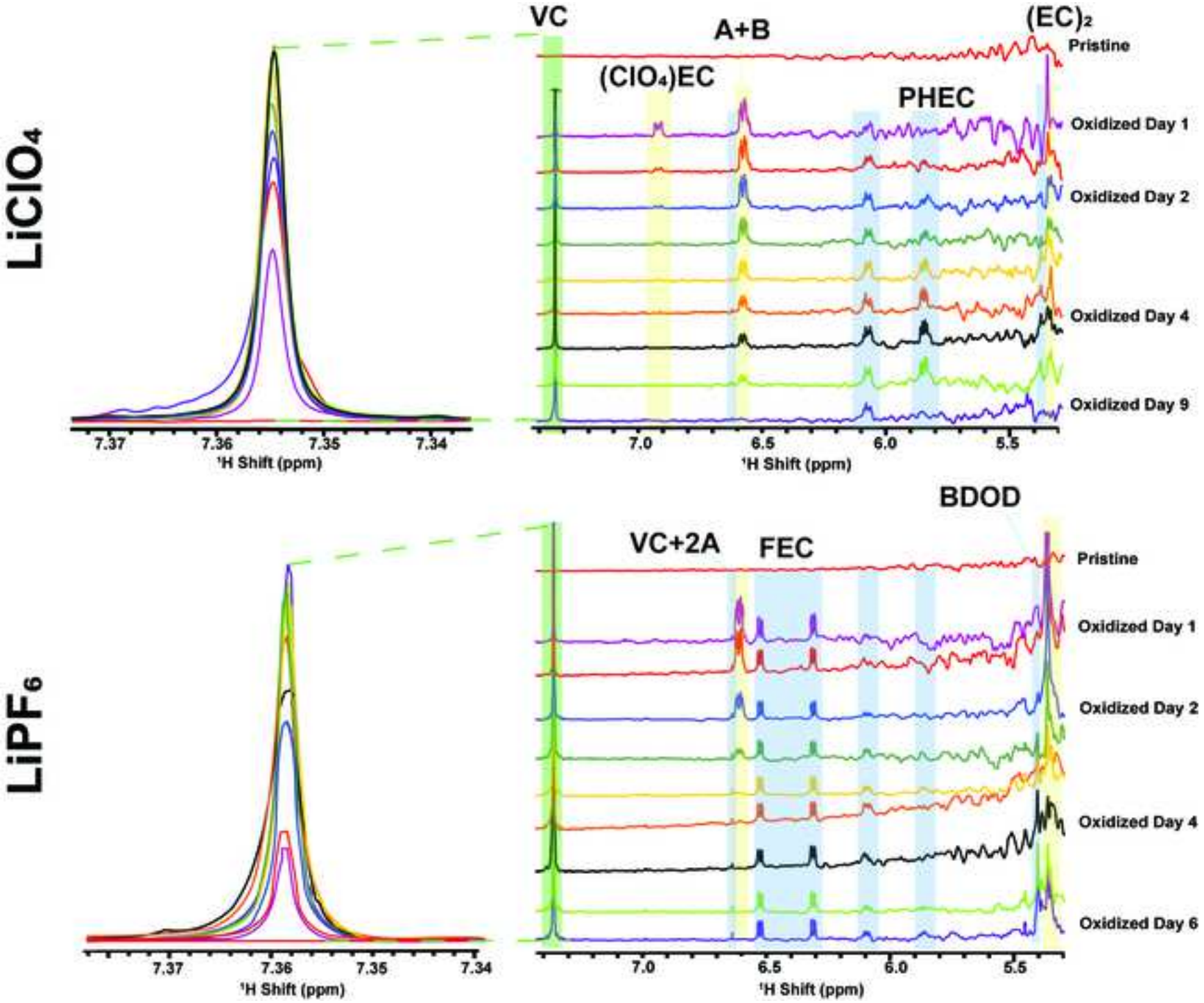

Fig8.tif

Click here to access/download;Figure;Fig8.tif

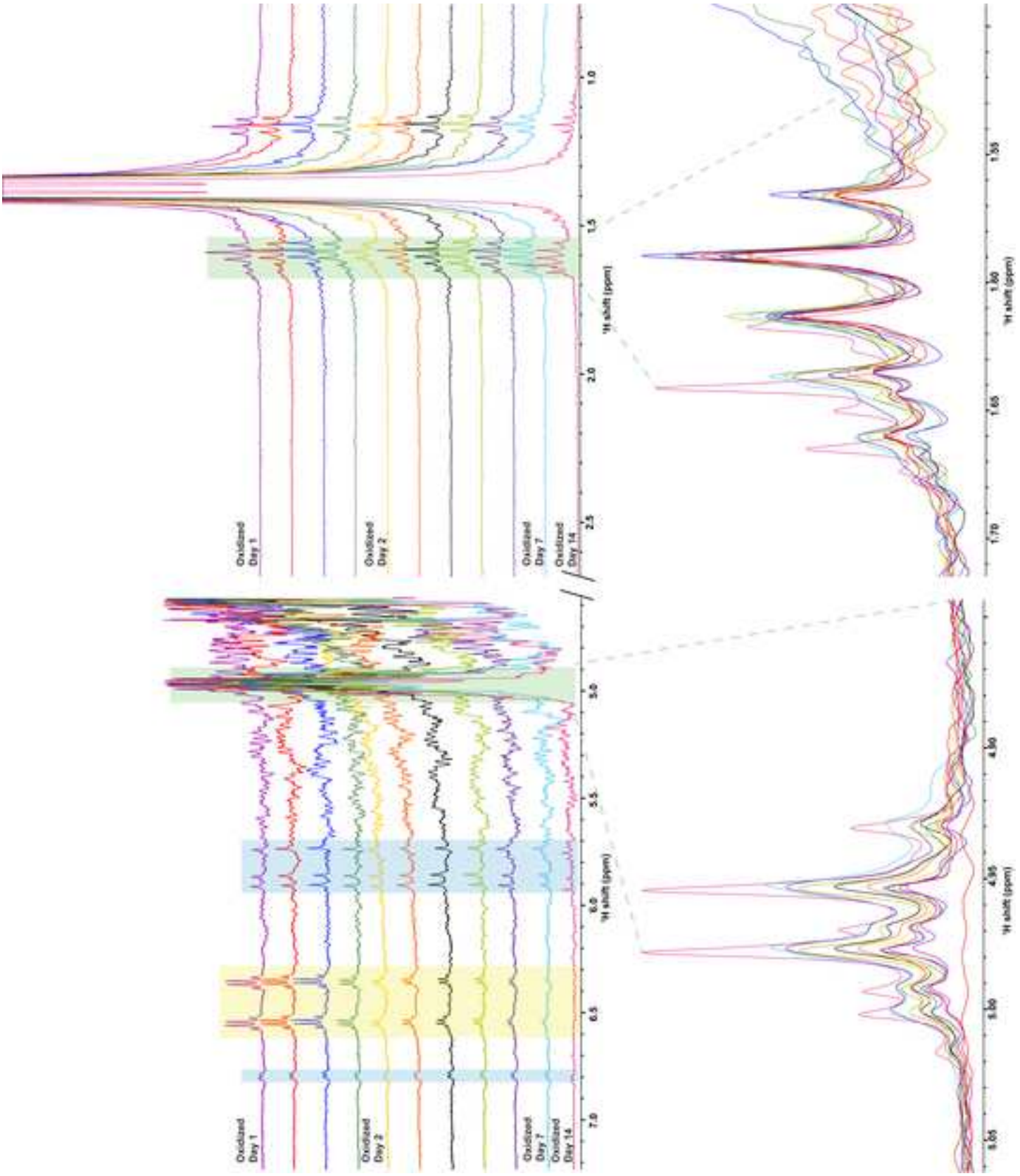

Declaration of interests

☒The authors declare that they have no known competing financial interests or personal relationships that could have appeared to influence the work reported in this paper.

☐The authors declare the following financial interests/personal relationships which may be considered as potential competing interests:

Abstract

Raising the upper cutoff voltage of lithium-ion batteries (LIBs) to increase energy density often exceeds the electrolyte's anodic stability limit, accelerating degradation and creating a major durability tradeoff. Designing electrolytes that can sustain long-term high-voltage cycling requires a clearer understanding of the fundamental mechanisms occurring when commercial carbonate solvents oxidize. To this end, simplified single-salt, single-solvent formulations of $LiClO_4$ and $LiPF_6$ in dimethyl carbonate (DMC), ethylene carbonate (EC), or ethyl methyl carbonate (EMC) were anodically electrolyzed on inert electrodes and monitored for extended periods of time using ^{1}H, ^{13}C, ^{19}F, and ^{35}Cl nuclear magnetic resonance (NMR) spectroscopy. The controlled environment of the experiments, coupled to the unique sensitivity of NMR, unveiled novel metastable intermediates and the formation of branching networks of products with temporal evolution. Oxidation of the pristine solvent primarily proceeds through a radical pathway that also produces highly reactive protons but faces competition from a second pathway involving a radical carbocation intermediate. In all cases, the intermediates follow a variety of downstream pathways that can intersect with each other. The concomitant network of reactions represents a significant increase in complexity compared to common descriptions in the literature, yet, critically, it helps explain the wide range of products typically identified in electrolyte oxidation in complete cells. The results highlight the need for refocusing fundamental research on anodic stability to analysis of the hierarchy of reaction networks to better inform efforts to mitigate the detrimental effects on battery performance, including prevention and harvesting of proton and radical products.

1.

Introduction

There is a widespread push towards improving the energy density of lithium-ion batteries through the use of cathodes operating at a high voltage such as $LiNi_{0.8}Mn_{0.1}Co_{0.1}O_2$ (NMC811) and $LiNi_{0.5}Mn_{1.5}O_4$ (LNMO) [1,2]. However, cycling to the higher voltages enabled by these cathodes often leads to rapid capacity loss and eventual cell failure [3]. These challenges can be attributed to a variety of failure mechanisms associated with processes at the cathode surface and in the electrolyte [4-7]. Unlike the SEI at the anode, the subsequent formation of cathode electrolyte interphases (CEI) is insufficient to induce electronic passivation, so the electrolyte continues to reach the electrode surface and undergoes oxidation upon cycling. Oxidation of the electrolyte contributes directly to these failure mechanisms via detrimental gas formation, generation of aggressive acidic species, and loss of ionic transport at the interface due to solvent depletion [8,9]. However, the exact hierarchy of the electrochemical and chemical reactions that build the pathways of oxidation of Li-ion battery electrolytes is only partly understood. This lack of understanding has resulted in highly empirical approaches to electrolyte design that, so far, have been unable to produce a breakthrough solution to mitigate degradation while enabling high-voltage, high-energy devices.

Degradation studies of the leading carbonate-based electrolytes have become widespread over the years, spanning experiments [7,10-13] and computations [14-16]. To date, it has been proposed that oxidation-induced breakdown of components of the electrolyte can proceed through C-H bond scission on the highly charged cathode surface [10,11,14,17], reaction with oxygen and peroxide species released during cathode phase changes [7,18-20], and interactions with radical and charged species in the electrolyte [21-23]. Yet there is still a significant lack of consensus on the inherent stability of the electrolytes at high potential, and, particularly, the relationship between the fundamental mechanism by which they can oxidize and the products of degradation observed. This outcome is not surprising when considering the chemical variability of possible solvents. In particular, the choice of salt in the oxidation study has been shown to affect the products of anodic decomposition, and studies evaluating degradation often use full cells designed for performance evaluation, which are heavily influenced by improper control of impurities, such as water, or contamination from the many components present [24-28].

The predominance of analyses of specific blends of solvents and salt makes it challenging to isolate the reactivity of each component and identify the largest culprits of degradation. As a consequence, linear carbonates like dimethyl carbonate (DMC) and ethyl methyl carbonate (EMC) are often assumed to be stable up to 5.0 V because cyclic carbonates like ethylene carbonate (EC) [29] tend to dominate behaviour in blends. A small number of reports indicate that DMC can degrade into formic acid, lithium methyl carbonate, CO_2, and organic polycarbonates [7,23,30], while EMC undergoes transesterification in the presence of lithium alkoxides to form DMC and DEC which can then further react to form additional dialkyl

carbonates [31]. However, a more complete analysis of the chemical decomposition of the linear carbonates in isolation is still necessary to understand each individual mechanism contributing to electrolyte degradation during high voltages.

Despite the comparably much greater effort on understanding the decomposition behaviour of EC, there is still no unified theory relating all of its products to specific pathways [29]. The leading mechanism in the literature involves ring-opening reactions to form glycolic acid, CO_2, oxalic acid, and long-chain oligomeric PEO-like species, although typically aided by the presence of some form of O-containing species (either as a transition metal oxide in the cathode or reactive oxygen species released during cathode phase changes) [7,19,21,32,33]. A second, less examined possibility involves EC undergoing double deprotonation to form vinylene carbonate (VC) [10,11,19] or even polymerizing to form poly-EC [13], rather than ring opening. The steps by which two hydrogen atoms can be removed simultaneously have not yet been revealed. Freiberg et al. proposed a reaction with singlet oxygen to abstract two protons and release an H_2O_2 molecule [19] whereas Zhang et al. theorized a two-step deprotonation involving a charged NMC811 surface with in-situ FTIR measurements [10]. Both paths rely on the presence of an oxide in the cell, yet previous work by our group has demonstrated the formation of VC from electrooxidized EC alone on oxide-free, inert Pt surfaces [34]. The only known mechanism that could generate VC without involvement of oxygenated species is a proposal by Shkrob et al. where they theorized that radiolysis can induce the disproportionation of two EC-generated radicals [21]. Therefore, a more in-depth tracking of the actual steps that follow EC oxidation remains necessary to understand the fundamentals of these reactions.

Electrolyte decomposition mechanisms have been analyzed with a wide variety of techniques including infrared/Raman spectroscopy [23], online electrochemical mass spectrometry (OEMS) [8], electron paramagnetic resonance (EPR) [21], and nuclear magnetic resonance (NMR) spectroscopy [7]. NMR, in particular, provides unique insight into bonding, electronegativity, and functional groups of unknown compounds, allowing for new structures and soluble decomposition products to be theorized. However, NMR shifts and identifications are highly influenced by the solvation environment and contaminants. Even the addition of deuterium-labelled solvents into the electrolyte for referencing can cause unforeseen reactions with impurities (e.g. H_2O in DMSO-d_6), leading to misleading products [35]. Therefore, careful precautions must be taken to ensure the act of measuring the sample does not influence the results. Furthermore, to minimize the complexity of the observed reactions and allow the direct measurement of specific solvent degradation mechanisms, model electrolytes on inert electrodes must be utilized. While NMR studies on inert electrodes have been performed in the past, only a handful of products were identified, resulting in an incomplete understanding of the reactions possible even in these simpler systems [23,30].

In this work, we targeted the intrinsic anodic chemistry of the most common solvents in LIBs. Model electrolytes composed of a single salt ($LiPF_6$ or $LiClO_4$) and solvent (DMC, EMC, or EC) were oxidized on an inert single crystal Pt (111) surface before being analysed with a

combination of ^{1}H, ^{13}C, ^{19}F, and ^{35}Cl NMR for dynamic tracking of species, utilizing multi-compartment, flame-sealed glass capillaries to avoid reactions between the oxidized electrolyte and the deuterium-labelled solvent. By decreasing the potential reactants to just one salt and one solvent, direct mechanistic tracing from products to oxidized intermediates became possible. The results reveal that even these simple systems undergo a network of reactions that can compete with each other. We describe their hierarchy, isolate the main paths of electrochemical versus chemical degradation, as well as label the structures of four intermediate species and four products that were previously unidentified. By identifying key moments in electrolyte solvent oxidation and chemical degradation mechanisms that lead to the most damage in the eventual cell, more effective mitigation techniques can be applied, eventually unlocking increasing voltages in Li-ion batteries.

2.

Results

Solutions of 1.3 M $LiClO_4$ or $LiPF_6$ in DMC, EC, or EMC were oxidized on either a RDE or RRDE under constant Ar flow. Electrochemical oxidation has often been reported to begin with a proton abstraction reaction [16,36]. The use of the RRDE enabled the comparison of the current density detected at the disk (Figure 1a) from solvent oxidation directly to the current measured at the ring (Figure 1b) when set at a potential to induce proton reduction to determine the proportion of electrons to protons generated in each of the three solvents (Figure 1c). RRDE has been previously discussed as a tool for investigating the electrooxidation of solvents by Hatsukade et al [37]. The formation of protons in all three solvents was further confirmed via ^{1}H NMR spectroscopy ($LiPF_6$: Figure 1d, $LiClO_4$: Figures S1-3) [34]. These highly deshielded protons appear further downfield than many reported superacids [7,38], suggesting a very aggressive chemical nature. They varied in chemical shift from 18.51 ppm for EC to 17.91 ppm and 15.00 ppm for DMC and EMC, respectively. The higher acidity in EC can be attributed to the delocalization of the remaining electron across the cyclic structure after proton removal, making the conjugate-base EC more stable and leading to increased acidity [39,40]. Upon storage, the reactive acidic proton signal shifted upfield and changed linewidth, indicating a change in its chemical environment, but, for the first week, the integrated intensity remained steady, indicating that there was no significant decrease in proton concentration during the earlier stages. Although the results presented here were performed in borosilicate glass tubes, reactive proton generation with similar trends were observed in PTFE NMR tubes containing oxidized $LiClO_4$/EC (Figure S4). In order to achieve the concentrations of species necessary to observe products in NMR, the RRDE was run for long periods, leading to the high potentials observed in Figure 1a-b; however, protons have been previously reported to form at potentials typical of standard battery cycling (~4.0V vs. Li/Li^{+}) [37].

In previous work, we found that protons generated from solvent oxidation can proceed to catalytically convert EC into CO_2 and various ether products through a ring-opening mechanism in a chemical decomposition process without an applied potential [34]. However, this proton-

promoted cascade does not fully account for the myriad of other products, like VC and FEC, often observed at these high potentials [10,19]. RRDE data (Figure 1c) measured at a range of voltages indicates that the electrochemical oxidation occurs with a proton-to-electron ratio of roughly 1:2 [37]. Given the calculated ratio, three initial electrochemical oxidation pathways have been proposed for each solvent (Figure 2) based on the most logical locations on the molecule that protons and electrons would be lost. Path A would generate a radical carbocation through the loss of a single electron (e.g. $EC^{\bullet+}$). Path B would involve the loss of a proton and an electron resulting in a neutral radical molecule (e.g. $EC^{\bullet}$). In order to achieve the observed 1:2 ratio, a combination of path A and path B would need to occur simultaneously. Path C would combine path A and path B into a single process, removing two electrons and a proton, leaving a carbocation (e.g. EC^{+}). All the proposed intermediates are expected to be highly reactive and unstable, especially the primary radicals or carbocations that would form from DMC (Figure 2a), compared to the possible ring-stabilization of EC intermediates (Figure 2b), or the secondary species in EMC (Figure 2c). Species associated with Path B have previously been proposed upon oxidation of EMC and EC on NMC811 oxide surfaces [10], but these radicals seem to be too short-lived to be observed without additional stabilization in this oxygen-free environment with no surface anchorage possible. EPR data was collected for electrolyzed EMC and EC (DMC was not measured due to the instability of the proposed primary radicals in these samples) only a few minutes after stopping the electrochemical cell, but no stable EPR-active radical species were observed. The lack of a major EPR signal (Figure S5) or any shortening in NMR relaxation times in ^{1}H NMR does not eliminate the possibility of the electrochemical paths proposed in Figure 2. Instead, it simply indicates either the concentrations of radicals were too low (in proportion to the bulk solvent) to be detected via EPR and/or the proposed free radical species are highly driven towards stable products and/or radical-free metastable intermediates, which have much longer lifetimes and can be measured via NMR. Addition of any radical trapping species for EPR measurements would more likely result in the degradation of the trap, leading to additional complications in interpreting the underlying mechanism.

The wide variety of decomposition products observed by tracking the evolution of electrolyzed solutions by ^{1}H and ^{13}C NMR 1D/2D NMR nonetheless presented commonalities in structure that enabled backtracking to common ancestors (Paths A-C) to determine a full mechanistic understanding of solvent degradation from initial oxidation onwards. The highly branched and interconnected mechanism derived from these results is contrary to the linear reaction pathways often discussed in the literature. ^{35}Cl and ^{19}F were performed to gather additional information on the influence of salt in product formation. To better understand the complex reactions occurring within each solvent, their specific mechanism of degradation is presented first, using detailed NMR spectra and reasoning based on established chemical principles, followed by a summary of the key lessons of this work. Due to the similarities in symmetry, simplicity, and overall outcomes, decomposition pathways for DMC and EC are discussed first, followed by EMC, which presented additional complexity due to its asymmetry. Our discussion decouples the main products after oxidation from those that form during subsequent chemical cascades over extended periods of time

(~1 week of storage). Furthermore, the addition of water as an impurity obscures many of the results reported below indicating how some of these products can often be masked in more complex systems.

2.1

DMC

Of the three solvents examined, dimethyl carbonate was the simplest, leading to a series of relatively straightforward decomposition peaks in the NMR spectra. The overall mechanism from DMC with $LiClO_4$ or $LiPF_6$ to products is presented in Figure 3. A tally of NMR peaks with an assignment of species, leading to Figure 3 from the data in Figure 4, is summarized in Table S1. Figure 4a presents the ^1H NMR data in a way that highlights the early species, with Figure 4b tracking the species from downstream processes. Figure 4c presents the evolution of the ^{13}C NMR for the same samples. From these results, it is clear that $DMC^{\bullet}$ (Path B) is the key intersection from which many of the subsequent products are formed while $DMC^{\bullet+}$ (Path A) mainly serves to form minor and small molecule products.

Based on ^1H peak integrations (Figure S6), the major oxidation product of $LiClO_4$/DMC is associated with a singlet at 4.62 ppm, which grows over time. Careful investigation of the ^{13}C spectra showed that peaks at 62.4 ppm and 154.8 ppm grow concurrently (Figure 4c). These peaks are consistent with methylene groups directly attached to O in a symmetric molecule like dimethyl-2,5-dioxahexanedioate (DMDOHC). DMDOHC was first proposed as a product of DMC oxidation by Moshkovich et al., with the same peaks at 4.62 ppm for ^1H and 62.4 ppm for ^{13}C [23]. Most current reports of DMDOHC generation came from studies of electrolyte formulations containing EC and $LiPF_6$ along with DMC and, therefore, attribute its formation exclusively to EC ring-opening [31,41,42]. Alternatively, this product could form from two $DMC^{\bullet}$ molecules reacting with each other at the terminal radical. In theory, an additional methyl ^1H signal should be observed around 4.01 ppm for DMDOHC, but it was likely masked by the DMC signal due to its low concentration. Indeed, no new ^1H signals were observed after purposefully adding small amounts of DMDOHC (~0.5 wt%) to pristine $LiPF_6$/DMC, without any obvious asymmetry of the DMC peak (Figure S7). Furthermore, DMDOHC can decompose into a mixture of EC and DMC in the presence of a lithium alkoxide [31,41,43]. While alkoxides were not initially observed in the oxidized electrolytes, continued chemical degradation reactions, possibly combined with slow oxygen leakage through the Teflon taping, led to the appearance of $LiOCH_3$ (^1H: 3.57 ppm, Figure 4b) after roughly a week of aging, unlocking this pathway [7]. The growth of a new singlet peak at 4.78 ppm (Figure 4a) about a week after the initial oxidation provides evidence of the generation of EC in the final solution, which was further affirmed by standard additions to pristine $LiPF_6$/DMC electrolytes (Figure S8). DMDOHC and EC signals continuously increased over the NMR observation period. Given their origin on Path B, this trend indicates that generation of $DMC^{\bullet}$ must be occurring even after oxidation has stopped. The continuous increase in $DMC^{\bullet}$ was

previously observed by EPR in a study where it was proposed to form as a secondary product from the reaction of DMC with a methyl or formyl radical from a different reaction [21].

The presence of the ^{1}H singlet at 6.45 ppm for a full day before disappearing indicates a metastable species that is eventually consumed and/or converted. When examining the ^{13}C spectra (Figure 4c), peaks at 91.2 ppm and 153.9 ppm disappeared around the same time. Together, these shifts indicate a -CH_2- functionality with two highly electronegative components adjacent on each side. Carbonate units meet this criterion, suggesting a molecule like the DMC A+B carbocation in Figure 3. DFT calculations of this A+B intermediate (Figure S9) predicted ^{1}H peaks at 6.49 ppm (^{13}C: 88.6 ppm) for the protons in the -CH_2- functionality between carbonate units, and 4.29 ppm and 4.84 ppm for the outer -CH_3 groups, in reasonable agreement with weak signals at 4.15 ppm and 4.76 ppm (Figure S10). These three peaks showed similar temporal dynamics upon storage, further supporting the assignment. Consequently, the formation of both initial intermediates in Path A and B is possible simultaneously upon oxidation. Both $DMC^{\bullet+}$ and $DMC^{\bullet}$ (Figure 2a) are too unstable in their original radical forms to be measured by NMR, especially as a paramagnetic organic species without a clear metal centre associated with them [44]. However, it is entirely plausible that they could form the metastable A+B species, thus eliminating the radicals and allowing detection via NMR. Although more stable than $DMC^{\bullet+}$ and $DMC^{\bullet}$, A+B is still a carbocation, albeit ternary, that will eventually break back apart into its constituent $DMC^{\bullet+}$ and $DMC^{\bullet}$ molecules to follow the respective product networks. An alternative structure of A+B could be theorized where the radical $O^{\bullet}$ of $DMC^{\bullet+}$ abstracts a proton from the terminal carbon of a pristine DMC molecule to generate more $DMC^{\bullet}$ [14,21]. However, this pathway seems less likely, as a protonated version of $DMC^{\bullet+}$ was not observed in these measurements.

Minor products of oxidation and associated chemical cascades were observed as the solution continued to degrade during storage. Very small amounts of HCOOH (Figure S11) were detected at 8.35 ppm (^{1}H, s) from the early stages, but without significant concentration changes after day 2 [7,45]. The only other minor product formed just after the initial oxidation step was observed at 5.97 ppm (^{1}H, s, Figure 4a) and grew in intensity until about one day after oxidation before levelling off. It is assigned as dimethyl methylene bis(carbonate) (DMMBC), first hypothesized by Moshkovich et al. [23] to arise from the reaction $DMC^{\bullet}$ with a radical methyl carbonate from the abstraction of CH_3^+ from $DMC^{\bullet+}$. DMMBC forms independent of the salt; however, further validation of this mechanism can be seen when the salt in the electrolyte is switched from $LiClO_4$ to $LiPF_6$ (discussed in more detail below), as the reaction of CH_3^+ with F generates fluoromethane in the ^{19}F spectra at -269.7 ppm (q, $^{2}J_{FH}$=46.2 Hz, Figure S12) [46,47]. As the solution continued to react over storage time, other products were generated from the continued chemical degradation of solvent molecules in the oxidized electrolyte. Besides $LiOCH_3$, lithium methyl carbonate (^{1}H singlet at 3.54 ppm in Figure 4b) was ascribed to unavoidable leaks of air into the NMR tube over time [7,43]. Finally, CO_2 was observed in the ^{13}C spectra (125.1 ppm, Figure 4c) 15 hours after oxidation, which has been widely reported as a downstream reaction product along with formic acid after DMC oxidation [7,17,23].

To determine the influence of salt on solvent-derived degradation products, $LiPF_6$/DMC was also studied. The main outcomes were very similar to $LiClO_4$/DMC (Table S1), so we focus here on the key differences. The major ^1H peaks of interest are tracked over storage time in Figure 5a-d, with peak integrations (relative to the DMC solvent peaks) plotted in Figure S13. The reactive proton generated by oxidation of $LiPF_6$/DMC appears at a higher field (17.91 ppm, Figure 1d) than in $LiClO_4$/DMC (Figure S1), suggesting a greater acidity [48]. The A+B carbocation peak at 6.45 ppm displayed seemingly accelerated dynamics, as its concentration peaks sooner than in $LiClO_4$/DMC, lasting less than 7 h. This observation hints at an increasing decomposition rate catalysed by the PF_6^- anion that increases the charge density on the carbonate moiety of A+B. This leads to more nucleophilic attacks, and thus, higher concentrations of the main decomposition product at 4.64 ppm [41].

The presence of fluorine in the electrolyte mixture also introduces new products. Present from the initial stages after oxidation, fluoromethyl methyl carbonate (FMMC) was assigned to signals at 5.94 ppm (d, $^2J_{HF}$ = 51.0 Hz, Figure 5a) and -157.6 ppm (t, $^2J_{FH}$= 51.0 Hz) (Figure 5d) in the ^1H and ^{19}F NMR, respectively, with correlated HSQC and HMBC ^{13}C 2D data (Figure S14). The methyl moiety of FMMC appeared as a small singlet peak around 4.01 ppm (Figure S15), in accordance with its proximity to DMC at 4.00 ppm. This product results from the fluorination of $DMC^{\bullet}$ [49]. A fluorinated version of DMDOHC (FDMDOHC, Figure 3) was assigned to the major ^1H peak at 4.64 ppm (s), only slightly shifted from the F-free product in $LiClO_4$/DMC, correlated to ^{13}C peaks at 63.0 and 162.9 ppm (Figure 5b). The addition of F to the terminal C should be enough to slightly deshield the inner $-CH_2-$ to cause the subtle shift. DFT simulations (Figure S16) placed them in the range of 4.38 ppm (similar to the 4.39 ppm predicted for the inner $-CH_2-$ in DMDOHC), with the terminal H adjacent to F theoretically overlapping with the FMMC peaks at 5.92 ppm. This molecule could form from linking together two subsequently deprotonated FMMC molecules or by subsequent fluorination of DMDOHC from linking two $DMC^{\bullet}$.

A closer look at the ^1H (Figure 5c) and ^{19}F spectra (Figure S17) also revealed products of decomposition of the salt over the observation period. The major fluorophosphate formed was $OPF_2(OCH_3)$, at -88.5 ppm in ^{19}F (d, J=1005.7 Hz) and 4.44 ppm in ^1H (d, J=12.1 Hz)). Wilken *et al*. predicted this product from the reaction of DMC with POF_3, also observed at -90.1 ppm (^{19}F, d, J=1066.1 Hz), itself arising from exposure of PF_5^- with trace H_2O [47]. Very small ^{19}F signals were also observed for $OPF_2(OH)$ at -84.9 ppm (d, J=975.5 Hz) and $OPF(OCH_3)_2$ at -88.3 ppm (d, J=961.0 Hz) [9,47,50]. While HF would be expected to form from PF_6^-, there were no detectable peaks in the 9.14-10.60 ppm ^1H range where a doublet would be expected [7,48]. In addition, there was only a faint, broad singlet around -191.4 ppm in the ^{19}F spectrum (Figure S18) indicating that if HF is formed, it is at very low concentrations and/or consumed. In contrast, a ^{19}F signal at -156.1 ppm (s) (Figure 5d) arose upon extended storage, indicating the formation of BF_4^- from etching of the borosilicate glass tubes by the acidic solution, likely coming from the $OPF_2(OH)$ and highly acidic proton (Figure 1d) [48].

2.2

EC

Moving from a linear symmetric molecule like DMC to a cyclic symmetric molecule like EC significantly increases the complexity of the chemical cascade products, as the ring can stabilize reactive intermediates or open to form a mixture of linear and cyclic products. However, despite the differences in products, DMC and EC have very similar initial mechanisms indicating the importance of symmetry in these early reactions. The full EC reaction mechanism is presented in Figure 6, and Table S2 summarizes all the ^{1}H NMR peaks observed and discussed below.

The ^{1}H NMR spectra of the oxidation products of both $LiClO_4$ and $LiPF_6$ in EC are displayed in Figure 7 with the overlay spectra for the major peak at 7.35 ppm expanded on the left. In fact, outside of direct anion reactions with reactive EC intermediates, almost all the reported oxidation products were observed in both $LiClO_4$ and $LiPF_6$-containing electrolytes. The only major difference was the faster growth of the main reaction products, particularly VC, in oxidized $LiPF_6$/EC (Figure S19), similar to the case of oxidized DMC [51]. Similar $LiPF_6$ hydrolysis steps were observed as in DMC with still little to no evidence of HF formation (Figure S20).

The products of EC oxidation can be sorted into two categories, ring-opened and cyclic molecules, which correspond to paths that start with one electron transfer (Path A) and one electron/proton transfer (Path B), respectively. Overall, the major oxidation product of EC is VC, which requires the net removal of two electrons and two protons. It corresponds to a ^{1}H signal at 7.35 ppm(s) and ^{13}C peaks at 134.1 ppm (HSQC) and 156.1 ppm (HMBC) (Figure S21). Its formation was further confirmed via addition of 100 mM VC into the oxidized electrolyte, resulting in an increased intensity at 7.35 ppm (Figure S22). In the literature, EC has been reported to oxidize to form VC and CO_2 separately, but with much debate over the exact mechanism [10,15,19,52]. Typically, the removal of the second proton is explained via reaction with oxygen species (singlet, peroxide, superoxide) originating from the cathode material [10,12,18,19,33]. However, such a mechanism is not possible on inert Pt electrodes used here. Instead, one of the theorized radical intermediates (Figure 2b), likely EC$^{\bullet}$, could perform a secondary radical reaction on either another EC$^{\bullet}$ or EC itself, resulting in additional proton abstractions and the formation of the alkene bond in the ring. The continuous increase in VC concentration over storage time thus implies that additional radical species must be either formed or made available for further reactions, even after electrochemical oxidation has stopped.

The continued availability of EC$^{\bullet}$ could also arise from the dynamics of an EC A+B metastable species analogous to that described for DMC. DFT predicts ^{1}H NMR shifts for the neutral ring portion of a plausible A+B intermediate at around 6.81 ppm (dd, according to traditional splitting patterns) [53] with adjacent ^{1}H at 4.92 ppm and 4.94 ppm, as well as ^{13}C peaks of 70.4 ppm, 105.7 ppm, and 153.5 ppm (Figure S23). These predictions match the ^{1}H peak at 6.59 ppm (dd, J=5.5, 1.9 Hz) with correlated peaks at 4.78 ppm and 4.95 ppm from the adjacent H in the ring structure (Figure S24) and ^{13}C shifts of 71.6 ppm, 96.8 ppm, and 156.0 ppm (Figure S25-26). The original

^{1}H peaks on the carbocation ring portion of the A+B species are predicted at 5.44 ppm, in a region where they could be masked by large noise around the EC solvent peak (Figure 7). In addition to the noise, carbocation predictions are challenging as simulations cannot perfectly reflect the complicated solution dynamics occurring in the electrolyte including the influence of salts and other ions on the conformation and positioning of the molecule, perhaps explaining the slight difference between experimental and estimated shift in the ^{13}C peak at 96.8 ppm. Still, this structure seems reasonable as Chen et al. have assigned a similar peak (6.62 ppm (dd, $^{3}J_{H-H}$= 5.6, 1.9 Hz)) to methoxyethylene carbonate (MEC), a molecule with a very similar structure [54].

Regardless of electrolyte salt, a short-lived intermediate appeared at 5.34 ppm (s) that is correlated with ^{13}C NMR peaks of 76.5 ppm (HSQC) and 169.6 ppm (HMBC) (Figures S26-27). Based on the mechanism of VC formation from EC through a double radical along Path B, this peak could be a dimerized form of EC, $(EC)_2$, from two double radical intermediates, branching away from VC formation. DFT simulation of this molecule estimates a ^{1}H chemical shift of 5.16 ppm (s) and ^{13}C peaks at 77.4 ppm and 164.5 ppm (Figure S28). Anti-parallel EC dimers have previously been observed in both solution and gas-phases using dielectric and infrared spectroscopy, respectively, and are highly dependent on surrounding solvent dynamics to determine the degree of dimerization [55,56]. Since the only solvent here is EC, it is likely stabilized enough by the other EC molecules to be observed via NMR, whether that is with actual bonding or a quasi-shared radical species between the two charged molecules. Still, the predicted molecule would experience significant amounts of ring strain, especially in the quasi-butane ring connecting the two molecules, making it highly unstable. Conversely, VC is highly stable and can be generated from the same initial diradical components. Therefore, any generated $(EC)_2$ likely breaks apart somewhat quickly to still form more VC molecules over time.

Cyclic intermediates and even minor products along Path B seemed to converge toward VC. Polymerized forms are also expected based on literature observations, but only a dimerized form of EC, [4,4'-bi(1,3-dioxolane)]-2,2'-dione (BDOD), generated from two EC$^{\bullet}$ molecules attaching at the radical position was detected after a day of storage with ^{1}H peaks around 5.37 ppm (m, J=12.1 Hz) (Figure S29) and widths similar to the literature [57,58]. Once VC has formed, it can also further react with a double addition of EC$^{\bullet+}$ across the alkene bond to form a VC+2A structure (Figures 7, S22, S30), which is ascribed to the ^{1}H signals at 6.63ppm (s) with correlated ^{13}C peaks of 98.7 ppm and 152.2 ppm (Figure S27, S31), and would offer a plausible path to polymerization. A similar branching mechanism of VC polymerization was reported by Ota et al [57].

As a radical carbocation molecule, EC$^{\bullet+}$ is predicted to favor ring opening [23]. Based on peak integrations, the ring-opened products were much more prevalent in $LiClO_4$/EC than $LiPF_6$/EC. Once opened, these molecules can undergo any number of chemical reactions, fracturing and rejoining to form new species, creating new branches of the network. Based on the shift and splitting patterns, the products at 6.08 ppm (dt, J=5.5, 2.5 Hz) and 5.83 ppm (dd, J=5.5, 2.5 Hz) are examples of polymeric species that can be generated as a result. The former can be ascribed to a proton with two H on one adjacent C (likely on the end of a double bond) and one H on the other

adjacent C while still containing a carbonate group (Figures S24-27). The result could have a similar structure to but-3-en-2-yl carbonate, although confirmation requires further study. The peak at 5.83 ppm is consistent with poly(1-hydroxyethyl carbonate) (PHEC) where an $OH^{\bullet}$ group (either from trace H_2O or from other molecule fragments) reacts on the ring-opened EC molecule to form a hydroxylated polymeric chain similar to previous reports (Figures S24-25, S31) [57,59]. Smaller molecules formed during the first NMR measurements as a result of fragmentation, including glyoxal at 9.34 ppm (s) (Figure S32) [23,60,61], CO_2, and various ether molecules at 3.72 ppm and 3.66 ppm (s) (Figure S29). CO_2 and ethers like oxirane, 1,4-dioxane, and 2-methyl-1,3-dioxolane were previously reported to form as a result of chemical (as opposed to electrochemical) decomposition of intact EC molecules, catalysed by the protons generated by the anodic process [34]. The sharp intensity increase in the 3.72 ppm and 3.66 ppm peaks after a week of storage corresponds to the generation of Li_2CO_3 and $LiOCH_3$ due to slow oxygen leakage through the Teflon tape, as discussed for DMC. EC can react with $LiOCH_3$ to form DMDOHC (or its fluorinated counterpart, FDMDOHC), which could explain the appearance of a small ^1H peak at 4.66 ppm (Figure S29).

We observed products related to the reaction of the specific electrolyte salt with $EC^{\bullet}$ after the initial oxidation. In the oxidized $LiClO_4$/EC electrolyte, a ^1H signal at 6.94 ppm (dd, J=6.0, 1.7Hz), correlated with other H at 4.90 ppm and 4.99 ppm (Figure S24) and ^{13}C at 102.6 ppm (Figure S27), was hypothesized to arise from Cl-based substitution into EC. DFT calculations for shifts of potential candidates led to (ClO_4)EC, which would produce a ^1H peak at 6.79 ppm and a correlated ^{13}C peak at 99.9 ppm (Figure S33). Due to the rapid relaxation of the ^{35}Cl nuclei, concurrent ^{35}Cl NMR (Figure S34) only showed a single broad peak, related to the coordination of the $LiClO_4$ salt with solvent molecules, that did not change over storage time [62]. However, the broad nature of this peak does not necessarily distinguish between coordinated ClO_4^- to EC and the unstable bond forming (ClO_4)EC from the anion and $EC^{\bullet}$. The bulky substituent and the poor solvation of ClO_4^- with EC [28,63] likely render the molecule highly unstable, consistent with its prominence only in the first scan and its complete disappearance after two days of storage. In contrast, $LiPF_6$ unlocked a path to the clear and sustained presence of fluorinated ethylene carbonate (FEC), with ^1H peaks at 6.42 ppm (ddd, J=64.1, 4.3, 1.1 Hz) and ^{19}F peaks centered at -124.0 ppm (dq, J=64.1 Hz) (Figure S34) [7,54].

Due to the high reactivity of the intermediates in the oxidized electrolyte, the slightest amount of contamination either from air or H_2O will steer the observations artificially away from the specific products resulting from oxidizing the electrolyte. These impurities can come from the purity of electrolyte solvents, the efficacy in sealing the samples, and, most insidiously, even the use of common deuterated NMR standards. Our experimental design avoided these issues by engineering a sample holder that allowed us to seal sample and deuterated standard free from air in separate chambers to prevent cross contamination. To highlight the importance of this design, we conducted experiments where we intentionally added 1 wt% H_2O to $LiClO_4$/EC immediately after oxidation had ceased and conducted similar ^1H NMR analyses (Figure S36). First, the

highly deshielded proton signals were absent, replaced by a broad peak around 9.10ppm, which would be consistent with a carboxylic acid instead of a highly acidic species. Second, while VC and other species were still formed, they did so at smaller concentrations in the presence of H_2O. Third, the EC A+B peak at 6.59 ppm changed shape slightly and disappeared quickly and some of the more unstable intermediates, like $(ClO_4)EC$ and $(EC)_2$, were not observed at all. Instead, the presence of H_2O induced the formation of PHEC, at 5.83 ppm, which could result from hydroxyl groups reacting with a ring-opened molecule. Overall, these observations do not necessarily mean the initial intermediates are not formed, but they were certainly masked and/or altered by other reactions in the solution, ultimately fundamentally modifying the observed pathways, distorting observations enough to potentially lead to incomplete conclusions.

2.3

EMC

The ^1H NMR spectra for oxidized $LiPF_6$/EMC are presented below in Figure 8 with the corresponding ^1H data for oxidized $LiClO_4$/EMC in Figure S37 and integrations in Figure S38. The summary of ^1H and ^{13}C data is displayed in Table S3. The change from a symmetric molecule like DMC and EC to an asymmetric molecule like EMC, increased the possible mechanism permutations because more than one type of H is available for extraction. Previous theoretical work has predicted the preferential deprotonation at the b-site in the ethyl group [10,64]. The products themselves, however, reflect the asymmetry of the molecule and include a mixture of products associated with excision of either $-CH_3$ group, similar to DMC oxidation, or $-CH_2-CH_3$ group of EMC. Out of all the solvents examined, EMC appeared to have the highest concentration of HF observable via NMR at -191.1 ppm (^{19}F, Figure S39) with increased BF_4^- glass etching and more fluorophosphate degradation species (Figure S40).

The major product in both $LiClO_4$ and $LiPF_6$/EMC appeared in the ^1H spectrum at 4.96 ppm (^{13}C peak at 75.1 ppm) and 1.70 ppm (^{13}C peak at 12.7 ppm) (Figure S41). In $LiClO_4$/EMC, these signals appeared as a clear quartet (^2J=7.2 Hz) and triplet (^2J= 7.0 Hz), respectively, indicative of a $R-O-CH_2-CH_3$ overall structure (Figure S37, S41); with smaller overlapping peaks growing in over storage time. With $LiPF_6$/EMC, the peaks became even harder to interpret because of overlap with other peaks in the same region from the first measurement. The exact structure of this molecule(s) or how it correlates to the proposed Paths in Figure 2c could not be uniquely elucidated, but some conclusions could still be drawn based on the splitting and shifts of the NMR data. To start, the molecule is likely similar in structure to EMC, but the attached R functional group would need to be more electronegative than a carbonate in order to shift the peaks downfield. In $LiPF_6$/EMC, this could potentially mean two Path B intermediates attaching at the radical site. Secondly, the small differences in peak shape and overlap between $LiClO_4$ and $LiPF_6$ can likely be attributed to the presence of fluorinated species, in analogy to DMC and EC observations. Finally, it is plausible that polymeric species were present in both salts as the electrolyzed solution became highly discoloured and opaque immediately after oxidation, giving way to a gel-like

precipitate. This precipitate was measured with ^{1}H solid-state NMR (Figure S42); however, results were inconclusive beyond that it is likely a polymeric species. In contrast, the oxidized DMC electrolyte was still transparent with only a slight yellow tint after a month of storage (Figure S43). At this point, the signal-to-noise ratio and prominence of the solvent peaks limited the detection of any possible additional peak(s) of the product(s) in solution. Future research that overcomes these experimental barriers is needed to better clarify their identity and structure.

Beyond this major product, oxidizing EMC produces many of the same species observed upon DMC oxidation, with slight differences in shift, likely due to solvation effects, and much lower intensities, likely due to competing reactions (Figure S44). It was interesting to observe the formation of the A+B intermediate identified for DMC, with a similar lifetime (~1 day of storage). The observation of some DMMBC indicates that cleavage of -O-CH_2- bond on the ethyl side is a competing process. While HCOOH was observed regardless of salt, small amounts of DMDOHC formed in $LiClO_4$, compared to the fluorinated molecules FMMC and FDMDOHC in $LiPF_6$ (Figure 8, Figure S45). These products all indicate that some form of either DMC, $DMC^{\bullet}$, or $DMC^{\bullet+}$ must be generated during EMC oxidation. While EMC has been reported to undergo either disproportionation or transesterification into DMC and DEC [41] in the presence of lithium alkoxides, no evidence of DMC or DEC was observed, unless masked by the bulk EMC, and alkoxides were not observed until after a few weeks of storage. We postulate that minor branching of the reaction involves EMC molecules fragmenting to form $DMC^{\bullet}$ (DMC Path B) and $CH_3^{\bullet}$ after deprotonation of the ethyl group [10,21], which proceed to further react. Unlike with EC, EMC appears highly unlikely to undergo a double proton abstraction due to the steric effects introduced by the additional -CH_3 group. This event would demand the formation of PC, which was never observed.

The deprotonation of the b-site H to produce $EMC^{\bullet}$ (Figure 2b) would explain the formation of 1-fluoroethyl methyl carbonate (FEMC) in $LiPF_6$ [10,64], assigned to ^{1}H peaks at 6.45 ppm (dq, J= 56.4, 5.1 Hz), highlighted in Figure 8 and S39, and at -121.8 ppm in the ^{19}F spectra (dq, J=56.7, 20.7 Hz, Figure S44, S46) [54]. FEMC slowly disappeared with storage time, indicating ongoing reaction dynamics for weeks after oxidation was stopped. The final F-containing product of EMC oxidation was at 6.80 ppm (dd, J= 5.7, 1.8 Hz), correlated with ^{1}H and ^{13}C peaks at 4.99 ppm (m, J=7.1 Hz) and 161.4 ppm, respectively (Figure S47). They appeared to be associated with a ^{19}F signal at -138.8 ppm (dt, J=55.2, 15.5 Hz) (Figure S39) based on similar intensities and peak formation after oxidation. Based on these correlations, this product was assigned as a polymeric form of FEMC (poly(FEMC)), which could further contribute to the dark discoloration and precipitates.

When H_2O was intentionally added to oxidized $LiClO_4$/EMC (Figure S48), almost all the aforementioned intermediates and products were fully quenched. The only observable was a broad peak at 6.27 ppm, which shifted upfield and narrowed over time, giving way to a sharp peak at 5.20 ppm after 10 days. This behaviour suggests that it is likely a polymeric product that is not fully dissolved in solution, but its exact identity remained unclear and warrants future investigation

[65]. The near complete disappearance of all other products indicates how even trace levels of H_2O can drastically affect which oxidation intermediates and products are observable, and even neutralize the subsequent chemical cascades catalysed by the reactive protons.

3.

Discussion

Our use of model systems using chemically inert electrodes unlocked the identification and tracking of products resulting from anodic decomposition of common alkyl carbonate solvents in Li-ion batteries, free of confounding factors associated with other battery components or simultaneous degradation processes like lattice oxygen release at the cathode. We also demonstrate that small amounts of H_2O, common in deuterated solvents used for NMR referencing [35], are sufficient to completely skew the observations away from the inherent pathways, and we propose a solution that was key for unobstructed insight. Overall, our approach allowed us to identify the key structures of four new intermediates and four new products compared to the existing body of knowledge [7,10,19]. We were able to discriminate intrinsic solvent activity from the modulation induced by interactions with the specific salt in the electrolyte and even separate salt decomposition. Even in these constrained conditions, the results highlight that the process of electrolyte oxidation is, in reality, a network of reactions with preferential and competing branches that can also cross. This fact likely makes modelling the process extremely challenging, as linear outcomes are typically assumed.

The electrochemical oxidation of all solvents studied begins the same way: electron transfer that may or may not be concurrent to proton transfer. The very high ^{1}H NMR shifts (> 14 ppm) of the protons indicate high reactivity. These acidic species are rarely reported in battery literature, likely because they can be consumed by other cell components, resulting in transition metal dissolution from the cathode, degradation of CEI products, and chemical degradation of the electrolyte producing many products commonly observed in the literature, e.g., CO_2 and a series of ether-based molecules and polymers [4,7,12,34]. Furthermore, their persistence for days after electrolysis indicates that HF and difluorophosphoric acid, observed in electrolytes containing $LiPF_6$ [9], are far from the sole acidic contributors to decomposition.

Electrochemical quantification led to three proposed initial intermediates (Figure 2). Although none of these intermediates can be directly measured with NMR because they are radicals and/or carbocations, forensic identification of the main products provided strong evidence of a preference for a combination of an initial 1-electron (Path A) and 1-electron/1-proton step (Path B). No evidence of molecules that could be tracked to Path C was found. The main products of oxidation in DMC ((F)DMDOHC) and EC (VC) provided the clearest evidence of the existence of Path B. The fluorination of solvent molecules to form FMMC, FEC, and FEMC further implied the preferential deprotonation at specific locations. The existence of Path B indirectly indicates that Path A must also be followed to produce the 2:1 ratio measured via RRDE. In both DMC and EC, metastable intermediates conceivably assembled from the initial intermediates of Path A and B

further support this conclusion. Molecules solely associated with Path A were slightly more challenging to confirm, with downstream products like DMMBC and CO_2 suggesting that chemical evolution is rapid along this pathway. Importantly, not only do competing pathways build a complex network of products, but the fact that they can cross is key to realizing that the damage continues even when the electrolyte is no longer under applied potentials.

The solvents begin to diverge mechanistically after the formation of the initial intermediates. DMC and EC are the simplest forms of their respective class of carbonates (linear and cyclic) and are fully symmetric. There are few possible positions on the molecule where permutations could occur, which leads to very predictable reactions. While they follow largely equivalent pathways, DMC creates fewer and more straightforward products, whereas EC can undergo either ring-opening mechanisms to form polymers along Path A or maintain a ring structure with additional substituents or changes along Path B. The greater stabilization of the ring via delocalized electron density endows the associated intermediates with longer lifetimes, and, thus, measurement prevalence. When an asymmetric molecule like EMC is oxidized, the complexity of the reaction networks increases because a variety of branches are unlocked, including fracturing or functionalization on either side of the molecule. This leads to a mixture reminiscent of the DMC outcomes, plus additional species that include ethyl groups. It is rather trivial to extrapolate that further increasing molecular complexity will scale the complexity of the reaction network, which explains the challenges identifying the products of propylene carbonate (PC) oxidation in the literature [16,21,28]. It is likely that resolution of these challenges will demand combined approaches based on experiments and computational modelling of the reaction explicitly as a network [66].

It is worth pondering the effects of the observed products on the overall health of a battery. At first glance, some of the products formed may seem beneficial to cycling. VC, for example, has been widely included in the electrolyte as a sacrificial additive to form a polymeric CEI and prevent surface reconstruction [6,67]. In the case of DMC, there is still some debate over the role of DMDOHC, with conflicting reports of high viscosity and poor conductivities contrasting with a role avoiding detrimental gas formation upon cycling at high temperature [46,47,68]. Regardless of outcomes, formation of these two products from EC and DMC demands the simultaneous generation of highly reactive protons and their degradation cascades, which would likely negate any benefits they may provide [34].

With the clarity on the mechanisms involved in anodic decomposition in hand, we can tackle an important question: what can be done to stop the oxidation of the electrolyte entirely? Ideally, solvents would be available that simply withstand the potentials at which these alkylcarbonates react, which can be as low as 4.3 V vs. Li^+/Li^0 depending on the metric chosen [34], without penalty along the other requirements for device function, like electrode passivation, current collector stability, viscosity and ionic conductivity [29]. An alternative route involves the use of additives that can act as a radical trap of the initial intermediates or that can target most harmful products in the reaction mechanism. At a fundamental level, the first approach would offer the most

comprehensive solution by tackling the earliest intermediates in the network, but it is unclear that traps exist that are themselves stable at these potentials. At the other end, proton scavengers would prevent chemical degradation breakdown of the solvent into CO_2 and ether species. It is possible that these additives can take the form of molecules in the electrolyte or coatings on the electrode. Outside of electrolyte manipulation, these decomposition pathways could also be halted by simply avoiding the onset potential of proton formation. Ultimately, a multi-pronged approach is likely to be necessary to preventing or alleviating the effects of anodic decomposition, considering the complex network of reactions and the possibility that only the balance of branches is altered.

4.

Conclusions

Anodic decomposition of the electrolyte at high voltages in Li-ion batteries is fundamental to the challenge of durability, especially when high energy density is needed, so establishing their chemical underpinnings is essential. Through a combination of experimental and computational NMR on model electrolyte systems in controlled environments, we isolate the inherent pathways of decomposition of three leading solvents in commercial batteries, DMC, EC and EMC. The approach uncovered key, previously unknown intermediates that allowed us to reconstruct the complex network of reactions associated with the electrochemical process. In all cases, the initial step involves a combination of 1-electron and 1-electron/1-proton transfer, an early onset of branching. Subsequent downstream chemistry depends highly on the symmetry and complexity of the molecule. In symmetric molecules, the continued formation of small molecules is enabled by the formation of metastable intermediates that can fragment to continue to drive chemical degradation. Molecular asymmetry scales the complexity of the reaction network, making it much harder to predict and elucidate. Molecular complexity acts as another factor in network branching, as demonstrated by linear DMC leading to significantly less products than cyclic EC. The results lay bare the complexity of solvent oxidation at high voltages. By systematically isolating each component of the electrolyte and mapping the whole network, this knowledge will guide fresh approaches to mitigation of degradation that more precisely target specific intermediate stages and arrest the worst outcomes, especially when moving towards more complex, multi-solvent systems with battery electrode materials. Central to this goal will be strategies that can prevent the formation or reactivity of protons in the first place, since all reactions appear to be downhill after their formation. The potential payoff in the form of transformational energy density and lifetime demand a renewed effort to translate mechanistic knowledge into sophisticated molecular design.

5.

Experimental Methods

5.1

Electrodes and electrolytes. For rotating disc electrode (RDE) and rotating ring disc electrode (RRDE) measurements, Pt (111) single crystal disk (6 mm diameter) electrodes were used. Prior to assembling the Pt (111) disk into the RDE or RRDE holder (Pine Research Instrumentation), its surface was conditioned by inductive heating for 7 min at 1050 °C in an argon-hydrogen flow (3 % hydrogen) and cooled slowly to room temperature under the inert atmosphere. Before assembling into RDE or RRDE and during the transfer, the surface of the Pt (111) was protected from oxidation and surface contamination with a droplet of deionized water (Milli-Q system). The difference between the RDE and RRDE holder is that the latter has a Pt ring with inner and outer diameter of approximately 7.5 and 8.5 mm, respectively. The Pt ring surface was prepared by mechanical polishing using SiC paper (1200 grit, Buehler), then rinsed and dried.

The electrolytes were prepared in the Ar-filled glove box by mixing $LiClO_4$ (battery grade, 99.99 % trace metal, Sigma Aldrich), which was dried under dynamic vacuum in the glass oven at 150 °C for 150 h, or $LiPF_6$ (BASF), which was also dried under dynamic vacuum at 120 °C, with ethylene carbonate, dimethyl carbonate or ethyl methyl carbonate (Gotion). The electrolytes had a water content of less than 10 ppm H_2O. All electrolytes were stored in FEP bottles and prepared fresh for all experiments.

5.2

Electrochemical cells for RDE and RRDE analyses. A flooded cell configuration was used for RDE and RRDE measurements. The electrochemical cell was assembled in a three-electrode glass configuration, where a Pt-wire and a Li-metal were used as counter electrode and reference electrode, respectively, inside an Ar-filled glove box (VAC, < 0.2 ppm O_2, < 0.5 ppm H_2O). The electrolyte volume was between 7 mL and 9 mL for RDE and between 35 mL and 45 mL for RRDE (purged with Ar gas).

5.3

Electrochemical protocols. The electrochemical experiments were performed inside an Ar-filled glovebox (VAC, < 0.2 ppm O_2, < 0.5 ppm H_2O) equipped with feedthroughs for gas lines and for electrical connections to a potentiostat located externally (Autolab PGSTAT302N, Metrohm). Measurements were conducted in a custom glass cell, which was dried overnight at 180 °C under vacuum in the antechamber and then directly put inside the glovebox. The cell had a Luggin capillary in which to place the reference electrode (lithium metal) near the working electrode, as well as a frit that separated the counter electrode (platinum wire) from the main compartment. The cell resistance was measured by electrochemical impedance spectroscopy and the potential was manually post-corrected for the ohmic losses. 90 % IR drop correction was used in all electrochemical measurements. The samples for NMR analysis were generated by passing 45 coulombs of charge through the electrolyte galvanostatically at 10mA output current using a Pt (111) electrode at 900 rpm rotation rate.

5.4

NMR analysis. Electrochemically oxidized electrolytes consisting of one salt ($LiClO_4$ or $LiPF_6$) and one solvent (DMC, EC, or EMC) were measured using ^{1}H, ^{13}C, ^{19}F, and ^{35}Cl NMR spectroscopy on a 300MHz Bruker Avance III HD spectrometer with an ATMA BBO probe. 2D NMR was performed including ^{1}H-^{1}H Homonuclear Correlation Spectroscopy (COSY), ^{1}H-^{13}C Heteronuclear Single Quantum Coherence (HSQC), and Heteronuclear Multiple Bond Correlation (HMBC) using the same spectrometer. All NMR samples were prepared in an argon-filled glovebox with flame sealed glass capillary inserts containing deuterated water (D_2O) as an external reference at 4.67 ppm. Each NMR tube was double sealed with Teflon tape to allow for extended measurements over time at room temperature in the atmosphere. The time between the end of the electrolyte oxidation and the first NMR spectroscopy measurement was roughly 20 minutes. NMR measurements were taken constantly for three straight days and then periodically for a minimum of three weeks. All NMR measurements were performed at room temperature. Solid-state MAS NMR measurements were performed on a 300MHz Bruker Avance III spectrometer using a 3.2 mm zirconium rotor at a spinning speed of 20kHz.

5.5

EPR analysis. Continuous wave (cw) X-band (9.5 GHz) electron paramagnetic resonance (EPR) measurements were conducted using a Bruker ELEXSYS II E500 spectrometer equipped with a rectangular TE_{102} resonator (Bruker ER 4102ST). All EPR measurements were performed at cryogenic temperatures, which was provided by liquid helium gas-flow cryostat (ICE Oxford, UK) and an ITC temperature controller (Oxford Instruments, UK).

5.6

DFT calculations. DFT calculations were conducted using an ab initio quantum chemistry program, ORCA 5.0.4 [69]. The molecular configuration was first optimized based on Universal Force Field (UFF) implemented in a molecule editor and visualizer software, Avogadro, before further optimization at ωB97M-V/ cc-pVQZ/JK level [70]. The chemical shielding tensors and J-coupling tensors were calculated with the B3LYP density functional in conjunction with the pcSseg-n basis set and solvent effects accounted for using the Conductor-like Polarizable Continuum Model (CPCM) based on the dielectric constant and refraction index of EC solution with approximately 1 M of Li salt [71-72]. The shielding values were then converted to predicted chemical shifts with a calibration factor determined by the difference between experimental and calculated chemical shifts of the primary solvent molecule (DMC, EC, etc.) then verified by comparing known products like VC, FEC, and FMMC. Due to the inherent gap in complexity between the modeled systems of electrolyte used in DFT calculations compared to those measured experimentally that contain a host of other species that can affect the solvation structure of the molecule of interest, perfect alignment of simulation and measured is unlikely. Therefore, based on comparisons of species identified via other methods to their predicted shifts, a ±0.3 ppm error range of ^{1}H simulations and ±5.0 ppm error range of ^{13}C simulations has been implemented. Predicted structures were visualized using VESTA [73].

Additional figures, text, and data are provided in the Supplemental Information.

References

[1] J. Xiang, Y. Wei, Y. Zhong, Y. Yang, H. Cheng, L. Yuan, H. Xu and Y. Huang, Building Practical High-Voltage Cathode Materials for Lithium-Ion Batteries, Adv. Mater. 34 (2022) 2200912. https://doi.org/10.1002/adma.202200912.

[2] L. Madec and L. D. Ellis, Exploring interactions between electrodes in $Li[Ni_xMn_yCo_{1-x-y}]O_2$/graphite cells through electrode/electrolyte interfaces analysis, J. Electrochem. Soc. 164 (2017) A3718–A3726. https://doi.org/10.1149/2.1011714jes.

[3] S. C. Jung, D. S. Jung, J. W. Choi and Y.-K. Han, Atom-level understanding of the sodiation process in silicon anode material, J. Phys. Chem. Lett. 5 (2014) 1283–1288. https://doi.org/10.1021/jz5002743.

[4] B. Strehle, K. Kleiner, R. Jung, F. Chesneau, M. Mendez, H. A. Gasteiger and M. Piana, The role of oxygen release from Li- and Mn-rich layered oxides during the first cycles investigated by on-line electrochemical mass spectrometry, J. Electrochem. Soc. 164 (2017) A400–A406. https://doi.org/10.1149/2.1001702jes.

[5] L. Rynearson, C. Antolini, C. Jayawardana, M. Yeddala, D. Hayes and B. L. Lucht, Speciation of transition metal dissolution in electrolyte from common cathode materials, Angew. Chem. Int. Ed. 63 (2024) e202317109. https://doi.org/10.1002/anie.202317109.

[6] H. Dai, L. Gomes, D. Maxwell, S. Zamani, K. Yang, D. Atienza, N. Dale and S. Mukerjee, Exploring the role of an electrolyte additive in suppressing surface reconstruction of a Ni-rich NMC cathode at ultrahigh voltage via enhanced in situ and operando characterization methods, ACS Appl. Mater. Interfaces 16 (2024) 8639–8654. https://doi.org/10.1021/acsami.3c15670.

[7] B. L. D. Rinkel, D. S. Hall, I. Temprano and C. P. Grey, Electrolyte oxidation pathways in lithium-ion batteries, J. Am. Chem. Soc. 142 (2020) 15058–15074. https://doi.org/10.1021/jacs.0c06363.

[8] M. Metzger, P. Walke, S. Solchenbach, G. Salitra, D. Aurbach and H. A. Gasteiger, Evaluating the high-voltage stability of conductive carbon and ethylene carbonate with various lithium salts, J. Electrochem. Soc. 167 (2020) 160522. https://doi.org/10.1149/1945-7111/abcabd.

[9] C. Jayawardana, N. Rodrigo, B. Parimalam and B. L. Lucht, Role of electrolyte oxidation and difluorophosphoric acid generation in crossover and capacity fade in lithium-ion batteries, ACS Energy Lett. 6 (2021) 3788–3792. https://doi.org/10.1021/acsenergylett.1c01657.

[10] Y. Zhang, Y. Katayama, R. Tatara, L. Giordano, Y. Yu, D. Fraggedakis, J. G. Sun, F. Maglia, R. Jung, M. Z. Bazant and Y. Shao-Horn, Revealing electrolyte oxidation via carbonate dehydrogenation on Ni-based oxides in Li-ion batteries by in situ FTIR spectroscopy, Energy Environ. Sci. 13 (2020) 183–199. https://doi.org/10.1039/C9EE02543J.

[11] B. L. D. Rinkel, J. P. Vivek, N. Garcia-Araez and C. P. Grey, Two electrolyte decomposition pathways at nickel-rich cathode surfaces in lithium-ion batteries, Energy Environ. Sci. 15 (2022) 3416–3438. https://doi.org/10.1039/D1EE04053G.

[12] R. Jung, M. Metzger, F. Maglia, C. Stinner and H. A. Gasteiger, Chemical versus electrochemical electrolyte oxidation on NMC111, NMC622, NMC811, LNMO, and conductive carbon, J. Phys. Chem. Lett. 8 (2017) 4820–4825. https://doi.org/10.1021/acs.jpclett.7b01927.

[13] L. Yang, B. Ravdel and B. L. Lucht, Electrolyte reactions with the surface of high voltage $LiNi_{0.5}Mn_{1.5}O_4$ cathodes for lithium-ion batteries, Electrochem. Solid-State Lett. 13 (2010) A95–A98. https://doi.org/10.1149/1.3428515.

[14] O. Borodin, W. Behl and T. R. Jow, Oxidative stability and initial decomposition reactions of carbonate, sulfone, and alkyl phosphate-based electrolytes, J. Phys. Chem. C 117 (2013) 8661–8682. https://doi.org/10.1021/jp400527c.

[15] L. Xing and O. Borodin, Oxidation-induced decomposition of ethylene carbonate from DFT calculations: importance of explicitly treating surrounding solvent, Phys. Chem. Chem. Phys. 14 (2012) 12838–12843. https://doi.org/10.1039/C2CP41103B.

[16] L. Xing, O. Borodin, G. D. Smith and W. Li, Density functional theory study of the role of anions on the oxidative decomposition reaction of propylene carbonate, J. Phys. Chem. A 115 (2011) 13896–13905. https://doi.org/10.1021/jp206153n.

[17] L. Huai, Z. Chen and J. Li, Degradation mechanism of dimethyl carbonate dissociation on the $LiCoO_2$ cathode surface: a first-principles study, ACS Appl. Mater. Interfaces 9 (2017) 36377–36384. https://doi.org/10.1021/acsami.7b09352.

[18] E. W. C. Spotte-Smith, S. Vijay, T. B. Petrocelli, B. L. D. Rinkel, B. D. McCloskey and K. A. Persson, A critical analysis of chemical and electrochemical oxidation mechanisms in Li-ion batteries, J. Phys. Chem. Lett. 15 (2024) 391–400. https://doi.org/10.1021/acs.jpclett.3c03279.

[19] A. T. S. Freiberg, M. K. Roos, J. Wandt, R. de Vivie-Riedle and H. A. Gasteiger, Singlet oxygen reactivity with carbonate solvents used for Li-ion battery electrolytes, J. Phys. Chem. A 122 (2018) 8828–8839. https://doi.org/10.1021/acs.jpca.8b08079.

[20] B. L. D. Rinkel, R. S. Mohanakrishnan, J. Lee, K. A. Persson and B. D. McCloskey, Reactivity of cyclic and linear alkyl carbonates with reactive oxygen species, J. Am. Chem. Soc. 147 (2025) 12089–12098. https://doi.org/10.1021/jacs.5c12089.

[21] I. A. Shkrob, Y. Zhu, T. W. Marin and D. Abraham, Reduction of carbonate electrolytes and the formation of solid-electrolyte interface (SEI) in lithium-ion batteries. 1. Spectroscopic observations of radical intermediates generated in one-electron reduction of carbonates, J. Phys. Chem. C 117 (2013) 19255–19269. https://doi.org/10.1021/jp406274e.

[22] I. A. Shkrob, Y. Zhu, T. W. Marin and D. Abraham, Reduction of carbonate electrolytes and the formation of solid-electrolyte interface (SEI) in lithium-ion batteries. 2. Radiolytically induced polymerization of ethylene carbonate, J. Phys. Chem. C 117 (2013) 19270–19279. https://doi.org/10.1021/jp406273p.

[23] M. Moshkovich, M. Cohocaru, H. E. Gottlieb and D. Aurbach, The study of the anodic stability of alkyl carbonate solutions by in situ FTIR spectroscopy, EQCM, NMR, and MS, J. Electroanal. Chem. 497 (2001) 84–96. https://doi.org/10.1016/S0022-0728(00)00457-5.

[24] R. Wagner, M. Korth, B. Streipert, J. Kasnatscheew, D. R. Gallus, S. Brox, M. Amereller, I. Cekic-Laskovic, M. Winter and K. U. Schwenke, Impact of selected $LiPF_6$ hydrolysis products on the high-voltage stability of lithium-ion battery cells, ACS Appl. Mater. Interfaces 8 (2016) 30871–30878. https://doi.org/10.1021/acsami.6b09164.

[25] S. E. Sloop, J. K. Pugh, S. Wang, J. B. Kerr and K. Kinoshita, Chemical reactivity of PF_5 and $LiPF_6$ in ethylene carbonate/dimethyl carbonate solutions, Electrochem. Solid-State Lett. 4 (2001) A42–A44. https://doi.org/10.1149/1.1353158.

[26] L. Hartmann, L. Reuter, L. Wallisch, A. Beiersdorfer, A. Adam, D. Goldbach, T. Teufl, P. Lamp, H. A. Gasteiger and J. Wandt, Depletion of electrolyte salt upon calendar aging of lithium-ion batteries and its effect on cell performance, J. Electrochem. Soc. 171 (2024) 060506. https://doi.org/10.1149/1945-7111/ad4821.

[27] J.-M. Tarascon and D. Guyomard, New electrolyte compositions stable over the 0 to 5 V voltage range and compatible with the $Li_{1+x}Mn_2O_4$/carbon Li-ion cells, Solid State Ion. 69 (1994) 293–305. https://doi.org/10.1016/0167-2738(94)90418-9.

[28] G. Eggert and J. Heitbaum, Electrochemical reactions of propylene carbonate and electrolytes solved therein—a DEMS study, Electrochim. Acta 31 (1986) 1443–1448. https://doi.org/10.1016/0013-4686(86)87057-8.

[29] K. Xu, Nonaqueous liquid electrolytes for lithium-based rechargeable batteries, Chem. Rev. 104 (2004) 4303–4418. https://doi.org/10.1021/cr030203g.

[30] I. Azcarate, W. Yin, C. Méthivier, F. Ribot, C. Laberty-Robert and A. Grimaud, Assessing the oxidation behavior of EC:DMC-based electrolyte on non-catalytically active surfaces, J. Electrochem. Soc. 167 (2020) 080530. https://doi.org/10.1149/1945-7111/ab8f57.

[31] H. Yoshida, T. Fukunaga, T. Hazama, M. Terasaki, M. Mizutani and M. Yamachi, Degradation mechanism of alkyl carbonate solvents used in lithium-ion cells during initial

charging, J. Power Sources 68 (1997) 311–315. https://doi.org/10.1016/S0378-7753(97)02635-9.

[32] J. Henschel, C. Peschel, S. Klein, F. Horsthemke, M. Winter and S. Nowak, Clarification of decomposition pathways in a state-of-the-art lithium-ion battery electrolyte through ^{13}C labeling of electrolyte components, Angew. Chem. Int. Ed. 59 (2020) 6128–6137. https://doi.org/10.1002/anie.202000727.

[33] R. C. McNulty, K. D. Jones, B. M. G. Denison, E. Hampson, I. Temprano, D. A. Walsh, H. W. Lam, G. N. Newton, W. M. Dose, C. P. Grey and L. R. Johnson, Singlet oxygen is not the source of ethylene carbonate degradation in nickel-rich Li-ion cells, Energy Environ. Sci. 18 (2025) 7603–7609. https://doi.org/10.1039/D5EE00956A.

[34] S. Ilic, M. Martins, H. Liu, P. F. B. D. Martins, D. Haering, J. Yang, T. Hatsukade, B. Genorio, S. E. Weitzner, L.-F. Wan, Z. Zhang, J. G. Connell, B. Key, J. Cabana and D. Strmcnik, An unwanted guest in the electrochemical oxidation of high-voltage Li-ion battery electrolytes: the life of highly reactive protons, Energy Environ. Sci. 18 (2025) 8303–8312. https://doi.org/10.1039/D5EE02403J.

[35] G. R. Fulmer, A. J. M. Miller, N. H. Sherden, H. E. Gottlieb, A. Nudelman, B. M. Stoltz, J. E. Bercaw and K. I. Goldberg, NMR chemical shifts of trace impurities: common laboratory solvents, organics, and gases in deuterated solvents relevant to the organometallic chemist, Organometallics 29 (2010) 2176–2179. https://doi.org/10.1021/om100106e.

[36] P. R. D. Murray, J. H. Cox, N. D. Chiappini, C. B. Roos, E. A. McLoughlin, B. G. Hejna, S. T. Nguyen, H. H. Ripberger, J. M. Ganley, E. Tsui, N. Y. Shin, B. Koronkiewicz, G. Qiu and R. R. Knowles, Photochemical and electrochemical applications of proton-coupled electron transfer in organic synthesis, Chem. Rev. 122 (2022) 2017–2291. https://doi.org/10.1021/acs.chemrev.1c00374.

[37] T. Hatsukade, M. Zorko, D. Haering, N. M. Marković, V. R. Stamenković and D. Strmcnik, Detection of protons using the rotating ring-disk electrode method during electrochemical oxidation of battery electrolytes, Electrochem. Commun. 120 (2020) 106785. https://doi.org/10.1016/j.elecom.2020.106785.

[38] S. K. Davidowski, F. Thompson, W. Huang, M. Hasani, S. A. Amin, C. A. Angell and J. L. Yarger, NMR characterization of ionicity and transport properties for a series of diethylmethylamine-based protic ionic liquids, J. Phys. Chem. B 120 (2016) 4279–4285. https://doi.org/10.1021/acs.jpcb.6b01203.

[39] W. M. Dose, W. Li, I. Temprano, C. A. O'Keefe, B. L. Mehdi, M. F. L. De Volder and C. P. Grey, Onset potential for electrolyte oxidation and Ni-rich cathode degradation in lithium-ion batteries, ACS Energy Lett. 7 (2022) 3524–3530. https://doi.org/10.1021/acsenergylett.2c01722.

[40] X. Liu, Structural effects on acidity and basicity, in Organic Chemistry I, Kwantlen Polytechnic University, Surrey, BC, 2021.

[41] T. Sasaki, T. Abe, Y. Iriyama, M. Inaba and Z. Ogumi, Formation mechanism of alkyl dicarbonates in Li-ion cells, J. Power Sources 150 (2005) 208–215. https://doi.org/10.1016/j.jpowsour.2005.02.021.

[42] T. Taskovic, A. Adamson, A. Clarke, E. D. Alter, A. Eldesoky, K. L. Gering, K. Tuul and J. R. Dahn, Alkyl dicarbonates, common electrolyte degradation products, can enable long-lived Li-ion cells at high temperatures, J. Electrochem. Soc. 170 (2023) 090527. https://doi.org/10.1149/1945-7111/acf886.

[43] G. Gachot, S. Grugeon, M. Armand, S. Pilard, P. Guenot, J.-M. Tarascon and S. Laruelle, Deciphering the multi-step degradation mechanisms of carbonate-based electrolyte in Li batteries, J. Power Sources 178 (2008) 409–421. https://doi.org/10.1016/j.jpowsour.2007.11.110.

[44] A. J. Pell, G. Pintacuda and C. P. Grey, Paramagnetic NMR in solution and the solid state, Prog. Nucl. Magn. Reson. Spectrosc. 111 (2019 1–271. https://doi.org/10.1016/j.pnmrs.2018.05.001.

[45] I. Berregi, G. del Campo, R. Caracena and J. I. Miranda, Quantitative determination of formic acid in apple juices by ^{1}H NMR spectrometry, Talanta 72 (2007) 1049–1053. https://doi.org/10.1016/j.talanta.2006.12.031.

[46] F. J. Weigert, Fluorine magnetic resonance spectra of monofluoro- and difluoro-substituted hydrocarbons, J. Org. Chem. 45 (1980) 3476–3483. https://doi.org/10.1021/jo01305a022.

[47] S. Wilken, M. Treskow, J. Scheers, P. Johansson and P. Jacobsson, Initial stages of thermal decomposition of $LiPF_6$-based lithium-ion battery electrolytes by detailed Raman and NMR spectroscopy, RSC Adv. 3 (2013) 16359–16369. https://doi.org/10.1039/C3RA42611D.

[48] S. Wiemers-Meyer, M. Winter and S. Nowak, Mechanistic insights into lithium-ion battery electrolyte degradation—a quantitative NMR study, Phys. Chem. Chem. Phys. 18 (2016) 26595–26601. https://doi.org/10.1039/C6CP05276B.

[49] M. Takehara, S. Watanabe, N. Nanbu, M. Ue and Y. Sasaki, Synthesis of fluorinated dimethyl carbonates by direct fluorination, Synth. Commun. 34 (2004) 1367–1375. https://doi.org/10.1081/SCC-120030685.

[50] C. L. Campion, W. Li and B. L. Lucht, Thermal decomposition of $LiPF_6$-based electrolytes for lithium-ion batteries, J. Electrochem. Soc. 152 (2005) A2327–A2334. https://doi.org/10.1149/1.2083267.

[51] L. Terborg, S. Weber, F. Blaske, S. Passerini, M. Winter, U. Karst and S. Nowak, Investigation of thermal aging and hydrolysis mechanisms in commercial lithium-ion battery electrolyte, J. Power Sources 242 (2013) 832–837. https://doi.org/10.1016/j.jpowsour.2013.05.125.

[52] Y.-F. Qiu, H. Murayama, C. Fujitomo, S. Kawai, A. Haruta, T. Hiasa, H. Mita, K. Motohashi and M. Tokunaga, Oxidative decomposition mechanism of ethylene carbonate on positive electrodes in lithium-ion batteries, Bull. Chem. Soc. Jpn. 96 (2023) 444–451. https://doi.org/10.1246/bcsj.20230027.

[53] H. Gunther, NMR Spectroscopy: Basic Principles, Concepts and Applications in Chemistry, 3rd ed., Wiley-VCH, Weinheim, 2013.

[54] R. L. B. Chen, F. N. Sayed, H. Banerjee, I. Temprano, J. Wan, A. J. Morris and C. P. Grey, Identification of the dual roles of Al_2O_3 coatings on NMC811 cathodes via theory and experiment, Energy Environ. Sci. 18 (2025) 1879–1900. https://doi.org/10.1039/D4EE03444A.

[55] S. Takabatake, N. Sagawa and T. Shikata, Quantitative antiparallel dimer formation analysis of ethylene carbonate in solution, Bull. Chem. Soc. Jpn. 89 (2016) 237–242. https://doi.org/10.1246/bcsj.20150346.

[56] N. Sagawa, S. Takabatake and T. Shikata, A dielectric spectroscopic study of ethylene carbonate in solution, Bull. Chem. Soc. Jpn. 89 (2016) 1018–1025. https://doi.org/10.1246/bcsj.20160126.

[57] H. Ota, Y. Sakata, Y. Otake, K. Shima, M. Ue and J.-I. Yamaki, Structural and functional analysis of surface film on Li anode in vinylene carbonate-containing electrolyte, J. Electrochem. Soc. 151 (2004) A1778–A1788. https://doi.org/10.1149/1.1798411.

[58] S. Schmidt, F. J. Gatti, M. Luitz, B. S. Ritter, B. Bruchmann and R. Mulhaupt, Erythritol dicarbonate as intermediate for solvent- and isocyanate-free tailoring of bio-based polyhydroxyurethane thermoplastics and thermoplastic elastomers, Macromolecules 50 (2017) 1604–1615. https://doi.org/10.1021/acs.macromol.6b02787.

[59] N. Gogoi, R. Lundstrom, G. Hernandez and E. J. Berg, Base-driven ring-opening reactions of vinylene carbonate, J. Electrochem. Soc. 171 (2024) 050506. https://doi.org/10.1149/1945-7111/ad430e.

[60] L. Xing, W. Li, C. Wang, F. Gu, M. Xu, C. Tan and J. Yi, Theoretical investigations on oxidative stability of solvents and oxidative decomposition mechanism of ethylene carbonate for lithium-ion battery use, J. Phys. Chem. B 113 (2009) 16596–16602. https://doi.org/10.1021/jp9074064.

[61] R. Kukeva, M. Kalapsazova, H. Rasheev, G. Vassilev, A. Tadjer and R. Stoyanova, In situ electron paramagnetic resonance monitoring of predegradation radical generation in a

lithium electrolyte, J. Phys. Chem. Lett. 14 (2023) 9633–9639. https://doi.org/10.1021/acs.jpclett.3c02374.

[62] V. N. Torocheshnikov and N. M. Sergeyev, ^{35}Cl and ^{37}Cl nuclear magnetic resonance of chloroorganic compounds, Chem. Phys. Lett. 288 (1998) 809–815. https://doi.org/10.1016/S0009-2614(98)00362-5.

[63] T. Li and P. B. Balbuena, Theoretical studies of lithium perchlorate in ethylene carbonate, propylene carbonate, and their mixtures, J. Electrochem. Soc. 145 (1999) 3613–3622. https://doi.org/10.1149/1.1392523.

[64] M. Hasegawa, H. Ishii, Y. Cao and T. Fuchigami, Regioselective anodic monofluorination of ethers, lactones, carbonates, and esters using ionic liquid fluoride salts, J. Electrochem. Soc. 153 (2006) D162–D166. https://doi.org/10.1149/1.2222891.

[65] F. A. Bovey, The high-resolution nuclear magnetic resonance spectroscopy of polymers, Prog. Polym. Sci. 3 (1963) 139–172.

[66] S. M. Blau, H. D. Patel, E. W. C. Spotte-Smith, X. Xie, S. Dwaraknath and K. A. Persson, A chemically consistent graph architecture for massive reaction networks applied to solid-electrolyte interphase formation, Chem. Sci. 12 (2021) 4931–4939. https://doi.org/10.1039/D0SC05647B.

[67] L. El Ouatani, R. Dedryvere, C. Siret, P. Biensan, S. Reynaud, P. Iratcabal and D. Gonbeau, The effect of vinylene carbonate additive on surface film formation on both electrodes in Li-ion batteries, J. Electrochem. Soc. 156 (2009) A103–A113. https://doi.org/10.1149/1.3029674.

[68] L. M. Thompson, W. Stone, A. Eldesoky, N. K. Smith, C. R. M. McFarlane, J. S. Kim, M. B. Johnson, R. Petibon and J. R. Dahn, Quantifying changes to the electrolyte and negative electrode in aged NMC532/graphite lithium-ion cells, J. Electrochem. Soc. 165 (2018) A2732–A2740. https://doi.org/10.1149/2.0721811jes.

[69] F. Neese, F. Wennmohs, U. Becker and C. Riplinger, The ORCA quantum chemistry program package, J. Chem. Phys. 152 (2020) 224108. https://doi.org/10.1063/5.0004608.

[70] N. B. Balabanov and K. A. Peterson, Systematically convergent basis sets for transition metals. I. All-electron correlation consistent basis sets for the 3d elements Sc–Zn, J. Chem. Phys. 123 (2005) 064107. https://doi.org/10.1063/1.1998907.

[71] F. Jensen, Segmented contracted basis sets optimized for nuclear magnetic shielding, J. Chem. Theory Comput. 11 (2015) 132–138. https://doi.org/10.1021/ct5009526.

[72] R. P. Seward and E. C. Vieira, The dielectric constants of ethylene carbonate and of solutions of ethylene carbonate in water, methanol, benzene and propylene carbonate, J. Phys. Chem. 62 (1958) 127–128. https://doi.org/10.1021/j150559a041.

[73] K. Momma and F. Izumi, VESTA 3 for three-dimensional visualization of crystal, volumetric and morphology data, J. Appl. Crystallogr. 44 (2011) 1272–1276. https://doi.org/10.1107/S0021889811038970.

Figure 1. a) Current measured on the disk and b) ring of the RRDE setup during oxidation of $LiClO_4$/DMC (purple), EC (blue), and EMC (pink), c) ratio of protons to electrons participating in the oxidation reaction across the three solvents at different voltage points obtained by dividing the currents in a) and b), d) Zoom of the ^1H NMR spectra tracking the evolution of electrogenerated protons in $LiPF_6$/DMC (top), /EC (middle), and /EMC (bottom) over storage time

Figure 2. Proposed electrochemical oxidation pathways of electrolytes with a) DMC, b) EC, and c) EMC

Figure 3: Oxidation and chemical degradation pathways of DMC.

Figure 4: Region between a) 4.50 and 6.50 ppm and b) 3.35 and 4.20 ppm of the ^1H NMR spectra, and c) ^{13}C NMR spectra of $LiClO_4$/DMC electrolyte at different time stamps. "Pristine" refers to the electrolyte prior to electrolysis, with "Oxidized Day 1" occurring roughly 20 minutes after electrolysis was stopped. The color coding follows the same assignment as Figure 3: the reaction intermediates are highlighted in yellow, the major oxidation product in green and the products of chemical cascades in purple. The zoom to the right of panel a) shows a close look at the increase in intensity of the major product.

Figure 5: a) ^1H shifts of oxidized $LiPF_6$/DMC electrolyte at different time points after initial electrochemical oxidation was stopped from 4.50-6.50 ppm. The reaction intermediate peak is highlighted in yellow at 6.45 ppm. The major oxidation product at 4.64 ppm is highlighted in green and its intensity increase upon aging is expanded upon on the right. b) ^1H and ^{13}C correlation 2D NMR (HSQC (left) and HMBC (right)) of FDMDOHC and other oxidation products, inset of labeled FDMDOHC structure. c) ^1H shifts of oxidized $LiPF_6$/DMC electrolyte at different time points after initial electrochemical oxidation has stopped from 3.55-4.82 ppm, d) ^{19}F shifts of FMMC and BF_4^- in oxidized $LiPF_6$/DMC

Figure 6: Oxidation and chemical degradation pathways of EC

Figure 7: ^1H shifts of oxidized EC electrolyte with $LiClO_4$ (top) or $LiPF_6$ (bottom) at different time points after initial electrochemical oxidation has stopped. The reaction intermediates are highlighted in yellow. The major oxidation product, VC, is highlighted in green and expanded upon on the left.

Figure 8: ^1H shifts of oxidized $LiPF_6$/EMC electrolyte at different time points after initial electrochemical oxidation has stopped. Intermediates are highlighted in yellow and the major

oxidation product at 4.97 ppm and 1.67 ppm is highlighted in green. Its intensity increase upon aging is expanded upon below.

Abstract

Raising the upper cutoff voltage of lithium-ion batteries (LIBs) to increase energy density often exceeds the electrolyte's anodic stability limit, accelerating degradation and creating a major durability tradeoff. Designing electrolytes that can sustain long-term high-voltage cycling requires a clearer understanding of the fundamental mechanisms occurring when commercial carbonate solvents oxidize. To this end, simplified single-salt, single-solvent formulations of $LiClO_4$ and $LiPF_6$ in dimethyl carbonate (DMC), ethylene carbonate (EC), or ethyl methyl carbonate (EMC) were anodically electrolyzed on inert electrodes and monitored for extended periods of time using ^{1}H, ^{13}C, ^{19}F, and ^{35}Cl nuclear magnetic resonance (NMR) spectroscopy. The controlled environment of the experiments, coupled to the unique sensitivity of NMR, unveiled novel metastable intermediates and the formation of branching networks of products with temporal evolution. Oxidation of the pristine solvent primarily proceeds through a radical pathway that also produces highly reactive protons but faces competition from a second pathway involving a radical carbocation intermediate. In all cases, the intermediates follow a variety of downstream pathways that can intersect with each other. The concomitant network of reactions represents a significant increase in complexity compared to common descriptions in the literature, yet, critically, it helps explain the wide range of products typically identified in electrolyte oxidation in complete cells. The results highlight the need for refocusing fundamental research on anodic stability to analysis of the hierarchy of reaction networks to better inform efforts to mitigate the detrimental effects on battery performance, including prevention and harvesting of proton and radical products.

1.

Introduction

There is a widespread push towards improving the energy density of lithium-ion batteries through the use of cathodes operating at a high voltage such as $LiNi_{0.8}Mn_{0.1}Co_{0.1}O_2$ (NMC811) and $LiNi_{0.5}Mn_{1.5}O_4$ (LNMO) [1,2]. However, cycling to the higher voltages enabled by these cathodes often leads to rapid capacity loss and eventual cell failure [3]. These challenges can be attributed to a variety of failure mechanisms associated with processes at the cathode surface and in the electrolyte [4-7]. Unlike the SEI at the anode, the subsequent formation of cathode electrolyte interphases (CEI) is insufficient to induce electronic passivation, so the electrolyte continues to reach the electrode surface and undergoes oxidation upon cycling. Oxidation of the electrolyte contributes directly to these failure mechanisms via detrimental gas formation, generation of aggressive acidic species, and loss of ionic transport at the interface due to solvent depletion [8,9]. However, the exact hierarchy of the electrochemical and chemical reactions that build the pathways of oxidation of Li-ion battery electrolytes is only partly understood. This lack of understanding has resulted in highly empirical approaches to electrolyte design that, so far, have been unable to produce a breakthrough solution to mitigate degradation while enabling high-voltage, high-energy devices.

Degradation studies of the leading carbonate-based electrolytes have become widespread over the years, spanning experiments [7,10-13] and computations [14-16]. To date, it has been proposed that oxidation-induced breakdown of components of the electrolyte can proceed through C-H bond scission on the highly charged cathode surface [10,11,14,17], reaction with oxygen and peroxide species released during cathode phase changes [7,18-20], and interactions with radical and charged species in the electrolyte [21-23]. Yet there is still a significant lack of consensus on the inherent stability of the electrolytes at high potential, and, particularly, the relationship between the fundamental mechanism by which they can oxidize and the products of degradation observed. This outcome is not surprising when considering the chemical variability of possible solvents. In particular, the choice of salt in the oxidation study has been shown to affect the products of anodic decomposition, and studies evaluating degradation often use full cells designed for performance evaluation, which are heavily influenced by improper control of impurities, such as water, or contamination from the many components present [24-28].

The predominance of analyses of specific blends of solvents and salt makes it challenging to isolate the reactivity of each component and identify the largest culprits of degradation. As a consequence, linear carbonates like dimethyl carbonate (DMC) and ethyl methyl carbonate (EMC) are often assumed to be stable up to 5.0 V because cyclic carbonates like ethylene carbonate (EC) [29] tend to dominate behaviour in blends. A small number of reports indicate that DMC can degrade into formic acid, lithium methyl carbonate, CO_2, and organic polycarbonates [7,23,30], while EMC undergoes transesterification in the presence of lithium alkoxides to form DMC and DEC which can then further react to form additional dialkyl carbonates [31]. However, a more complete

analysis of the chemical decomposition of the linear carbonates in isolation is still necessary to understand each individual mechanism contributing to electrolyte degradation during high voltages.

Despite the comparably much greater effort on understanding the decomposition behaviour of EC, there is still no unified theory relating all of its products to specific pathways [29]. The leading mechanism in the literature involves ring-opening reactions to form glycolic acid, CO_2, oxalic acid, and long-chain oligomeric PEO-like species, although typically aided by the presence of some form of O-containing species (either as a transition metal oxide in the cathode or reactive oxygen species released during cathode phase changes) [7,19,21,32,33]. A second, less examined possibility involves EC undergoing double deprotonation to form vinylene carbonate (VC) [10,11,19] or even polymerizing to form poly-EC [13], rather than ring opening. The steps by which two hydrogen atoms can be removed simultaneously have not yet been revealed. Freiberg et al. proposed a reaction with singlet oxygen to abstract two protons and release an H_2O_2 molecule [19] whereas Zhang et al. theorized a two-step deprotonation involving a charged NMC811 surface with in-situ FTIR measurements [10]. Both paths rely on the presence of an oxide in the cell, yet previous work by our group has demonstrated the formation of VC from electrooxidized EC alone on oxide-free, inert Pt surfaces [34]. The only known mechanism that could generate VC without involvement of oxygenated species is a proposal by Shkrob et al. where they theorized that radiolysis can induce the disproportionation of two EC-generated radicals [21]. Therefore, a more in-depth tracking of the actual steps that follow EC oxidation remains necessary to understand the fundamentals of these reactions.

Electrolyte decomposition mechanisms have been analyzed with a wide variety of techniques including infrared/Raman spectroscopy [23], online electrochemical mass spectrometry (OEMS) [8], electron paramagnetic resonance (EPR) [21], and nuclear magnetic resonance (NMR) spectroscopy [7]. NMR, in particular, provides unique insight into bonding, electronegativity, and functional groups of unknown compounds, allowing for new structures and soluble decomposition products to be theorized. However, NMR shifts and identifications are highly influenced by the solvation environment and contaminants. Even the addition of deuterium-labelled solvents into the electrolyte for referencing can cause unforeseen reactions with impurities (e.g. H_2O in DMSO-d_6), leading to misleading products [35]. Therefore, careful precautions must be taken to ensure the act of measuring the sample does not influence the results. Furthermore, to minimize the complexity of the observed reactions and allow the direct measurement of specific solvent degradation mechanisms, model electrolytes on inert electrodes must be utilized. While NMR studies on inert electrodes have been performed in the past, only a handful of products were identified, resulting in an incomplete understanding of the reactions possible even in these simpler systems [23,30].

In this work, we targeted the intrinsic anodic chemistry of the most common solvents in LIBs. Model electrolytes composed of a single salt ($LiPF_6$ or $LiClO_4$) and solvent (DMC, EMC, or EC) were oxidized on an inert single crystal Pt (111) surface before being analysed with a combination of ^{1}H, ^{13}C, ^{19}F, and ^{35}Cl NMR for dynamic tracking of species, utilizing multi-compartment, flame-

sealed glass capillaries to avoid reactions between the oxidized electrolyte and the deuterium-labelled solvent. By decreasing the potential reactants to just one salt and one solvent, direct mechanistic tracing from products to oxidized intermediates became possible. The results reveal that even these simple systems undergo a network of reactions that can compete with each other. We describe their hierarchy, isolate the main paths of electrochemical versus chemical degradation, as well as label the structures of four intermediate species and four products that were previously unidentified. By identifying key moments in electrolyte solvent oxidation and chemical degradation mechanisms that lead to the most damage in the eventual cell, more effective mitigation techniques can be applied, eventually unlocking increasing voltages in Li-ion batteries.

2. Results

Solutions of 1.3 M $LiClO_4$ or $LiPF_6$ in DMC, EC, or EMC were oxidized on either a RDE or RRDE under constant Ar flow. Electrochemical oxidation has often been reported to begin with a proton abstraction reaction [16,36]. The use of the RRDE enabled the comparison of the current density detected at the disk (Figure 1a) from solvent oxidation directly to the current measured at the ring (Figure 1b) when set at a potential to induce proton reduction to determine the proportion of electrons to protons generated in each of the three solvents (Figure 1c). RRDE has been previously discussed as a tool for investigating the electrooxidation of solvents by Hatsukade et al [37]. The formation of protons in all three solvents was further confirmed via ^1H NMR spectroscopy ($LiPF_6$: Figure 1d, $LiClO_4$: Figures S1-3) [34]. These highly deshielded protons appear further downfield than many reported superacids [7,38], suggesting a very aggressive chemical nature. They varied in chemical shift from 18.51 ppm for EC to 17.91 ppm and 15.00 ppm for DMC and EMC, respectively. The higher acidity in EC can be attributed to the delocalization of the remaining electron across the cyclic structure after proton removal, making the conjugate-base EC more stable and leading to increased acidity [39,40]. Upon storage, the reactive acidic proton signal shifted upfield and changed linewidth, indicating a change in its chemical environment, but, for the first week, the integrated intensity remained steady, indicating that there was no significant decrease in proton concentration during the earlier stages. Although the results presented here were performed in borosilicate glass tubes, reactive proton generation with similar trends were observed in PTFE NMR tubes containing oxidized $LiClO_4$/EC (Figure S4). In order to achieve the concentrations of species necessary to observe products in NMR, the RRDE was run for long periods, leading to the high potentials observed in Figure 1a-b; however, protons have been previously reported to form at potentials typical of standard battery cycling (~4.0V vs. Li/Li^+) [37].

In previous work, we found that protons generated from solvent oxidation can proceed to catalytically convert EC into CO_2 and various ether products through a ring-opening mechanism in a chemical decomposition process without an applied potential [34]. However, this proton-promoted cascade does not fully account for the myriad of other products, like VC and FEC, often observed at these high potentials [10,19]. RRDE data (Figure 1c) measured at a range of voltages

indicates that the electrochemical oxidation occurs with a proton-to-electron ratio of roughly 1:2 [37]. Given the calculated ratio, three initial electrochemical oxidation pathways have been proposed for each solvent (Figure 2) based on the most logical locations on the molecule that protons and electrons would be lost. Path A would generate a radical carbocation through the loss of a single electron (e.g. $EC^{\bullet+}$). Path B would involve the loss of a proton and an electron resulting in a neutral radical molecule (e.g. $EC^{\bullet}$). In order to achieve the observed 1:2 ratio, a combination of path A and path B would need to occur simultaneously. Path C would combine path A and path B into a single process, removing two electrons and a proton, leaving a carbocation (e.g. EC^{+}). All the proposed intermediates are expected to be highly reactive and unstable, especially the primary radicals or carbocations that would form from DMC (Figure 2a), compared to the possible ring-stabilization of EC intermediates (Figure 2b), or the secondary species in EMC (Figure 2c). Species associated with Path B have previously been proposed upon oxidation of EMC and EC on NMC811 oxide surfaces [10], but these radicals seem to be too short-lived to be observed without additional stabilization in this oxygen-free environment with no surface anchorage possible. EPR data was collected for electrolyzed EMC and EC (DMC was not measured due to the instability of the proposed primary radicals in these samples) only a few minutes after stopping the electrochemical cell, but no stable EPR-active radical species were observed. The lack of a major EPR signal (Figure S5) or any shortening in NMR relaxation times in ^{1}H NMR does not eliminate the possibility of the electrochemical paths proposed in Figure 2. Instead, it simply indicates either the concentrations of radicals were too low (in proportion to the bulk solvent) to be detected via EPR and/or the proposed free radical species are highly driven towards stable products and/or radical-free metastable intermediates, which have much longer lifetimes and can be measured via NMR. Addition of any radical trapping species for EPR measurements would more likely result in the degradation of the trap, leading to additional complications in interpreting the underlying mechanism.

The wide variety of decomposition products observed by tracking the evolution of electrolyzed solutions by ^{1}H and ^{13}C NMR 1D/2D NMR nonetheless presented commonalities in structure that enabled backtracking to common ancestors (Paths A-C) to determine a full mechanistic understanding of solvent degradation from initial oxidation onwards. The highly branched and interconnected mechanism derived from these results is contrary to the linear reaction pathways often discussed in the literature. ^{35}Cl and ^{19}F were performed to gather additional information on the influence of salt in product formation. To better understand the complex reactions occurring within each solvent, their specific mechanism of degradation is presented first, using detailed NMR spectra and reasoning based on established chemical principles, followed by a summary of the key lessons of this work. Due to the similarities in symmetry, simplicity, and overall outcomes, decomposition pathways for DMC and EC are discussed first, followed by EMC, which presented additional complexity due to its asymmetry. Our discussion decouples the main products after oxidation from those that form during subsequent chemical cascades over extended periods of time (~1 week of storage). Furthermore, the addition of water as an impurity obscures many of the

results reported below indicating how some of these products can often be masked in more complex systems.

2.1

DMC

Of the three solvents examined, dimethyl carbonate was the simplest, leading to a series of relatively straightforward decomposition peaks in the NMR spectra. The overall mechanism from DMC with $LiClO_4$ or $LiPF_6$ to products is presented in Figure 3. A tally of NMR peaks with an assignment of species, leading to Figure 3 from the data in Figure 4, is summarized in Table S1. Figure 4a presents the ^{1}H NMR data in a way that highlights the early species, with Figure 4b tracking the species from downstream processes. Figure 4c presents the evolution of the ^{13}C NMR for the same samples. From these results, it is clear that DMC$^{\bullet}$ (Path B) is the key intersection from which many of the subsequent products are formed while DMC$^{\bullet+}$ (Path A) mainly serves to form minor and small molecule products.

Based on ^{1}H peak integrations (Figure S6), the major oxidation product of $LiClO_4$/DMC is associated with a singlet at 4.62 ppm, which grows over time. Careful investigation of the ^{13}C spectra showed that peaks at 62.4 ppm and 154.8 ppm grow concurrently (Figure 4c). These peaks are consistent with methylene groups directly attached to O in a symmetric molecule like dimethyl-2,5-dioxahexanedioate (DMDOHC). DMDOHC was first proposed as a product of DMC oxidation by Moshkovich et al., with the same peaks at 4.62 ppm for ^{1}H and 62.4 ppm for ^{13}C [23]. Most current reports of DMDOHC generation came from studies of electrolyte formulations containing EC and $LiPF_6$ along with DMC and, therefore, attribute its formation exclusively to EC ring-opening [31,41,42]. Alternatively, this product could form from two DMC$^{\bullet}$ molecules reacting with each other at the terminal radical. In theory, an additional methyl ^{1}H signal should be observed around 4.01 ppm for DMDOHC, but it was likely masked by the DMC signal due to its low concentration. Indeed, no new ^{1}H signals were observed after purposefully adding small amounts of DMDOHC (~0.5 wt%) to pristine $LiPF_6$/DMC, without any obvious asymmetry of the DMC peak (Figure S7). Furthermore, DMDOHC can decompose into a mixture of EC and DMC in the presence of a lithium alkoxide [31,41,43]. While alkoxides were not initially observed in the oxidized electrolytes, continued chemical degradation reactions, possibly combined with slow oxygen leakage through the Teflon taping, led to the appearance of $LiOCH_3$ (^{1}H: 3.57 ppm, Figure 4b) after roughly a week of aging, unlocking this pathway [7]. The growth of a new singlet peak at 4.78 ppm (Figure 4a) about a week after the initial oxidation provides evidence of the generation of EC in the final solution, which was further affirmed by standard additions to pristine $LiPF_6$/DMC electrolytes (Figure S8). DMDOHC and EC signals continuously increased over the NMR observation period. Given their origin on Path B, this trend indicates that generation of DMC$^{\bullet}$ must be occurring even after oxidation has stopped. The continuous increase in DMC$^{\bullet}$ was previously observed by EPR in a study where it was proposed to form as a secondary product from the reaction of DMC with a methyl or formyl radical from a different reaction [21].

The presence of the ^{1}H singlet at 6.45 ppm for a full day before disappearing indicates a metastable species that is eventually consumed and/or converted. When examining the ^{13}C spectra (Figure 4c), peaks at 91.2 ppm and 153.9 ppm disappeared around the same time. Together, these shifts indicate a -CH_2- functionality with two highly electronegative components adjacent on each side. Carbonate units meet this criterion, suggesting a molecule like the DMC A+B carbocation in Figure 3. DFT calculations of this A+B intermediate (Figure S9) predicted ^{1}H peaks at 6.49 ppm (^{13}C: 88.6 ppm) for the protons in the -CH_2- functionality between carbonate units, and 4.29 ppm and 4.84 ppm for the outer -CH_3 groups, in reasonable agreement with weak signals at 4.15 ppm and 4.76 ppm (Figure S10). These three peaks showed similar temporal dynamics upon storage, further supporting the assignment. Consequently, the formation of both initial intermediates in Path A and B is possible simultaneously upon oxidation. Both $DMC^{\bullet+}$ and $DMC^{\bullet}$ (Figure 2a) are too unstable in their original radical forms to be measured by NMR, especially as a paramagnetic organic species without a clear metal centre associated with them [44]. However, it is entirely plausible that they could form the metastable A+B species, thus eliminating the radicals and allowing detection via NMR. Although more stable than $DMC^{\bullet+}$ and $DMC^{\bullet}$, A+B is still a carbocation, albeit ternary, that will eventually break back apart into its constituent $DMC^{\bullet+}$ and $DMC^{\bullet}$ molecules to follow the respective product networks. An alternative structure of A+B could be theorized where the radical $O^{\bullet}$ of $DMC^{\bullet+}$ abstracts a proton from the terminal carbon of a pristine DMC molecule to generate more $DMC^{\bullet}$ [14,21]. However, this pathway seems less likely, as a protonated version of $DMC^{\bullet+}$ was not observed in these measurements.

Minor products of oxidation and associated chemical cascades were observed as the solution continued to degrade during storage. Very small amounts of HCOOH (Figure S11) were detected at 8.35 ppm (^{1}H, s) from the early stages, but without significant concentration changes after day 2 [7,45]. The only other minor product formed just after the initial oxidation step was observed at 5.97 ppm (^{1}H, s, Figure 4a) and grew in intensity until about one day after oxidation before levelling off. It is assigned as dimethyl methylene bis(carbonate) (DMMBC), first hypothesized by Moshkovich et al. [23] to arise from the reaction $DMC^{\bullet}$ with a radical methyl carbonate from the abstraction of CH_3^{+} from $DMC^{\bullet+}$. DMMBC forms independent of the salt; however, further validation of this mechanism can be seen when the salt in the electrolyte is switched from $LiClO_4$ to $LiPF_6$ (discussed in more detail below), as the reaction of CH_3^{+} with F generates fluoromethane in the ^{19}F spectra at -269.7 ppm (q, $^{2}J_{FH}$=46.2 Hz, Figure S12) [46,47]. As the solution continued to react over storage time, other products were generated from the continued chemical degradation of solvent molecules in the oxidized electrolyte. Besides $LiOCH_3$, lithium methyl carbonate (^{1}H singlet at 3.54 ppm in Figure 4b) was ascribed to unavoidable leaks of air into the NMR tube over time [7,43]. Finally, CO_2 was observed in the ^{13}C spectra (125.1 ppm, Figure 4c) 15 hours after oxidation, which has been widely reported as a downstream reaction product along with formic acid after DMC oxidation [7,17,23].

To determine the influence of salt on solvent-derived degradation products, $LiPF_6$/DMC was also studied. The main outcomes were very similar to $LiClO_4$/DMC (Table S1), so we focus here on

the key differences. The major ^{1}H peaks of interest are tracked over storage time in Figure 5a-d, with peak integrations (relative to the DMC solvent peaks) plotted in Figure S13. The reactive proton generated by oxidation of $LiPF_6$/DMC appears at a higher field (17.91 ppm, Figure 1d) than in $LiClO_4$/DMC (Figure S1), suggesting a greater acidity [48]. The A+B carbocation peak at 6.45 ppm displayed seemingly accelerated dynamics, as its concentration peaks sooner than in $LiClO_4$/DMC, lasting less than 7 h. This observation hints at an increasing decomposition rate catalysed by the PF_6^- anion that increases the charge density on the carbonate moiety of A+B. This leads to more nucleophilic attacks, and thus, higher concentrations of the main decomposition product at 4.64 ppm [41].

The presence of fluorine in the electrolyte mixture also introduces new products. Present from the initial stages after oxidation, fluoromethyl methyl carbonate (FMMC) was assigned to signals at 5.94 ppm (d, $^{2}J_{HF}$ = 51.0 Hz, Figure 5a) and -157.6 ppm (t, $^{2}J_{FH}$= 51.0 Hz) (Figure 5d) in the ^{1}H and ^{19}F NMR, respectively, with correlated HSQC and HMBC ^{13}C 2D data (Figure S14). The methyl moiety of FMMC appeared as a small singlet peak around 4.01 ppm (Figure S15), in accordance with its proximity to DMC at 4.00 ppm. This product results from the fluorination of $DMC^{\bullet}$ [49]. A fluorinated version of DMDOHC (FDMDOHC, Figure 3) was assigned to the major ^{1}H peak at 4.64 ppm (s), only slightly shifted from the F-free product in $LiClO_4$/DMC, correlated to ^{13}C peaks at 63.0 and 162.9 ppm (Figure 5b). The addition of F to the terminal C should be enough to slightly deshield the inner $-CH_2-$ to cause the subtle shift. DFT simulations (Figure S16) placed them in the range of 4.38 ppm (similar to the 4.39 ppm predicted for the inner $-CH_2-$ in DMDOHC), with the terminal H adjacent to F theoretically overlapping with the FMMC peaks at 5.92 ppm. This molecule could form from linking together two subsequently deprotonated FMMC molecules or by subsequent fluorination of DMDOHC from linking two $DMC^{\bullet}$.

A closer look at the ^{1}H (Figure 5c) and ^{19}F spectra (Figure S17) also revealed products of decomposition of the salt over the observation period. The major fluorophosphate formed was $OPF_2(OCH_3)$, at -88.5 ppm in ^{19}F (d, J=1005.7 Hz) and 4.44 ppm in ^{1}H (d, J=12.1 Hz)). Wilken *et al*. predicted this product from the reaction of DMC with POF_3, also observed at -90.1 ppm (^{19}F, d, J=1066.1 Hz), itself arising from exposure of PF_5^- with trace H_2O [47]. Very small ^{19}F signals were also observed for $OPF_2(OH)$ at -84.9 ppm (d, J=975.5 Hz) and $OPF(OCH_3)_2$ at -88.3 ppm (d, J=961.0 Hz) [9,47,50]. While HF would be expected to form from PF_6^-, there were no detectable peaks in the 9.14-10.60 ppm ^{1}H range where a doublet would be expected [7,48]. In addition, there was only a faint, broad singlet around -191.4 ppm in the ^{19}F spectrum (Figure S18) indicating that if HF is formed, it is at very low concentrations and/or consumed. In contrast, a ^{19}F signal at -156.1 ppm (s) (Figure 5d) arose upon extended storage, indicating the formation of BF_4^- from etching of the borosilicate glass tubes by the acidic solution, likely coming from the $OPF_2(OH)$ and highly acidic proton (Figure 1d) [48].

2.2

EC

Moving from a linear symmetric molecule like DMC to a cyclic symmetric molecule like EC significantly increases the complexity of the chemical cascade products, as the ring can stabilize reactive intermediates or open to form a mixture of linear and cyclic products. However, despite the differences in products, DMC and EC have very similar initial mechanisms indicating the importance of symmetry in these early reactions. The full EC reaction mechanism is presented in Figure 6, and Table S2 summarizes all the ^{1}H NMR peaks observed and discussed below.

The ^{1}H NMR spectra of the oxidation products of both $LiClO_4$ and $LiPF_6$ in EC are displayed in Figure 7 with the overlay spectra for the major peak at 7.35 ppm expanded on the left. In fact, outside of direct anion reactions with reactive EC intermediates, almost all the reported oxidation products were observed in both $LiClO_4$ and $LiPF_6$-containing electrolytes. The only major difference was the faster growth of the main reaction products, particularly VC, in oxidized $LiPF_6$/EC (Figure S19), similar to the case of oxidized DMC [51]. Similar $LiPF_6$ hydrolysis steps were observed as in DMC with still little to no evidence of HF formation (Figure S20).

The products of EC oxidation can be sorted into two categories, ring-opened and cyclic molecules, which correspond to paths that start with one electron transfer (Path A) and one electron/proton transfer (Path B), respectively. Overall, the major oxidation product of EC is VC, which requires the net removal of two electrons and two protons. It corresponds to a ^{1}H signal at 7.35 ppm(s) and ^{13}C peaks at 134.1 ppm (HSQC) and 156.1 ppm (HMBC) (Figure S21). Its formation was further confirmed via addition of 100 mM VC into the oxidized electrolyte, resulting in an increased intensity at 7.35 ppm (Figure S22). In the literature, EC has been reported to oxidize to form VC and CO_2 separately, but with much debate over the exact mechanism [10,15,19,52]. Typically, the removal of the second proton is explained via reaction with oxygen species (singlet, peroxide, superoxide) originating from the cathode material [10,12,18,19,33]. However, such a mechanism is not possible on inert Pt electrodes used here. Instead, one of the theorized radical intermediates (Figure 2b), likely EC$^{\bullet}$, could perform a secondary radical reaction on either another EC$^{\bullet}$ or EC itself, resulting in additional proton abstractions and the formation of the alkene bond in the ring. The continuous increase in VC concentration over storage time thus implies that additional radical species must be either formed or made available for further reactions, even after electrochemical oxidation has stopped.

The continued availability of EC$^{\bullet}$ could also arise from the dynamics of an EC A+B metastable species analogous to that described for DMC. DFT predicts ^{1}H NMR shifts for the neutral ring portion of a plausible A+B intermediate at around 6.81 ppm (dd, according to traditional splitting patterns) [53] with adjacent ^{1}H at 4.92 ppm and 4.94 ppm, as well as ^{13}C peaks of 70.4 ppm, 105.7 ppm, and 153.5 ppm (Figure S23). These predictions match the ^{1}H peak at 6.59 ppm (dd, J=5.5, 1.9 Hz) with correlated peaks at 4.78 ppm and 4.95 ppm from the adjacent H in the ring structure (Figure S24) and ^{13}C shifts of 71.6 ppm, 96.8 ppm, and 156.0 ppm (Figure S25-26). The original ^{1}H peaks on the carbocation ring portion of the A+B species are predicted at 5.44 ppm, in a region

where they could be masked by large noise around the EC solvent peak (Figure 7). In addition to the noise, carbocation predictions are challenging as simulations cannot perfectly reflect the complicated solution dynamics occurring in the electrolyte including the influence of salts and other ions on the conformation and positioning of the molecule, perhaps explaining the slight difference between experimental and estimated shift in the ^{13}C peak at 96.8 ppm. Still, this structure seems reasonable as Chen et al. have assigned a similar peak (6.62 ppm (dd, $^{3}J_{H-H}$= 5.6, 1.9 Hz)) to methoxyethylene carbonate (MEC), a molecule with a very similar structure [54].

Regardless of electrolyte salt, a short-lived intermediate appeared at 5.34 ppm (s) that is correlated with ^{13}C NMR peaks of 76.5 ppm (HSQC) and 169.6 ppm (HMBC) (Figures S26-27). Based on the mechanism of VC formation from EC through a double radical along Path B, this peak could be a dimerized form of EC, $(EC)_2$, from two double radical intermediates, branching away from VC formation. DFT simulation of this molecule estimates a ^{1}H chemical shift of 5.16 ppm (s) and ^{13}C peaks at 77.4 ppm and 164.5 ppm (Figure S28). Anti-parallel EC dimers have previously been observed in both solution and gas-phases using dielectric and infrared spectroscopy, respectively, and are highly dependent on surrounding solvent dynamics to determine the degree of dimerization [55,56]. Since the only solvent here is EC, it is likely stabilized enough by the other EC molecules to be observed via NMR, whether that is with actual bonding or a quasi-shared radical species between the two charged molecules. Still, the predicted molecule would experience significant amounts of ring strain, especially in the quasi-butane ring connecting the two molecules, making it highly unstable. Conversely, VC is highly stable and can be generated from the same initial diradical components. Therefore, any generated $(EC)_2$ likely breaks apart somewhat quickly to still form more VC molecules over time.

Cyclic intermediates and even minor products along Path B seemed to converge toward VC. Polymerized forms are also expected based on literature observations, but only a dimerized form of EC, [4,4'-bi(1,3-dioxolane)]-2,2'-dione (BDOD), generated from two $EC^{\bullet}$ molecules attaching at the radical position was detected after a day of storage with ^{1}H peaks around 5.37 ppm (m, J=12.1 Hz) (Figure S29) and widths similar to the literature [57,58]. Once VC has formed, it can also further react with a double addition of $EC^{\bullet+}$ across the alkene bond to form a VC+2A structure (Figures 7, S22, S30), which is ascribed to the ^{1}H signals at 6.63ppm (s) with correlated ^{13}C peaks of 98.7 ppm and 152.2 ppm (Figure S27, S31), and would offer a plausible path to polymerization. A similar branching mechanism of VC polymerization was reported by Ota et al [57].

As a radical carbocation molecule, $EC^{\bullet+}$ is predicted to favor ring opening [23]. Based on peak integrations, the ring-opened products were much more prevalent in $LiClO_4$/EC than $LiPF_6$/EC. Once opened, these molecules can undergo any number of chemical reactions, fracturing and rejoining to form new species, creating new branches of the network. Based on the shift and splitting patterns, the products at 6.08 ppm (dt, J=5.5, 2.5 Hz) and 5.83 ppm (dd, J=5.5, 2.5 Hz) are examples of polymeric species that can be generated as a result. The former can be ascribed to a proton with two H on one adjacent C (likely on the end of a double bond) and one H on the other adjacent C while still containing a carbonate group (Figures S24-27). The result could have a

similar structure to but-3-en-2-yl carbonate, although confirmation requires further study. The peak at 5.83 ppm is consistent with poly(1-hydroxyethyl carbonate) (PHEC) where an $OH^{\bullet}$ group (either from trace H_2O or from other molecule fragments) reacts on the ring-opened EC molecule to form a hydroxylated polymeric chain similar to previous reports (Figures S24-25, S31) [57,59]. Smaller molecules formed during the first NMR measurements as a result of fragmentation, including glyoxal at 9.34 ppm (s) (Figure S32) [23,60,61], CO_2, and various ether molecules at 3.72 ppm and 3.66 ppm (s) (Figure S29). CO_2 and ethers like oxirane, 1,4-dioxane, and 2-methyl-1,3-dioxolane were previously reported to form as a result of chemical (as opposed to electrochemical) decomposition of intact EC molecules, catalysed by the protons generated by the anodic process [34]. The sharp intensity increase in the 3.72 ppm and 3.66 ppm peaks after a week of storage corresponds to the generation of Li_2CO_3 and $LiOCH_3$ due to slow oxygen leakage through the Teflon tape, as discussed for DMC. EC can react with $LiOCH_3$ to form DMDOHC (or its fluorinated counterpart, FDMDOHC), which could explain the appearance of a small ^1H peak at 4.66 ppm (Figure S29).

We observed products related to the reaction of the specific electrolyte salt with $EC^{\bullet}$ after the initial oxidation. In the oxidized $LiClO_4$/EC electrolyte, a ^1H signal at 6.94 ppm (dd, J=6.0, 1.7Hz), correlated with other H at 4.90 ppm and 4.99 ppm (Figure S24) and ^{13}C at 102.6 ppm (Figure S27), was hypothesized to arise from Cl-based substitution into EC. DFT calculations for shifts of potential candidates led to (ClO_4)EC, which would produce a ^1H peak at 6.79 ppm and a correlated ^{13}C peak at 99.9 ppm (Figure S33). Due to the rapid relaxation of the ^{35}Cl nuclei, concurrent ^{35}Cl NMR (Figure S34) only showed a single broad peak, related to the coordination of the $LiClO_4$ salt with solvent molecules, that did not change over storage time [62]. However, the broad nature of this peak does not necessarily distinguish between coordinated ClO_4^- to EC and the unstable bond forming (ClO_4)EC from the anion and $EC^{\bullet}$. The bulky substituent and the poor solvation of ClO_4^- with EC [28,63] likely render the molecule highly unstable, consistent with its prominence only in the first scan and its complete disappearance after two days of storage. In contrast, $LiPF_6$ unlocked a path to the clear and sustained presence of fluorinated ethylene carbonate (FEC), with ^1H peaks at 6.42 ppm (ddd, J=64.1, 4.3, 1.1 Hz) and ^{19}F peaks centered at -124.0 ppm (dq, J=64.1 Hz) (Figure S34) [7,54].

Due to the high reactivity of the intermediates in the oxidized electrolyte, the slightest amount of contamination either from air or H_2O will steer the observations artificially away from the specific products resulting from oxidizing the electrolyte. These impurities can come from the purity of electrolyte solvents, the efficacy in sealing the samples, and, most insidiously, even the use of common deuterated NMR standards. Our experimental design avoided these issues by engineering a sample holder that allowed us to seal sample and deuterated standard free from air in separate chambers to prevent cross contamination. To highlight the importance of this design, we conducted experiments where we intentionally added 1 wt% H_2O to $LiClO_4$/EC immediately after oxidation had ceased and conducted similar ^1H NMR analyses (Figure S36). First, the highly deshielded proton signals were absent, replaced by a broad peak around 9.10ppm, which would be consistent

with a carboxylic acid instead of a highly acidic species. Second, while VC and other species were still formed, they did so at smaller concentrations in the presence of H_2O. Third, the EC A+B peak at 6.59 ppm changed shape slightly and disappeared quickly and some of the more unstable intermediates, like $(ClO_4)EC$ and $(EC)_2$, were not observed at all. Instead, the presence of H_2O induced the formation of PHEC, at 5.83 ppm, which could result from hydroxyl groups reacting with a ring-opened molecule. Overall, these observations do not necessarily mean the initial intermediates are not formed, but they were certainly masked and/or altered by other reactions in the solution, ultimately fundamentally modifying the observed pathways, distorting observations enough to potentially lead to incomplete conclusions.

2.3

EMC

The ^1H NMR spectra for oxidized $LiPF_6$/EMC are presented below in Figure 8 with the corresponding ^1H data for oxidized $LiClO_4$/EMC in Figure S37 and integrations in Figure S38. The summary of ^1H and ^{13}C data is displayed in Table S3. The change from a symmetric molecule like DMC and EC to an asymmetric molecule like EMC, increased the possible mechanism permutations because more than one type of H is available for extraction. Previous theoretical work has predicted the preferential deprotonation at the b-site in the ethyl group [10,64]. The products themselves, however, reflect the asymmetry of the molecule and include a mixture of products associated with excision of either $-CH_3$ group, similar to DMC oxidation, or $-CH_2-CH_3$ group of EMC. Out of all the solvents examined, EMC appeared to have the highest concentration of HF observable via NMR at -191.1 ppm (^{19}F, Figure S39) with increased BF_4^- glass etching and more fluorophosphate degradation species (Figure S40).

The major product in both $LiClO_4$ and $LiPF_6$/EMC appeared in the ^1H spectrum at 4.96 ppm (^{13}C peak at 75.1 ppm) and 1.70 ppm (^{13}C peak at 12.7 ppm) (Figure S41). In $LiClO_4$/EMC, these signals appeared as a clear quartet (^2J=7.2 Hz) and triplet (^2J= 7.0 Hz), respectively, indicative of a $R-O-CH_2-CH_3$ overall structure (Figure S37, S41); with smaller overlapping peaks growing in over storage time. With $LiPF_6$/EMC, the peaks became even harder to interpret because of overlap with other peaks in the same region from the first measurement. The exact structure of this molecule(s) or how it correlates to the proposed Paths in Figure 2c could not be uniquely elucidated, but some conclusions could still be drawn based on the splitting and shifts of the NMR data. To start, the molecule is likely similar in structure to EMC, but the attached R functional group would need to be more electronegative than a carbonate in order to shift the peaks downfield. In $LiPF_6$/EMC, this could potentially mean two Path B intermediates attaching at the radical site. Secondly, the small differences in peak shape and overlap between $LiClO_4$ and $LiPF_6$ can likely be attributed to the presence of fluorinated species, in analogy to DMC and EC observations. Finally, it is plausible that polymeric species were present in both salts as the electrolyzed solution became highly discoloured and opaque immediately after oxidation, giving way to a gel-like precipitate. This precipitate was measured with ^1H solid-state NMR (Figure S42); however, results

were inconclusive beyond that it is likely a polymeric species. In contrast, the oxidized DMC electrolyte was still transparent with only a slight yellow tint after a month of storage (Figure S43). At this point, the signal-to-noise ratio and prominence of the solvent peaks limited the detection of any possible additional peak(s) of the product(s) in solution. Future research that overcomes these experimental barriers is needed to better clarify their identity and structure.

Beyond this major product, oxidizing EMC produces many of the same species observed upon DMC oxidation, with slight differences in shift, likely due to solvation effects, and much lower intensities, likely due to competing reactions (Figure S44). It was interesting to observe the formation of the A+B intermediate identified for DMC, with a similar lifetime (~1 day of storage). The observation of some DMMBC indicates that cleavage of -O-CH_2- bond on the ethyl side is a competing process. While HCOOH was observed regardless of salt, small amounts of DMDOHC formed in $LiClO_4$, compared to the fluorinated molecules FMMC and FDMDOHC in $LiPF_6$ (Figure 8, Figure S45). These products all indicate that some form of either DMC, DMC$^{\bullet}$, or DMC$^{\bullet+}$ must be generated during EMC oxidation. While EMC has been reported to undergo either disproportionation or transesterification into DMC and DEC [41] in the presence of lithium alkoxides, no evidence of DMC or DEC was observed, unless masked by the bulk EMC, and alkoxides were not observed until after a few weeks of storage. We postulate that minor branching of the reaction involves EMC molecules fragmenting to form DMC$^{\bullet}$ (DMC Path B) and $CH_3^{\bullet}$ after deprotonation of the ethyl group [10,21], which proceed to further react. Unlike with EC, EMC appears highly unlikely to undergo a double proton abstraction due to the steric effects introduced by the additional -CH_3 group. This event would demand the formation of PC, which was never observed.

The deprotonation of the b-site H to produce EMC$^{\bullet}$ (Figure 2b) would explain the formation of 1-fluoroethyl methyl carbonate (FEMC) in $LiPF_6$ [10,64], assigned to ^{1}H peaks at 6.45 ppm (dq, J= 56.4, 5.1 Hz), highlighted in Figure 8 and S39, and at -121.8 ppm in the ^{19}F spectra (dq, J=56.7, 20.7 Hz, Figure S44, S46) [54]. FEMC slowly disappeared with storage time, indicating ongoing reaction dynamics for weeks after oxidation was stopped. The final F-containing product of EMC oxidation was at 6.80 ppm (dd, J= 5.7, 1.8 Hz), correlated with ^{1}H and ^{13}C peaks at 4.99 ppm (m, J=7.1 Hz) and 161.4 ppm, respectively (Figure S47). They appeared to be associated with a ^{19}F signal at -138.8 ppm (dt, J=55.2, 15.5 Hz) (Figure S39) based on similar intensities and peak formation after oxidation. Based on these correlations, this product was assigned as a polymeric form of FEMC (poly(FEMC)), which could further contribute to the dark discoloration and precipitates.

When H_2O was intentionally added to oxidized $LiClO_4$/EMC (Figure S48), almost all the aforementioned intermediates and products were fully quenched. The only observable was a broad peak at 6.27 ppm, which shifted upfield and narrowed over time, giving way to a sharp peak at 5.20 ppm after 10 days. This behaviour suggests that it is likely a polymeric product that is not fully dissolved in solution, but its exact identity remained unclear and warrants future investigation [65]. The near complete disappearance of all other products indicates how even trace levels of H_2O

can drastically affect which oxidation intermediates and products are observable, and even neutralize the subsequent chemical cascades catalysed by the reactive protons.

3. Discussion

Our use of model systems using chemically inert electrodes unlocked the identification and tracking of products resulting from anodic decomposition of common alkyl carbonate solvents in Li-ion batteries, free of confounding factors associated with other battery components or simultaneous degradation processes like lattice oxygen release at the cathode. We also demonstrate that small amounts of H_2O, common in deuterated solvents used for NMR referencing [35], are sufficient to completely skew the observations away from the inherent pathways, and we propose a solution that was key for unobstructed insight. Overall, our approach allowed us to identify the key structures of four new intermediates and four new products compared to the existing body of knowledge [7,10,19]. We were able to discriminate intrinsic solvent activity from the modulation induced by interactions with the specific salt in the electrolyte and even separate salt decomposition. Even in these constrained conditions, the results highlight that the process of electrolyte oxidation is, in reality, a network of reactions with preferential and competing branches that can also cross. This fact likely makes modelling the process extremely challenging, as linear outcomes are typically assumed.

The electrochemical oxidation of all solvents studied begins the same way: electron transfer that may or may not be concurrent to proton transfer. The very high ^{1}H NMR shifts (> 14 ppm) of the protons indicate high reactivity. These acidic species are rarely reported in battery literature, likely because they can be consumed by other cell components, resulting in transition metal dissolution from the cathode, degradation of CEI products, and chemical degradation of the electrolyte producing many products commonly observed in the literature, e.g., CO_2 and a series of ether-based molecules and polymers [4,7,12,34]. Furthermore, their persistence for days after electrolysis indicates that HF and difluorophosphoric acid, observed in electrolytes containing $LiPF_6$ [9], are far from the sole acidic contributors to decomposition.

Electrochemical quantification led to three proposed initial intermediates (Figure 2). Although none of these intermediates can be directly measured with NMR because they are radicals and/or carbocations, forensic identification of the main products provided strong evidence of a preference for a combination of an initial 1-electron (Path A) and 1-electron/1-proton step (Path B). No evidence of molecules that could be tracked to Path C was found. The main products of oxidation in DMC ((F)DMDOHC) and EC (VC) provided the clearest evidence of the existence of Path B. The fluorination of solvent molecules to form FMMC, FEC, and FEMC further implied the preferential deprotonation at specific locations. The existence of Path B indirectly indicates that Path A must also be followed to produce the 2:1 ratio measured via RRDE. In both DMC and EC, metastable intermediates conceivably assembled from the initial intermediates of Path A and B further support this conclusion. Molecules solely associated with Path A were slightly more

challenging to confirm, with downstream products like DMMBC and CO_2 suggesting that chemical evolution is rapid along this pathway. Importantly, not only do competing pathways build a complex network of products, but the fact that they can cross is key to realizing that the damage continues even when the electrolyte is no longer under applied potentials.

The solvents begin to diverge mechanistically after the formation of the initial intermediates. DMC and EC are the simplest forms of their respective class of carbonates (linear and cyclic) and are fully symmetric. There are few possible positions on the molecule where permutations could occur, which leads to very predictable reactions. While they follow largely equivalent pathways, DMC creates fewer and more straightforward products, whereas EC can undergo either ring-opening mechanisms to form polymers along Path A or maintain a ring structure with additional substituents or changes along Path B. The greater stabilization of the ring via delocalized electron density endows the associated intermediates with longer lifetimes, and, thus, measurement prevalence. When an asymmetric molecule like EMC is oxidized, the complexity of the reaction networks increases because a variety of branches are unlocked, including fracturing or functionalization on either side of the molecule. This leads to a mixture reminiscent of the DMC outcomes, plus additional species that include ethyl groups. It is rather trivial to extrapolate that further increasing molecular complexity will scale the complexity of the reaction network, which explains the challenges identifying the products of propylene carbonate (PC) oxidation in the literature [16,21,28]. It is likely that resolution of these challenges will demand combined approaches based on experiments and computational modelling of the reaction explicitly as a network [66].

It is worth pondering the effects of the observed products on the overall health of a battery. At first glance, some of the products formed may seem beneficial to cycling. VC, for example, has been widely included in the electrolyte as a sacrificial additive to form a polymeric CEI and prevent surface reconstruction [6,67]. In the case of DMC, there is still some debate over the role of DMDOHC, with conflicting reports of high viscosity and poor conductivities contrasting with a role avoiding detrimental gas formation upon cycling at high temperature [46,47,68]. Regardless of outcomes, formation of these two products from EC and DMC demands the simultaneous generation of highly reactive protons and their degradation cascades, which would likely negate any benefits they may provide [34].

With the clarity on the mechanisms involved in anodic decomposition in hand, we can tackle an important question: what can be done to stop the oxidation of the electrolyte entirely? Ideally, solvents would be available that simply withstand the potentials at which these alkylcarbonates react, which can be as low as 4.3 V vs. Li^+/Li^0 depending on the metric chosen [34], without penalty along the other requirements for device function, like electrode passivation, current collector stability, viscosity and ionic conductivity [29]. An alternative route involves the use of additives that can act as a radical trap of the initial intermediates or that can target most harmful products in the reaction mechanism. At a fundamental level, the first approach would offer the most comprehensive solution by tackling the earliest intermediates in the network, but it is unclear that

traps exist that are themselves stable at these potentials. At the other end, proton scavengers would prevent chemical degradation breakdown of the solvent into CO_2 and ether species. It is possible that these additives can take the form of molecules in the electrolyte or coatings on the electrode. Outside of electrolyte manipulation, these decomposition pathways could also be halted by simply avoiding the onset potential of proton formation. Ultimately, a multi-pronged approach is likely to be necessary to preventing or alleviating the effects of anodic decomposition, considering the complex network of reactions and the possibility that only the balance of branches is altered.

4.

Conclusions

Anodic decomposition of the electrolyte at high voltages in Li-ion batteries is fundamental to the challenge of durability, especially when high energy density is needed, so establishing their chemical underpinnings is essential. Through a combination of experimental and computational NMR on model electrolyte systems in controlled environments, we isolate the inherent pathways of decomposition of three leading solvents in commercial batteries, DMC, EC and EMC. The approach uncovered key, previously unknown intermediates that allowed us to reconstruct the complex network of reactions associated with the electrochemical process. In all cases, the initial step involves a combination of 1-electron and 1-electron/1-proton transfer, an early onset of branching. Subsequent downstream chemistry depends highly on the symmetry and complexity of the molecule. In symmetric molecules, the continued formation of small molecules is enabled by the formation of metastable intermediates that can fragment to continue to drive chemical degradation. Molecular asymmetry scales the complexity of the reaction network, making it much harder to predict and elucidate. Molecular complexity acts as another factor in network branching, as demonstrated by linear DMC leading to significantly less products than cyclic EC. The results lay bare the complexity of solvent oxidation at high voltages. By systematically isolating each component of the electrolyte and mapping the whole network, this knowledge will guide fresh approaches to mitigation of degradation that more precisely target specific intermediate stages and arrest the worst outcomes, especially when moving towards more complex, multi-solvent systems with battery electrode materials. Central to this goal will be strategies that can prevent the formation or reactivity of protons in the first place, since all reactions appear to be downhill after their formation. The potential payoff in the form of transformational energy density and lifetime demand a renewed effort to translate mechanistic knowledge into sophisticated molecular design.

5.

Experimental Methods

5.1

Electrodes and electrolytes. For rotating disc electrode (RDE) and rotating ring disc electrode (RRDE) measurements, Pt (111) single crystal disk (6 mm diameter) electrodes were used. Prior to assembling the Pt (111) disk into the RDE or RRDE holder (Pine Research Instrumentation), its

surface was conditioned by inductive heating for 7 min at 1050 °C in an argon-hydrogen flow (3 % hydrogen) and cooled slowly to room temperature under the inert atmosphere. Before assembling into RDE or RRDE and during the transfer, the surface of the Pt (111) was protected from oxidation and surface contamination with a droplet of deionized water (Milli-Q system). The difference between the RDE and RRDE holder is that the latter has a Pt ring with inner and outer diameter of approximately 7.5 and 8.5 mm, respectively. The Pt ring surface was prepared by mechanical polishing using SiC paper (1200 grit, Buehler), then rinsed and dried.

The electrolytes were prepared in the Ar-filled glove box by mixing $LiClO_4$ (battery grade, 99.99 % trace metal, Sigma Aldrich), which was dried under dynamic vacuum in the glass oven at 150 °C for 150 h, or $LiPF_6$ (BASF), which was also dried under dynamic vacuum at 120 °C, with ethylene carbonate, dimethyl carbonate or ethyl methyl carbonate (Gotion). The electrolytes had a water content of less than 10 ppm H_2O. All electrolytes were stored in FEP bottles and prepared fresh for all experiments.

5.2

Electrochemical cells for RDE and RRDE analyses. A flooded cell configuration was used for RDE and RRDE measurements. The electrochemical cell was assembled in a three-electrode glass configuration, where a Pt-wire and a Li-metal were used as counter electrode and reference electrode, respectively, inside an Ar-filled glove box (VAC, < 0.2 ppm O_2, < 0.5 ppm H_2O). The electrolyte volume was between 7 mL and 9 mL for RDE and between 35 mL and 45 mL for RRDE (purged with Ar gas).

5.3

Electrochemical protocols. The electrochemical experiments were performed inside an Ar-filled glovebox (VAC, < 0.2 ppm O_2, < 0.5 ppm H_2O) equipped with feedthroughs for gas lines and for electrical connections to a potentiostat located externally (Autolab PGSTAT302N, Metrohm). Measurements were conducted in a custom glass cell, which was dried overnight at 180 °C under vacuum in the antechamber and then directly put inside the glovebox. The cell had a Luggin capillary in which to place the reference electrode (lithium metal) near the working electrode, as well as a frit that separated the counter electrode (platinum wire) from the main compartment. The cell resistance was measured by electrochemical impedance spectroscopy and the potential was manually post-corrected for the ohmic losses. 90 % IR drop correction was used in all electrochemical measurements. The samples for NMR analysis were generated by passing 45 coulombs of charge through the electrolyte galvanostatically at 10mA output current using a Pt (111) electrode at 900 rpm rotation rate.

5.4

NMR analysis. Electrochemically oxidized electrolytes consisting of one salt ($LiClO_4$ or $LiPF_6$) and one solvent (DMC, EC, or EMC) were measured using ^{1}H, ^{13}C, ^{19}F, and ^{35}Cl NMR spectroscopy on a 300MHz Bruker Avance III HD spectrometer with an ATMA BBO probe. 2D

NMR was performed including ^{1}H-^{1}H Homonuclear Correlation Spectroscopy (COSY), ^{1}H-^{13}C Heteronuclear Single Quantum Coherence (HSQC), and Heteronuclear Multiple Bond Correlation (HMBC) using the same spectrometer. All NMR samples were prepared in an argon-filled glovebox with flame sealed glass capillary inserts containing deuterated water (D_2O) as an external reference at 4.67 ppm. Each NMR tube was double sealed with Teflon tape to allow for extended measurements over time at room temperature in the atmosphere. The time between the end of the electrolyte oxidation and the first NMR spectroscopy measurement was roughly 20 minutes. NMR measurements were taken constantly for three straight days and then periodically for a minimum of three weeks. All NMR measurements were performed at room temperature. Solid-state MAS NMR measurements were performed on a 300MHz Bruker Avance III spectrometer using a 3.2 mm zirconium rotor at a spinning speed of 20kHz.

5.5

EPR analysis. Continuous wave (cw) X-band (9.5 GHz) electron paramagnetic resonance (EPR) measurements were conducted using a Bruker ELEXSYS II E500 spectrometer equipped with a rectangular TE_{102} resonator (Bruker ER 4102ST). All EPR measurements were performed at cryogenic temperatures, which was provided by liquid helium gas-flow cryostat (ICE Oxford, UK) and an ITC temperature controller (Oxford Instruments, UK).

5.6

DFT calculations. DFT calculations were conducted using an ab initio quantum chemistry program, ORCA 5.0.4 [69]. The molecular configuration was first optimized based on Universal Force Field (UFF) implemented in a molecule editor and visualizer software, Avogadro, before further optimization at ωB97M-V/ cc-pVQZ/JK level [70]. The chemical shielding tensors and J-coupling tensors were calculated with the B3LYP density functional in conjunction with the pcSseg-n basis set and solvent effects accounted for using the Conductor-like Polarizable Continuum Model (CPCM) based on the dielectric constant and refraction index of EC solution with approximately 1 M of Li salt [71-72]. The shielding values were then converted to predicted chemical shifts with a calibration factor determined by the difference between experimental and calculated chemical shifts of the primary solvent molecule (DMC, EC, etc.) then verified by comparing known products like VC, FEC, and FMMC. Due to the inherent gap in complexity between the modeled systems of electrolyte used in DFT calculations compared to those measured experimentally that contain a host of other species that can affect the solvation structure of the molecule of interest, perfect alignment of simulation and measured is unlikely. Therefore, based on comparisons of species identified via other methods to their predicted shifts, a ±0.3 ppm error range of ^{1}H simulations and ±5.0 ppm error range of ^{13}C simulations has been implemented. Predicted structures were visualized using VESTA [73].

Additional figures, text, and data are provided in the Supplemental Information.

References

[1] J. Xiang, Y. Wei, Y. Zhong, Y. Yang, H. Cheng, L. Yuan, H. Xu and Y. Huang, Building Practical High-Voltage Cathode Materials for Lithium-Ion Batteries, Adv. Mater. 34 (2022) 2200912. https://doi.org/10.1002/adma.202200912.

[2] L. Madec and L. D. Ellis, Exploring interactions between electrodes in $Li[Ni_xMn_yCo_{1-x-y}]O_2$/graphite cells through electrode/electrolyte interfaces analysis, J. Electrochem. Soc. 164 (2017) A3718–A3726. https://doi.org/10.1149/2.1011714jes.

[3] S. C. Jung, D. S. Jung, J. W. Choi and Y.-K. Han, Atom-level understanding of the sodiation process in silicon anode material, J. Phys. Chem. Lett. 5 (2014) 1283–1288. https://doi.org/10.1021/jz5002743.

[4] B. Strehle, K. Kleiner, R. Jung, F. Chesneau, M. Mendez, H. A. Gasteiger and M. Piana, The role of oxygen release from Li- and Mn-rich layered oxides during the first cycles investigated by on-line electrochemical mass spectrometry, J. Electrochem. Soc. 164 (2017) A400–A406. https://doi.org/10.1149/2.1001702jes.

[5] L. Rynearson, C. Antolini, C. Jayawardana, M. Yeddala, D. Hayes and B. L. Lucht, Speciation of transition metal dissolution in electrolyte from common cathode materials, Angew. Chem. Int. Ed. 63 (2024) e202317109. https://doi.org/10.1002/anie.202317109.

[6] H. Dai, L. Gomes, D. Maxwell, S. Zamani, K. Yang, D. Atienza, N. Dale and S. Mukerjee, Exploring the role of an electrolyte additive in suppressing surface reconstruction of a Ni-rich NMC cathode at ultrahigh voltage via enhanced in situ and operando characterization methods, ACS Appl. Mater. Interfaces 16 (2024) 8639–8654. https://doi.org/10.1021/acsami.3c15670.

[7] B. L. D. Rinkel, D. S. Hall, I. Temprano and C. P. Grey, Electrolyte oxidation pathways in lithium-ion batteries, J. Am. Chem. Soc. 142 (2020) 15058–15074. https://doi.org/10.1021/jacs.0c06363.

[8] M. Metzger, P. Walke, S. Solchenbach, G. Salitra, D. Aurbach and H. A. Gasteiger, Evaluating the high-voltage stability of conductive carbon and ethylene carbonate with various lithium salts, J. Electrochem. Soc. 167 (2020) 160522. https://doi.org/10.1149/1945-7111/abcabd.

[9] C. Jayawardana, N. Rodrigo, B. Parimalam and B. L. Lucht, Role of electrolyte oxidation and difluorophosphoric acid generation in crossover and capacity fade in lithium-ion batteries, ACS Energy Lett. 6 (2021) 3788–3792. https://doi.org/10.1021/acsenergylett.1c01657.

[10] Y. Zhang, Y. Katayama, R. Tatara, L. Giordano, Y. Yu, D. Fraggedakis, J. G. Sun, F. Maglia, R. Jung, M. Z. Bazant and Y. Shao-Horn, Revealing electrolyte oxidation via carbonate dehydrogenation on Ni-based oxides in Li-ion batteries by in situ FTIR spectroscopy, Energy Environ. Sci. 13 (2020) 183–199. https://doi.org/10.1039/C9EE02543J.

[11] B. L. D. Rinkel, J. P. Vivek, N. Garcia-Araez and C. P. Grey, Two electrolyte decomposition pathways at nickel-rich cathode surfaces in lithium-ion batteries, Energy Environ. Sci. 15 (2022) 3416–3438. https://doi.org/10.1039/D1EE04053G.

[12] R. Jung, M. Metzger, F. Maglia, C. Stinner and H. A. Gasteiger, Chemical versus electrochemical electrolyte oxidation on NMC111, NMC622, NMC811, LNMO, and conductive carbon, J. Phys. Chem. Lett. 8 (2017) 4820–4825. https://doi.org/10.1021/acs.jpclett.7b01927.

[13] L. Yang, B. Ravdel and B. L. Lucht, Electrolyte reactions with the surface of high voltage $LiNi_{0.5}Mn_{1.5}O_4$ cathodes for lithium-ion batteries, Electrochem. Solid-State Lett. 13 (2010) A95–A98. https://doi.org/10.1149/1.3428515.

[14] O. Borodin, W. Behl and T. R. Jow, Oxidative stability and initial decomposition reactions of carbonate, sulfone, and alkyl phosphate-based electrolytes, J. Phys. Chem. C 117 (2013) 8661–8682. https://doi.org/10.1021/jp400527c.

[15] L. Xing and O. Borodin, Oxidation-induced decomposition of ethylene carbonate from DFT calculations: importance of explicitly treating surrounding solvent, Phys. Chem. Chem. Phys. 14 (2012) 12838–12843. https://doi.org/10.1039/C2CP41103B.

[16] L. Xing, O. Borodin, G. D. Smith and W. Li, Density functional theory study of the role of anions on the oxidative decomposition reaction of propylene carbonate, J. Phys. Chem. A 115 (2011) 13896–13905. https://doi.org/10.1021/jp206153n.

[17] L. Huai, Z. Chen and J. Li, Degradation mechanism of dimethyl carbonate dissociation on the $LiCoO_2$ cathode surface: a first-principles study, ACS Appl. Mater. Interfaces 9 (2017) 36377–36384. https://doi.org/10.1021/acsami.7b09352.

[18] E. W. C. Spotte-Smith, S. Vijay, T. B. Petrocelli, B. L. D. Rinkel, B. D. McCloskey and K. A. Persson, A critical analysis of chemical and electrochemical oxidation mechanisms in Li-ion batteries, J. Phys. Chem. Lett. 15 (2024) 391–400. https://doi.org/10.1021/acs.jpclett.3c03279.

[19] A. T. S. Freiberg, M. K. Roos, J. Wandt, R. de Vivie-Riedle and H. A. Gasteiger, Singlet oxygen reactivity with carbonate solvents used for Li-ion battery electrolytes, J. Phys. Chem. A 122 (2018) 8828–8839. https://doi.org/10.1021/acs.jpca.8b08079.

[20] B. L. D. Rinkel, R. S. Mohanakrishnan, J. Lee, K. A. Persson and B. D. McCloskey, Reactivity of cyclic and linear alkyl carbonates with reactive oxygen species, J. Am. Chem. Soc. 147 (2025) 12089–12098. https://doi.org/10.1021/jacs.5c12089.

[21] I. A. Shkrob, Y. Zhu, T. W. Marin and D. Abraham, Reduction of carbonate electrolytes and the formation of solid-electrolyte interface (SEI) in lithium-ion batteries. 1. Spectroscopic observations of radical intermediates generated in one-electron reduction of carbonates, J. Phys. Chem. C 117 (2013) 19255–19269. https://doi.org/10.1021/jp406274e.

[22] I. A. Shkrob, Y. Zhu, T. W. Marin and D. Abraham, Reduction of carbonate electrolytes and the formation of solid-electrolyte interface (SEI) in lithium-ion batteries. 2. Radiolytically induced polymerization of ethylene carbonate, J. Phys. Chem. C 117 (2013) 19270–19279. https://doi.org/10.1021/jp406273p.

[23] M. Moshkovich, M. Cohocaru, H. E. Gottlieb and D. Aurbach, The study of the anodic stability of alkyl carbonate solutions by in situ FTIR spectroscopy, EQCM, NMR, and MS, J. Electroanal. Chem. 497 (2001) 84–96. https://doi.org/10.1016/S0022-0728(00)00457-5.

[24] R. Wagner, M. Korth, B. Streipert, J. Kasnatscheew, D. R. Gallus, S. Brox, M. Amereller, I. Cekic-Laskovic, M. Winter and K. U. Schwenke, Impact of selected $LiPF_6$ hydrolysis products on the high-voltage stability of lithium-ion battery cells, ACS Appl. Mater. Interfaces 8 (2016) 30871–30878. https://doi.org/10.1021/acsami.6b09164.

[25] S. E. Sloop, J. K. Pugh, S. Wang, J. B. Kerr and K. Kinoshita, Chemical reactivity of PF_5 and $LiPF_6$ in ethylene carbonate/dimethyl carbonate solutions, Electrochem. Solid-State Lett. 4 (2001) A42–A44. https://doi.org/10.1149/1.1353158.

[26] L. Hartmann, L. Reuter, L. Wallisch, A. Beiersdorfer, A. Adam, D. Goldbach, T. Teufl, P. Lamp, H. A. Gasteiger and J. Wandt, Depletion of electrolyte salt upon calendar aging of lithium-ion batteries and its effect on cell performance, J. Electrochem. Soc. 171 (2024) 060506. https://doi.org/10.1149/1945-7111/ad4821.

[27] J.-M. Tarascon and D. Guyomard, New electrolyte compositions stable over the 0 to 5 V voltage range and compatible with the $Li_{1+x}Mn_2O_4$/carbon Li-ion cells, Solid State Ion. 69 (1994) 293–305. https://doi.org/10.1016/0167-2738(94)90418-9.

[28] G. Eggert and J. Heitbaum, Electrochemical reactions of propylene carbonate and electrolytes solved therein—a DEMS study, Electrochim. Acta 31 (1986) 1443–1448. https://doi.org/10.1016/0013-4686(86)87057-8.

[29] K. Xu, Nonaqueous liquid electrolytes for lithium-based rechargeable batteries, Chem. Rev. 104 (2004) 4303–4418. https://doi.org/10.1021/cr030203g.

[30] I. Azcarate, W. Yin, C. Méthivier, F. Ribot, C. Laberty-Robert and A. Grimaud, Assessing the oxidation behavior of EC:DMC-based electrolyte on non-catalytically active surfaces, J. Electrochem. Soc. 167 (2020) 080530. https://doi.org/10.1149/1945-7111/ab8f57.

[31] H. Yoshida, T. Fukunaga, T. Hazama, M. Terasaki, M. Mizutani and M. Yamachi, Degradation mechanism of alkyl carbonate solvents used in lithium-ion cells during initial charging, J. Power Sources 68 (1997) 311–315. https://doi.org/10.1016/S0378-7753(97)02635-9.

[32] J. Henschel, C. Peschel, S. Klein, F. Horsthemke, M. Winter and S. Nowak, Clarification of decomposition pathways in a state-of-the-art lithium-ion battery electrolyte

through ^{13}C labeling of electrolyte components, Angew. Chem. Int. Ed. 59 (2020) 6128–6137. https://doi.org/10.1002/anie.202000727.

[33] R. C. McNulty, K. D. Jones, B. M. G. Denison, E. Hampson, I. Temprano, D. A. Walsh, H. W. Lam, G. N. Newton, W. M. Dose, C. P. Grey and L. R. Johnson, Singlet oxygen is not the source of ethylene carbonate degradation in nickel-rich Li-ion cells, Energy Environ. Sci. 18 (2025) 7603–7609. https://doi.org/10.1039/D5EE00956A.

[34] S. Ilic, M. Martins, H. Liu, P. F. B. D. Martins, D. Haering, J. Yang, T. Hatsukade, B. Genorio, S. E. Weitzner, L.-F. Wan, Z. Zhang, J. G. Connell, B. Key, J. Cabana and D. Strmcnik, An unwanted guest in the electrochemical oxidation of high-voltage Li-ion battery electrolytes: the life of highly reactive protons, Energy Environ. Sci. 18 (2025) 8303–8312. https://doi.org/10.1039/D5EE02403J.

[35] G. R. Fulmer, A. J. M. Miller, N. H. Sherden, H. E. Gottlieb, A. Nudelman, B. M. Stoltz, J. E. Bercaw and K. I. Goldberg, NMR chemical shifts of trace impurities: common laboratory solvents, organics, and gases in deuterated solvents relevant to the organometallic chemist, Organometallics 29 (2010) 2176–2179. https://doi.org/10.1021/om100106e.

[36] P. R. D. Murray, J. H. Cox, N. D. Chiappini, C. B. Roos, E. A. McLoughlin, B. G. Hejna, S. T. Nguyen, H. H. Ripberger, J. M. Ganley, E. Tsui, N. Y. Shin, B. Koronkiewicz, G. Qiu and R. R. Knowles, Photochemical and electrochemical applications of proton-coupled electron transfer in organic synthesis, Chem. Rev. 122 (2022) 2017–2291. https://doi.org/10.1021/acs.chemrev.1c00374.

[37] T. Hatsukade, M. Zorko, D. Haering, N. M. Marković, V. R. Stamenković and D. Strmcnik, Detection of protons using the rotating ring-disk electrode method during electrochemical oxidation of battery electrolytes, Electrochem. Commun. 120 (2020) 106785. https://doi.org/10.1016/j.elecom.2020.106785.

[38] S. K. Davidowski, F. Thompson, W. Huang, M. Hasani, S. A. Amin, C. A. Angell and J. L. Yarger, NMR characterization of ionicity and transport properties for a series of diethylmethylamine-based protic ionic liquids, J. Phys. Chem. B 120 (2016) 4279–4285. https://doi.org/10.1021/acs.jpcb.6b01203.

[39] W. M. Dose, W. Li, I. Temprano, C. A. O'Keefe, B. L. Mehdi, M. F. L. De Volder and C. P. Grey, Onset potential for electrolyte oxidation and Ni-rich cathode degradation in lithium-ion batteries, ACS Energy Lett. 7 (2022) 3524–3530. https://doi.org/10.1021/acsenergylett.2c01722.

[40] X. Liu, Structural effects on acidity and basicity, in Organic Chemistry I, Kwantlen Polytechnic University, Surrey, BC, 2021.

[41] T. Sasaki, T. Abe, Y. Iriyama, M. Inaba and Z. Ogumi, Formation mechanism of alkyl dicarbonates in Li-ion cells, J. Power Sources 150 (2005) 208–215. https://doi.org/10.1016/j.jpowsour.2005.02.021.

[42] T. Taskovic, A. Adamson, A. Clarke, E. D. Alter, A. Eldesoky, K. L. Gering, K. Tuul and J. R. Dahn, Alkyl dicarbonates, common electrolyte degradation products, can enable long-lived Li-ion cells at high temperatures, J. Electrochem. Soc. 170 (2023) 090527. https://doi.org/10.1149/1945-7111/acf886.

[43] G. Gachot, S. Grugeon, M. Armand, S. Pilard, P. Guenot, J.-M. Tarascon and S. Laruelle, Deciphering the multi-step degradation mechanisms of carbonate-based electrolyte in Li batteries, J. Power Sources 178 (2008) 409–421. https://doi.org/10.1016/j.jpowsour.2007.11.110.

[44] A. J. Pell, G. Pintacuda and C. P. Grey, Paramagnetic NMR in solution and the solid state, Prog. Nucl. Magn. Reson. Spectrosc. 111 (2019 1–271. https://doi.org/10.1016/j.pnmrs.2018.05.001.

[45] I. Berregi, G. del Campo, R. Caracena and J. I. Miranda, Quantitative determination of formic acid in apple juices by ^{1}H NMR spectrometry, Talanta 72 (2007) 1049–1053. https://doi.org/10.1016/j.talanta.2006.12.031.

[46] F. J. Weigert, Fluorine magnetic resonance spectra of monofluoro- and difluoro-substituted hydrocarbons, J. Org. Chem. 45 (1980) 3476–3483. https://doi.org/10.1021/jo01305a022.

[47] S. Wilken, M. Treskow, J. Scheers, P. Johansson and P. Jacobsson, Initial stages of thermal decomposition of $LiPF_6$-based lithium-ion battery electrolytes by detailed Raman and NMR spectroscopy, RSC Adv. 3 (2013) 16359–16369. https://doi.org/10.1039/C3RA42611D.

[48] S. Wiemers-Meyer, M. Winter and S. Nowak, Mechanistic insights into lithium-ion battery electrolyte degradation—a quantitative NMR study, Phys. Chem. Chem. Phys. 18 (2016) 26595–26601. https://doi.org/10.1039/C6CP05276B.

[49] M. Takehara, S. Watanabe, N. Nanbu, M. Ue and Y. Sasaki, Synthesis of fluorinated dimethyl carbonates by direct fluorination, Synth. Commun. 34 (2004) 1367–1375. https://doi.org/10.1081/SCC-120030685.

[50] C. L. Campion, W. Li and B. L. Lucht, Thermal decomposition of $LiPF_6$-based electrolytes for lithium-ion batteries, J. Electrochem. Soc. 152 (2005) A2327–A2334. https://doi.org/10.1149/1.2083267.

[51] L. Terborg, S. Weber, F. Blaske, S. Passerini, M. Winter, U. Karst and S. Nowak, Investigation of thermal aging and hydrolysis mechanisms in commercial lithium-ion battery electrolyte, J. Power Sources 242 (2013) 832–837. https://doi.org/10.1016/j.jpowsour.2013.05.125.

[52] Y.-F. Qiu, H. Murayama, C. Fujitomo, S. Kawai, A. Haruta, T. Hiasa, H. Mita, K. Motohashi and M. Tokunaga, Oxidative decomposition mechanism of ethylene carbonate on

positive electrodes in lithium-ion batteries, Bull. Chem. Soc. Jpn. 96 (2023) 444–451. https://doi.org/10.1246/bcsj.20230027.

[53] H. Gunther, NMR Spectroscopy: Basic Principles, Concepts and Applications in Chemistry, 3rd ed., Wiley-VCH, Weinheim, 2013.

[54] R. L. B. Chen, F. N. Sayed, H. Banerjee, I. Temprano, J. Wan, A. J. Morris and C. P. Grey, Identification of the dual roles of Al_2O_3 coatings on NMC811 cathodes via theory and experiment, Energy Environ. Sci. 18 (2025) 1879–1900. https://doi.org/10.1039/D4EE03444A.

[55] S. Takabatake, N. Sagawa and T. Shikata, Quantitative antiparallel dimer formation analysis of ethylene carbonate in solution, Bull. Chem. Soc. Jpn. 89 (2016) 237–242. https://doi.org/10.1246/bcsj.20150346.

[56] N. Sagawa, S. Takabatake and T. Shikata, A dielectric spectroscopic study of ethylene carbonate in solution, Bull. Chem. Soc. Jpn. 89 (2016) 1018–1025. https://doi.org/10.1246/bcsj.20160126.

[57] H. Ota, Y. Sakata, Y. Otake, K. Shima, M. Ue and J.-I. Yamaki, Structural and functional analysis of surface film on Li anode in vinylene carbonate-containing electrolyte, J. Electrochem. Soc. 151 (2004) A1778–A1788. https://doi.org/10.1149/1.1798411.

[58] S. Schmidt, F. J. Gatti, M. Luitz, B. S. Ritter, B. Bruchmann and R. Mulhaupt, Erythritol dicarbonate as intermediate for solvent- and isocyanate-free tailoring of bio-based polyhydroxyurethane thermoplastics and thermoplastic elastomers, Macromolecules 50 (2017) 1604–1615. https://doi.org/10.1021/acs.macromol.6b02787.

[59] N. Gogoi, R. Lundstrom, G. Hernandez and E. J. Berg, Base-driven ring-opening reactions of vinylene carbonate, J. Electrochem. Soc. 171 (2024) 050506. https://doi.org/10.1149/1945-7111/ad430e.

[60] L. Xing, W. Li, C. Wang, F. Gu, M. Xu, C. Tan and J. Yi, Theoretical investigations on oxidative stability of solvents and oxidative decomposition mechanism of ethylene carbonate for lithium-ion battery use, J. Phys. Chem. B 113 (2009) 16596–16602. https://doi.org/10.1021/jp9074064.

[61] R. Kukeva, M. Kalapsazova, H. Rasheev, G. Vassilev, A. Tadjer and R. Stoyanova, In situ electron paramagnetic resonance monitoring of predegradation radical generation in a lithium electrolyte, J. Phys. Chem. Lett. 14 (2023) 9633–9639. https://doi.org/10.1021/acs.jpclett.3c02374.

[62] V. N. Torocheshnikov and N. M. Sergeyev, ^{35}Cl and ^{37}Cl nuclear magnetic resonance of chloroorganic compounds, Chem. Phys. Lett. 288 (1998) 809–815. https://doi.org/10.1016/S0009-2614(98)00362-5.

[63] T. Li and P. B. Balbuena, Theoretical studies of lithium perchlorate in ethylene carbonate, propylene carbonate, and their mixtures, J. Electrochem. Soc. 145 (1999) 3613–3622. https://doi.org/10.1149/1.1392523.

[64] M. Hasegawa, H. Ishii, Y. Cao and T. Fuchigami, Regioselective anodic monofluorination of ethers, lactones, carbonates, and esters using ionic liquid fluoride salts, J. Electrochem. Soc. 153 (2006) D162–D166. https://doi.org/10.1149/1.2222891.

[65] F. A. Bovey, The high-resolution nuclear magnetic resonance spectroscopy of polymers, Prog. Polym. Sci. 3 (1963) 139–172.

[66] S. M. Blau, H. D. Patel, E. W. C. Spotte-Smith, X. Xie, S. Dwaraknath and K. A. Persson, A chemically consistent graph architecture for massive reaction networks applied to solid-electrolyte interphase formation, Chem. Sci. 12 (2021) 4931–4939. https://doi.org/10.1039/D0SC05647B.

[67] L. El Ouatani, R. Dedryvere, C. Siret, P. Biensan, S. Reynaud, P. Iratcabal and D. Gonbeau, The effect of vinylene carbonate additive on surface film formation on both electrodes in Li-ion batteries, J. Electrochem. Soc. 156 (2009) A103–A113. https://doi.org/10.1149/1.3029674.

[68] L. M. Thompson, W. Stone, A. Eldesoky, N. K. Smith, C. R. M. McFarlane, J. S. Kim, M. B. Johnson, R. Petibon and J. R. Dahn, Quantifying changes to the electrolyte and negative electrode in aged NMC532/graphite lithium-ion cells, J. Electrochem. Soc. 165 (2018) A2732–A2740. https://doi.org/10.1149/2.0721811jes.

[69] F. Neese, F. Wennmohs, U. Becker and C. Riplinger, The ORCA quantum chemistry program package, J. Chem. Phys. 152 (2020) 224108. https://doi.org/10.1063/5.0004608.

[70] N. B. Balabanov and K. A. Peterson, Systematically convergent basis sets for transition metals. I. All-electron correlation consistent basis sets for the 3d elements Sc–Zn, J. Chem. Phys. 123 (2005) 064107. https://doi.org/10.1063/1.1998907.

[71] F. Jensen, Segmented contracted basis sets optimized for nuclear magnetic shielding, J. Chem. Theory Comput. 11 (2015) 132–138. https://doi.org/10.1021/ct5009526.

[72] R. P. Seward and E. C. Vieira, The dielectric constants of ethylene carbonate and of solutions of ethylene carbonate in water, methanol, benzene and propylene carbonate, J. Phys. Chem. 62 (1958) 127–128. https://doi.org/10.1021/j150559a041.

[73] K. Momma and F. Izumi, VESTA 3 for three-dimensional visualization of crystal, volumetric and morphology data, J. Appl. Crystallogr. 44 (2011) 1272–1276. https://doi.org/10.1107/S0021889811038970.

Figure 1. a) Current measured on the disk and b) ring of the RRDE setup during oxidation of $LiClO_4$/DMC (purple), EC (blue), and EMC (pink), c) ratio of protons to electrons participating in the oxidation reaction across the three solvents at different voltage points obtained by dividing the currents in a) and b), d) Zoom of the ^1H NMR spectra tracking the evolution of electrogenerated protons in $LiPF_6$/DMC (top), /EC (middle), and /EMC (bottom) over storage time

Figure 2. Proposed electrochemical oxidation pathways of electrolytes with a) DMC, b) EC, and c) EMC

Figure 3: Oxidation and chemical degradation pathways of DMC.

Figure 4: Region between a) 4.50 and 6.50 ppm and b) 3.35 and 4.20 ppm of the ^1H NMR spectra, and c) ^{13}C NMR spectra of $LiClO_4$/DMC electrolyte at different time stamps. "Pristine" refers to the electrolyte prior to electrolysis, with "Oxidized Day 1" occurring roughly 20 minutes after electrolysis was stopped. The color coding follows the same assignment as Figure 3: the reaction intermediates are highlighted in yellow, the major oxidation product in green and the products of chemical cascades in purple. The zoom to the right of panel a) shows a close look at the increase in intensity of the major product.

Figure 5: a) ^1H shifts of oxidized $LiPF_6$/DMC electrolyte at different time points after initial electrochemical oxidation was stopped from 4.50-6.50 ppm. The reaction intermediate peak is highlighted in yellow at 6.45 ppm. The major oxidation product at 4.64 ppm is highlighted in green and its intensity increase upon aging is expanded upon on the right. b) ^1H and ^{13}C correlation 2D NMR (HSQC (left) and HMBC (right)) of FDMDOHC and other oxidation products, inset of labeled FDMDOHC structure. c) ^1H shifts of oxidized $LiPF_6$/DMC electrolyte at different time points after initial electrochemical oxidation has stopped from 3.55-4.82 ppm, d) ^{19}F shifts of FMMC and BF_4^- in oxidized $LiPF_6$/DMC

Figure 6: Oxidation and chemical degradation pathways of EC

Figure 7: ^1H shifts of oxidized EC electrolyte with $LiClO_4$ (top) or $LiPF_6$ (bottom) at different time points after initial electrochemical oxidation has stopped. The reaction intermediates are highlighted in yellow. The major oxidation product, VC, is highlighted in green and expanded upon on the left.

Figure 8: ^1H shifts of oxidized $LiPF_6$/EMC electrolyte at different time points after initial electrochemical oxidation has stopped. Intermediates are highlighted in yellow and the major oxidation product at 4.97 ppm and 1.67 ppm is highlighted in green. Its intensity increase upon aging is expanded upon below.